Dedicated to innovation in aerospace

AIRTuB Field lab ZEPHYROS

PUBLIC

NLR-CR-2021-177 | February 2023

Remote Ultrasonic Inspection of Offshore Wind Turbine Blades

Automated Inspection and Repair of Turbine Blades (AIRTuB) - WP1

CUSTOMER: World Class Maintenance (WCM)

Royal NLR - Netherlands Aerospace Centre

Dedicated to innovation in aerospace

Remote Ultrasonic Inspection of Offshore Wind Turbine Blades

Automated Inspection and Repair of Turbine Blades (AIRTuB) - WP1

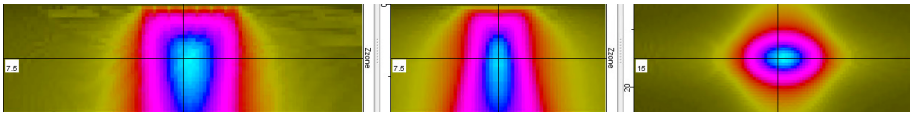

Simulated sound waves in a GFRP rotor blade

REPORT NUMBER
NLR-CR-2021-177

AUTHOR(S)
D.J. Platenkamp
V.S.V. Dhanisetty
A. Chabok
A.F. Bosch

REPORT CLASSIFICATION
UNCLASSIFIED

DATE
February 2023

KNOWLEDGE AREA(S)
Aerospace Structures Testing

DESCRIPTOR(S)
Offshore Wind Turbine Blades
Non-Destructive Testing
Remote

Problem area

Automated Inspection and Repair of Turbine Blades (AIRTuB) project pursues to reduce the downtime on the maintenance of the offshore wind blades, by developing an unmanned automated system capable of performing necessary inspections. Such system can perform inspection on the blades, instead of human inspectors. One of the objectives of AIRTuB project is to develop sensor systems, capable of inspecting remotely internal and external damages on the offshore wind turbine blades, by a small unmanned vehicle. Two unmanned vehicles are foreseen, one drone for the inspection of external damage and another one for transport of a crawler. The crawler is equipped with an ultrasonic sensor to inspect the internal integrity of the turbine blades. Consortium partner TU-Delft developed an inspection device based on an off-the-shelf phased array roller probe. The inspection device is integrated in the crawler developed by consortium partner HZ University of Applied Sciences. For integration of this roller probe into the crawler, TU-Delft designed a mechanical structure to hold the roller probe, water spray, analyzer and battery together. The off-the-shelf phased array roller probe is a good first starting point and in principal suitable for the rotor blade inspection task. But this concept has a weight of >5 kg (excluding cable and connector). Payload is key, because the crawler and sensor package are transported by drone. In parallel, NLR developed its own PAUT sliding probe (Phased Array Ultrasonic Testing) with a payload < 1 kg.

This report describes;

- The design, development and testing of a light weight probe holder containing an off-the-shelf PAUT sensor. The combination of probe holder and PAUT sensor is further called PAUT sliding probe.

- Integration of this PAUT sliding probe into the crawler.
- Ultrasonic modelling.
- Ultrasonic experimental performance on real turbine blade specimens.

Description of work

Based on the literature “Survey on Remote Inspection of Offshore Wind Turbine Blades” (ref. 1), the ultrasonic-based NDI method is found to be the most practical approach in terms of miniaturization possibilities and damage detection possibilities in thick composite material. Phased Array Ultrasonic Testing (PAUT) method may provide practical solution. Conventional ultrasonic C-scan inspection is used as a baseline inspection. Representative reference specimens (sectioned from a real wind turbine rotor blade) are immersed in a water tank. Due to constant coupling and the application of focused transducers an optimal sensitivity and resolution is achieved. NLR developed a new PAUT sliding probe, with a weight <1 kg, that can be integrated into the crawler design. Payload is key in this approach, because the crawler and sensor package are transported by drone. CIVA modelling and experimental phased array tests are performed on the reference specimens and compared to the baseline conventional ultrasonic C-scan inspections.

Results and conclusions

The investigation showed that NLR’s light weight PAUT sliding probe gives impact damage detection, which is comparable to conventional ultrasonic C-scan baseline inspections. Furthermore, the PAUT sliding probe showed good coupling and sliding performance. Further development is recommended to control the amount of fluid between phased array probe and the foil. Miniaturisation and wireless remote control of the phased ultrasonic device needs further attention.

Applicability

Especially if the damage has occurred in a primary structure in an offshore wind turbine blades, it is important to evaluate and repair the damage if necessary. Moreover, the efficiency of a wind turbine can even be optimized if the design philosophy transitions from safe-life (currently used design philosophy) towards damage-tolerance design principle (aerospace design philosophy). In order to realize this transition, non-destructive inspection is a key to this.
Based on the literature study (ref.1), ultrasonic-based NDI will become a major method to inspect offshore wind turbine blades. It is highly recommended to consider the introduction of advanced faster and cost-effective ultrasonic phased array methods.

Royal NLR
Anthony Fokkerweg 2
1059 CM Amsterdam, The Netherlands
p) +31 88 511 3113
e) info@nlr.nl i) www.nlr.nl

Dedicated to innovation in aerospace

PUBLIC

NLR-CR-2021-177 | February 2023

Remote Ultrasonic Inspection of Offshore Wind Turbine Blades

Automated Inspection and Repair of Turbine Blades (AIRTuB) - WP1

CUSTOMER: World Class Maintenance (WCM)

AUTHOR(S):

D.J. Platenkamp	NLR
V.S.V. Dhanisetty	NLR
A. Chabok	NLR
A.F. Bosch	NLR

Royal NLR - Netherlands Aerospace Centre

The project is executed with subsidy from Topsector Energy part of Ministry of Economic Affairs.

CUSTOMER	**World Class Maintenance (WCM)**
CONTRACT NUMBER	**---**
OWNER	**NLR**
DIVISION NLR	**Aerospace Vehicles**
DISTRIBUTION	**Unlimited**
CLASSIFICATION OF TITLE	**UNCLASSIFIED**

APPROVED BY:		**Date**
AUTHOR	D.J. Platenkamp	14-02-2023
REVIEWER	J.S. Hwang	14-02-2023
MANAGING DEPARTMENT	P. Arendsen	15-02-2023

Summary

The goal of the project ”Automated Inspection and Repair of Turbine Blades (AIRTuB)” is to reduce the downtime during maintenance of the offshore wind blades, by developing an unmanned automated system capable of performing necessary inspections. Especially if the damage has occurred in a primary structure, it is important to evaluate and repair the damage in time, if necessary. Moreover, the efficiency of a wind turbine can even be optimized, if the design philosophy changes from safe-life (currently used design philosophy) towards damage-tolerance (aerospace design philosophy), (ref. 1). In order to realize this change, non-destructive inspection is key to this.

Based on the literature study “Survey on Remote Inspection of Offshore Wind Turbine Blades” (ref.1), ultrasonic-based NDI methods is found to be the most practical approach in terms of miniaturization possibilities and damage detection possibilities in thick composite material.

This report gives the test results of an investigation into the applicability of Phased Array Ultrasonic Testing (PAUT) for the in-service inspection of offshore wind turbine blades. The NLR developed a light weight weight probe holder containing an off-the-shelf PAUT sensor. The combination of probe holder and PAUT sensor is further called PAUT sliding probe.
CIVA modulation of PAUT definitely supports the experimental investigation. The appearance of the ultrasound beam profiles per aperture size gives an underpinned insight to make the correct choice w.r.t. transducer type and instrument settings.
The investigation showed that the light weight PAUT sliding probe gives impact damage detection compared to conventional ultrasonic C-scan baseline inspections. Typicall defects sizes detected are in the range from 0.5 to 1.5 inch. Further, the FBH responses in CIVA and the PAUT experimental test results are quite comparable.

The reference specimens were cut from relative old (~30 years) rotor blades with relative low material quality and a thickness of approx 15 mm. In consequence, this relatively low material quality has an negative influence on the inspection performance. On the other hand, nowadays large off-shore rotor blades have skin thickness of approx. 60 mm. Compared to the reference specimens used in this investigation (15 mm), it is questionable whether the reference specimen used in this study represents the current state. It is recommended that the experiments are performed on representative thicknesses.

Even though, the PAUT sliding probe showed good coupling and sliding performance further development is recommended to control the amount of fluid between phased array probe and the protecting foil. Miniaturisation and wire-less remote control of the phased ultrasonic device needs further attention.

Contents

Abbreviations

ACRONYM	DESCRIPTION
BR	Backwall Reflection
CFRP	Composite Fibre Reinforced Plastics
CS	Cross-section
CT	Computed Tomography
DAC	Distance Amplitude Curve
FOD	Foreign Object Damage
FR	Front Reflection
GFRP	Glass Fibre Reinforced Plastics
IRP	Inspection Reference Panels
NDI/NDT	Non-Destructive Inspection/Non-Destructive Testing
NLR	Royal NLR - Netherlands Aerospace Centre
PA	Phased Array
PAUT	Phased Array Ultrasonic Testing
PET	Poly Ethylene Terephthalate
TCG	Time Corrected Gain
TOF	Time Of Flight
UT	Ultrasonic Testing

1 Introduction

Automated Inspection and Repair of Turbine Blades (AIRTuB) project pursues to reduce the downtime on the maintenance of the offshore wind blades by developing an unmanned automated system capable of performing necessary inspections. Such system can perform inspection on the blades instead of human inspectors. One of the objectives of AIRTuB project is to develop sensor systems, capable of remotely inspecting internal and external damages on the offshore wind turbine blades, by a small unmanned vehicle. Two unmanned vehicles are foreseen, a drone for the inspection of external damage and another drone to transport a crawler. The crawler is equipped with a ultrasonic sensor to inspect the internal integrity of the turbine blades.
Consortium partner TU-Delft developed an inspection device based on an off-the-shelf phased array roller probe. The inspection device is integrated in the crawler developed by consortium partner HZ University of Applied Sciences. For integration of this roller probe into the crawler, TU-Delft designed a mechanical structure to hold the roller probe, water spray, analyzer and battery together. Furthermore, this structure has a tilt mechanism which can lift the roller probe up when the inspection is not needed (e.g. moving the crawler from landing position to the area of interest). This enables remotely positioning of the probe on and off the wind turbine rotor blade.
The off-the-shelf phased array roller probe is a good first starting point and in principal suitable for the rotor blade inspection task. But this concept has a weight of >5 kg (excluding cable and connector). Payload is key, because the crawler and sensor package are transported by drone. In parallel NLR developed its own light weight probe holder containing an off-the-shelf PAUT sensor, with a payload < 1 kg. The combination of probe holder and PAUT sensor is further called PAUT sliding probe.

This report describes;

- The design, development and testing of a light weight PAUT sliding probe containing an off-the-shelf PAUT sensor.
- Integration of this PAUT sliding probe into the crawler.
- Ultrasonic modelling.
- Ultrasonic experimental performance on real turbine blade specimens.

2 Wind Turbine Rotor Blade

This chapter describes the configuration of a wind turbine rotor blade and the type of materials used. Further, to underpin NDT results representative reference specimens are required. The NDT reference specimens are cut from a full-scale wind turbine blade provided by LM-Windpower. The reference panels are provided with Flat Bottom Holes, which is an establish method of basic characterisation of the ultrasonic methods. To verify the general material quality of the NDT reference specimens, cross-sections and Computed Tomography (CT) scan analysis are performed.

2.1 Configuration wind turbine rotor blade

A modern and typical wind turbine rotor blade consists out of two important parts: the outer skins and inner spars. The individually produced parts are assembled by bonding the two outer skins with inner structures (in this example, there are two spars), see Figure 2-1.

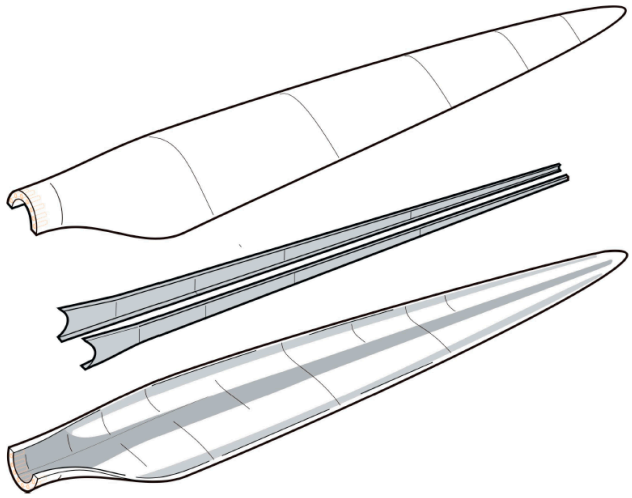

Figure 2-1: Schematics of a wind blade, assembled by bonding the two outer skins with inner structures (in this example, there are two spars) [Ref.1]

Most modern wind blades are made of composite materials featuring a thermoset polymer matrix, such as epoxy or polyester, with reinforcing glass (GFRP) or carbon fibers (CFRP). Thin sectioned areas of the blade may consist of laminates built by multiple and variably oriented unidirectionally reinforced plies. More thicker or structurally critical areas may comprise of laminates consisting of biaxial or triaxial weave reinforced plies. Furthermore, a thick section may also comprise out of shell structure, consisting of laminate layer(s) enforced with a core structure (foam or balsa wood). The inner structure carries the structural load and provides stiffness against various cyclic loading conditions (rotating movement, gravity, wind). Figure 2-2 shows schematically the different type of spar designs using one or for larger wind blades two spars or a so-called box design.
At the outer surface of the wind blade often a gelcoat is applied to protect the composite material for factors, such as heat, moisture, salty condition and ultraviolet light. The quality of the gelcoat e.g. the amount of voids (small entrapped air bubbles) can have a significant influence for the inspection of the internal structure.

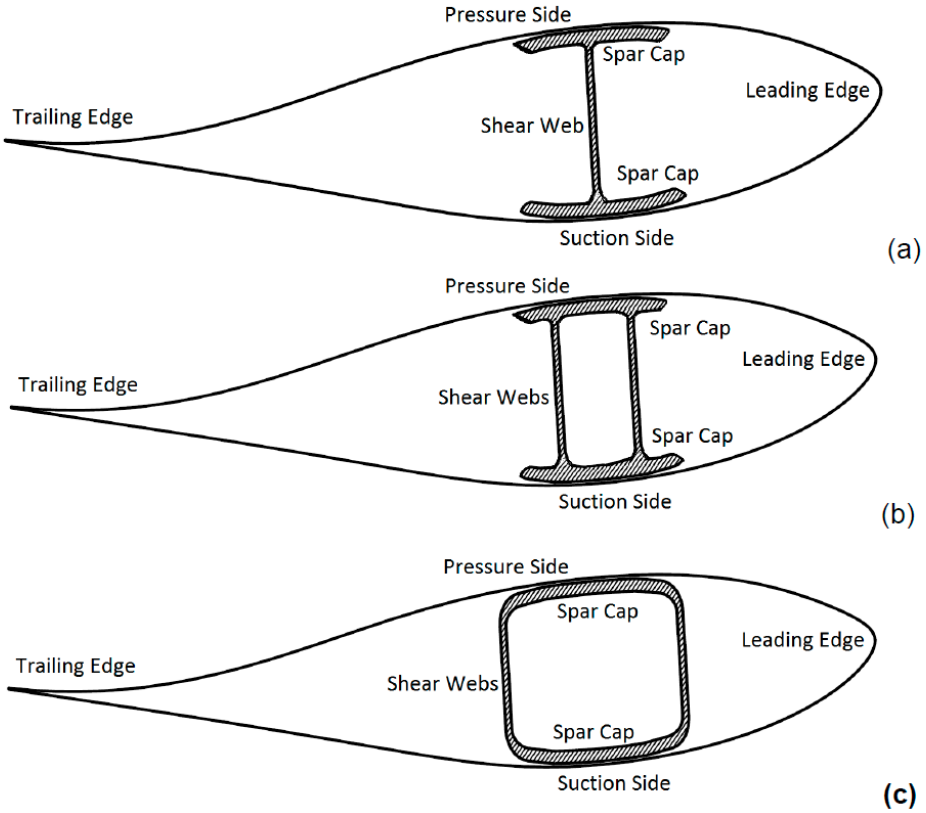

Figure 2-2: Schematic view of a typical wind blade section with a single (a), double (b) and a box beam (c) core structure [Ref.1]

For the in-service inspection three type of internal defects considered that must be detected by means of NDT: delamination in the skin, debonding between spar and skin and debonding between skin and core material. The defect can be introduced in the wind blade due to Foreign Object Damage (FOD), e.g. bird- or lightning strike, by fatigue loads or caused by high static load(s).

2.2 NDT Reference specimens

Consortium partner LM-Windpower provided 3 full-scale wind turbine blades for the AIRTuB project. One blade divided in four sections is provided to the TU-Delft and a complete one to the HZ University of Applied Sciences. Two blades are delivered to the NLR. One complete wind turbine blade which is used for drone experiments is located at the NLR drone centre, see Figure 2-3.

Figure 2-3: Full-scale wind turbine blade for drone experiments

The second blade is delivered in sections as can be seen in Figure 2-4, NLR mid-section 1 is selected as base material to manufacture detailed Inspection Reference Panels (IRP).

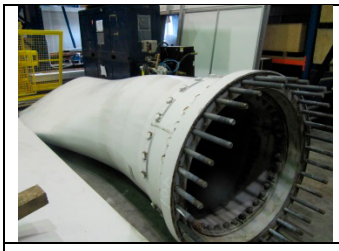			
NLR root-section Dimensions: L 5.20m x W 1.80m-Ø1.32 x H 0.55 - Ø1.32m Thickness: 25-16 mm	NLR mid-section 1 Dimensions: L 5.07m x W 1.77-1.33m x H 0.54-0.37mm Thickness: 15-12 mm	NLR mid-section 2 Dimensions: L 5.05m x W 1.32-0.96m x H 0.35-0.2m Thickness: 14-10 mm	NLR tip-section Dimensions: L 4.16m x W 0.94-0.67m x H 0.2 m Thickness: 10 mm

Figure 2-4: Overview of the NLR sectioned turbine blade

The cutting scheme can be seen in Figure 2-5, the section is cut in two halves, chord direction and in span direction. In total 6 cutting lines will remove respectively the top and bottom skin, resulting in:

- Two “full-scale” reference parts of ~2x1.70m (one bottom side, one top side) including a part of the leading edge, 2 spar connections and an intact trailing edge, see Figure 2-6 ;
- The two “full-scale” reference parts are accessible from the inside by means of milling for applying artificial defects;
- From area 1 to 4 several small reference panels are cut (only skin configuration). The areas 5 to 8 represents a skin/spar connection.

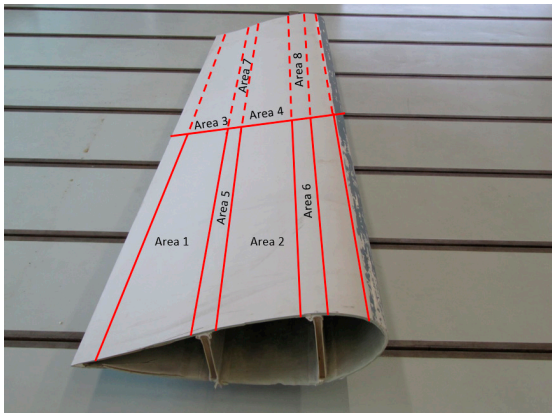

Figure 2-5: Cutting scheme of NLR mid-section 1

Figure 2-6: Two "full-scale" reference parts of ~2x1.70m (one bottom side, one top side)

The sectioned wind turbine blade is used to investigate the possibilities for inspection for internal defects. In total 15 panels for three consortium partners; TU-Delft, Dutch Terra Hertz and NLR are manufactured, see for overview of the detailed IRP panels Figure 2-7. The IRP numbers used in the experiments of the NLR are IRP1, IRP4, IRP10, IRP13 and IRP27.

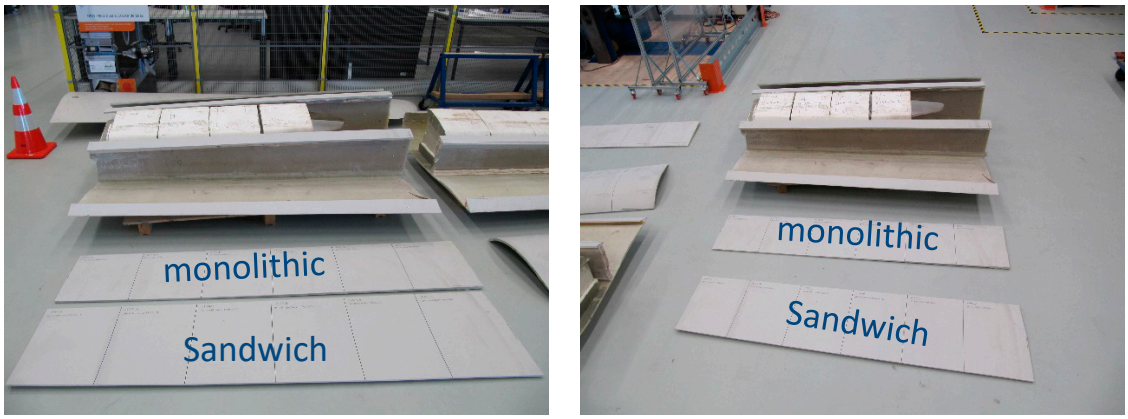

Figure 2-7: Overview of the detailed IRP panels

The reference panels are manufactured by NLR and the different five configurations are described below, each consortium partner is provided with almost an identical set of reference panels. To determine all geometrical parameter the panels are scanned with 3D structural light technology, see Figure 2-8.

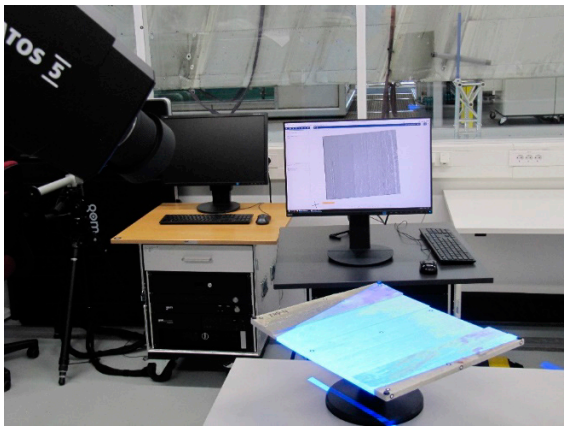

Figure 2-8: Setup 3D structural light technology

IRP1 Relative flat monolithic skin part:

IRP1 is a monolithic reference panel made of Glass Reinforcing Plastic (GFRP). The panel is extracted from a relative flat part of the NLR mid-section 1 turbine blade. Figure 2-9 shows an overview of IRP1.

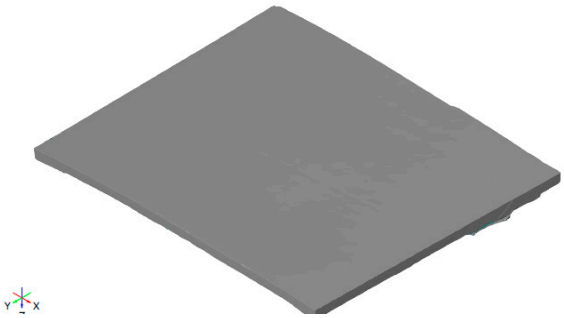

Frontside

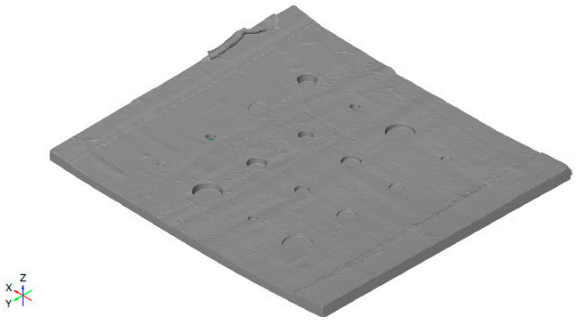

Backside

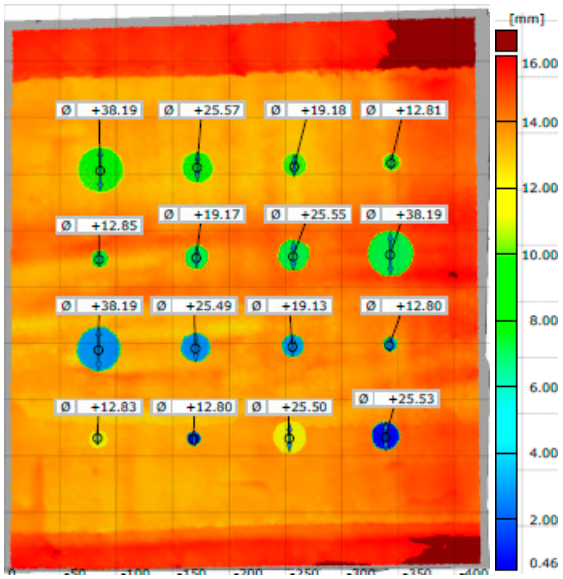

Actual FBH diameters

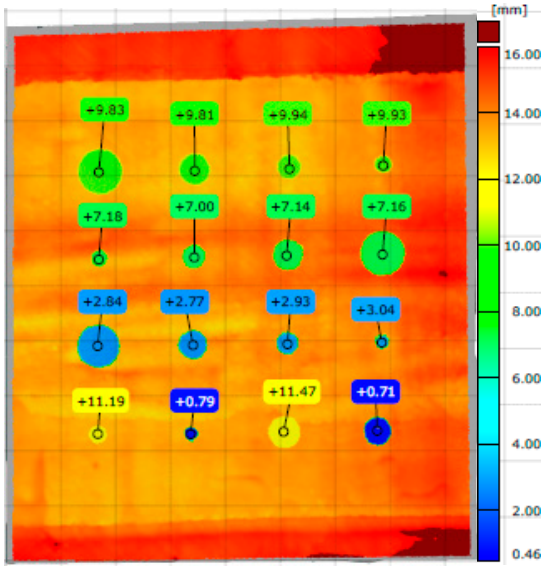

Actual remaining material

Figure 2-9: Overview of reference panel IRP1

To simulate internal delamination damage, Flat Bottom Holes (FBH) are applied to the panels. In real life delaminations can be caused by Foreign Object Damage (FOD) by means of a bird, lightning strike or static/dynamic overload(s). The diameter and actual remaining material above the FBH's for IRP1 can be seen in Figure 2-9. The applied diameters are 0.5 inch (12.7mm), 0.75 inch (19.1 mm), 1 inch (25.4 mm) and 1.5 inch (37.1 mm). The depth of the FBH's are evenly divided w.r.t. the total thickness of the IRP. Further, 0.5 inch and 1 inch diameter FBH's are positioned near the front and backwall and serve to determine the near and far surface resolution of the ultrasonic inspection.

IRP4 Relative flat monolithic skin stepwedge:

To estimate the more or less general attenuation values of the GFRP material a stepwedge was manufactured, see Figure 2-10.

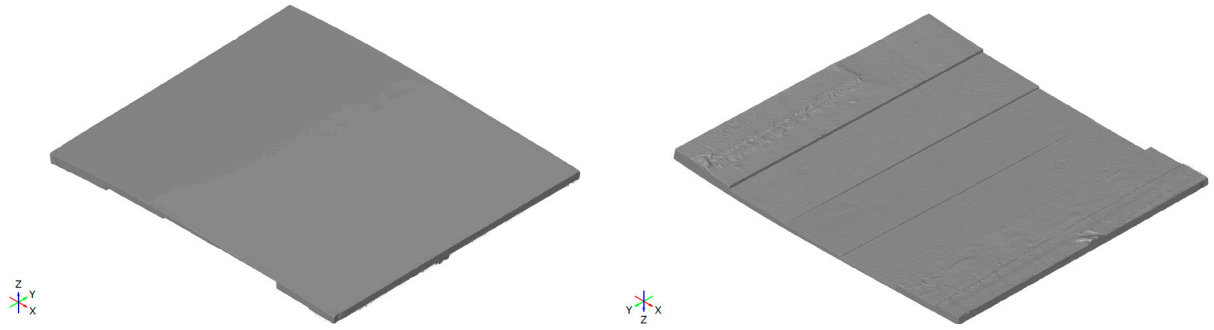

Frontside *Backside*

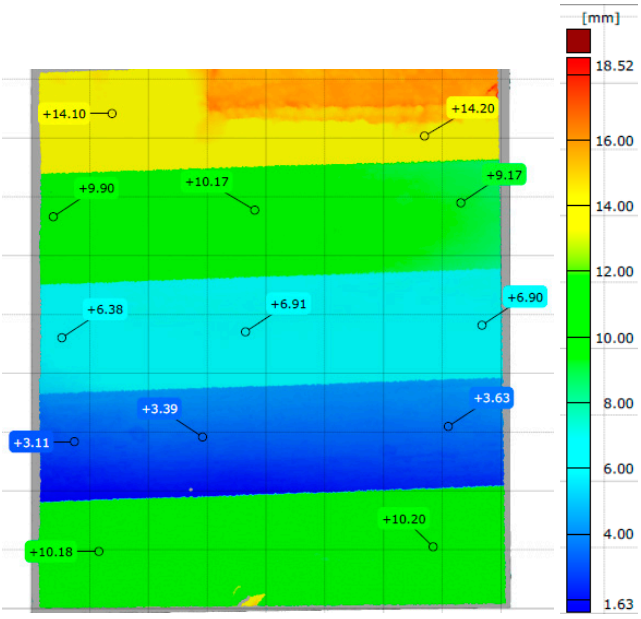

Figure 2-10: Overview of reference panel IRP4 showing the different thicknesses

IRP10 Relative flat sandwich skin:

IRP10 represents the sandwich areas of the wind turbine rotor, which is more located at the aft side of the blade towards the trailing edge. The sandwich material consist of balsa wood as indicated in Figure 2-11. The inserted FBH's are positioned at the both interfaces between the sandwich material and the GFRP skin. The inspections are performed from the outer side of the skin. Due to high porosity content of the balsa wood it is not possible to penetrate this material with ultrasound. Therefore, it can be concluded that the FBH's positioned at the inner side of the balsa wood cannot be detected with the ultrasonic method.

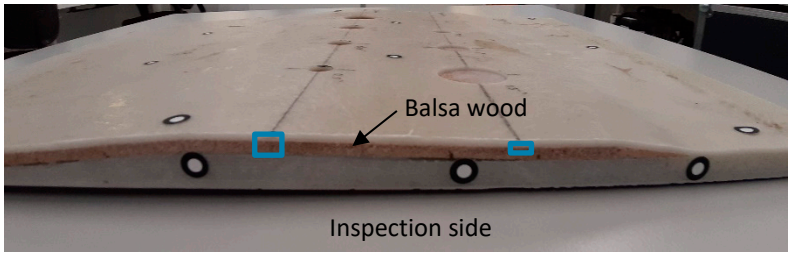

Figure 2-11: Side view of IRP10 showing the position of the balsa wood, inspection side and depth positions of the FBH's

Figure 2-12 shows all geometrical dimension of the IRP10 panel and the FBH's.

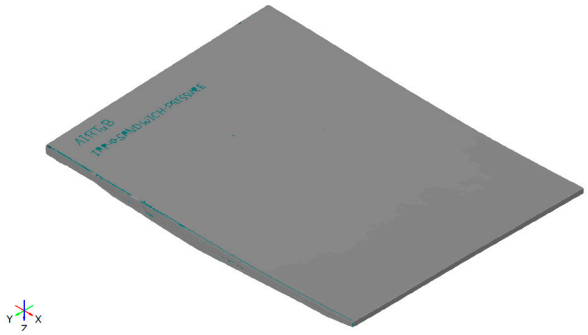

Frontside

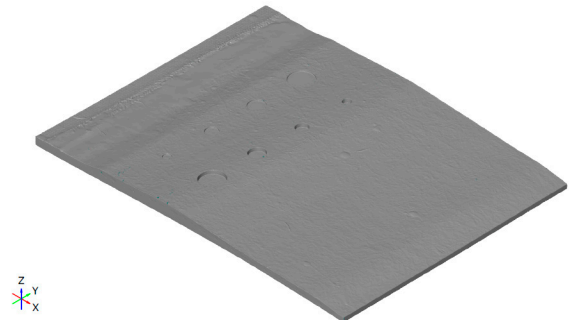

Backside

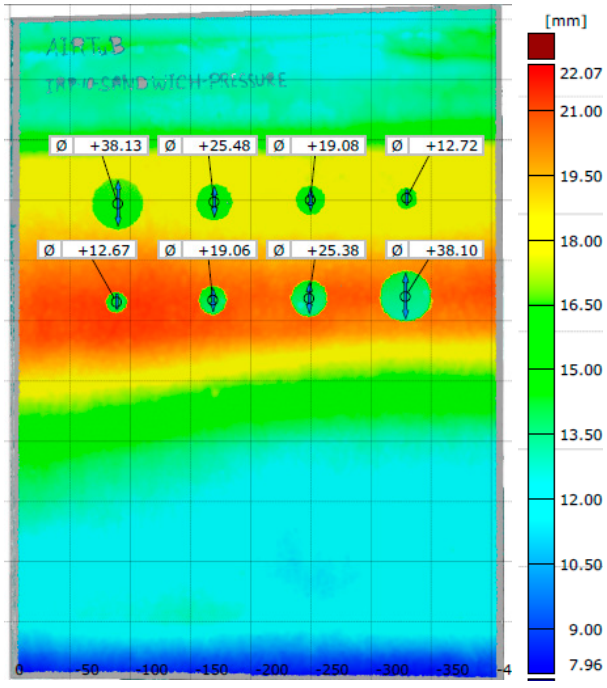

Actual FBH diameters

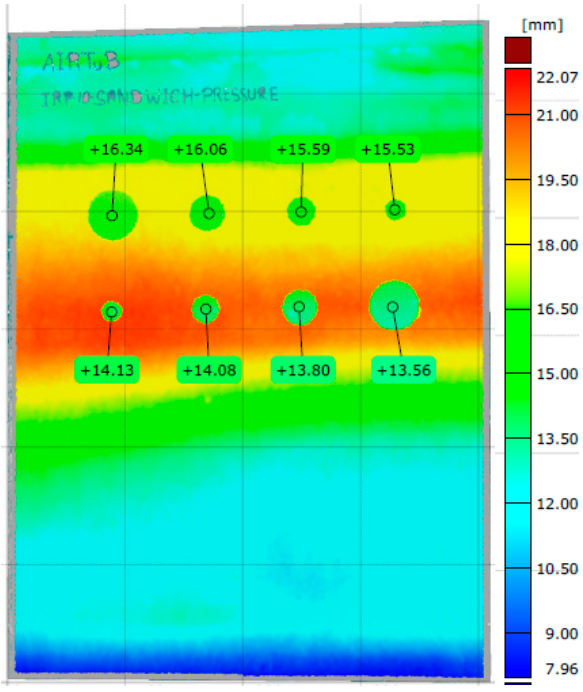

Actual remaining material

Figure 2-12: Overview of reference panel IRP10

IRP13Curved monolithic skin part:

Figure 2-13 shows all geometrical dimension of the IRP13 panel and the FBH's. The panel is highly curved as it is a part of the leading edge of the wind turbine rotor.

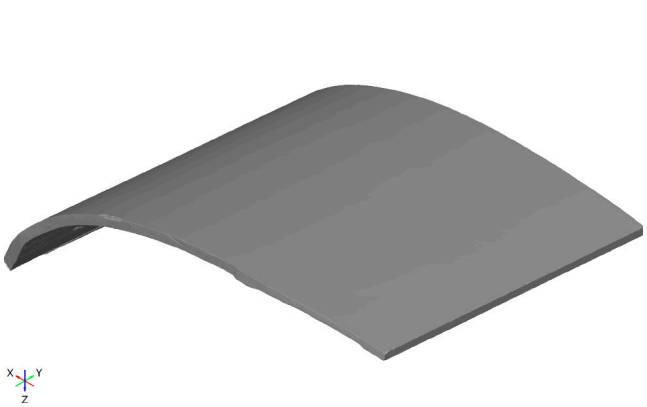

Frontside

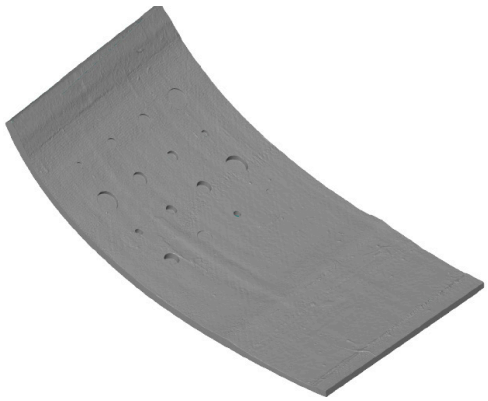

Backside

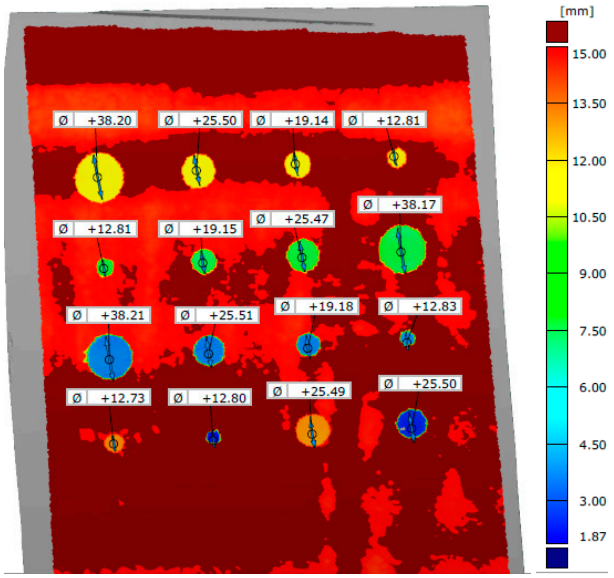

Actual FBH diameters

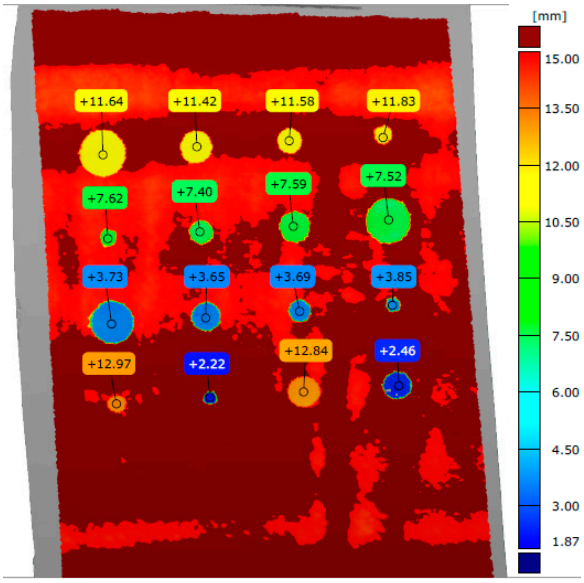

Actual remaining material

Figure 2-13: Overview of reference panel IRP13

IRP27 Skin/spar bonded connection:

IRP27 represents a bonded connection between the skin of the wind turbine rotor and the internal spar, see Figure 2-14 . The dimensions are length 800 mm, width 100 mm and thickness skin 15 mm.

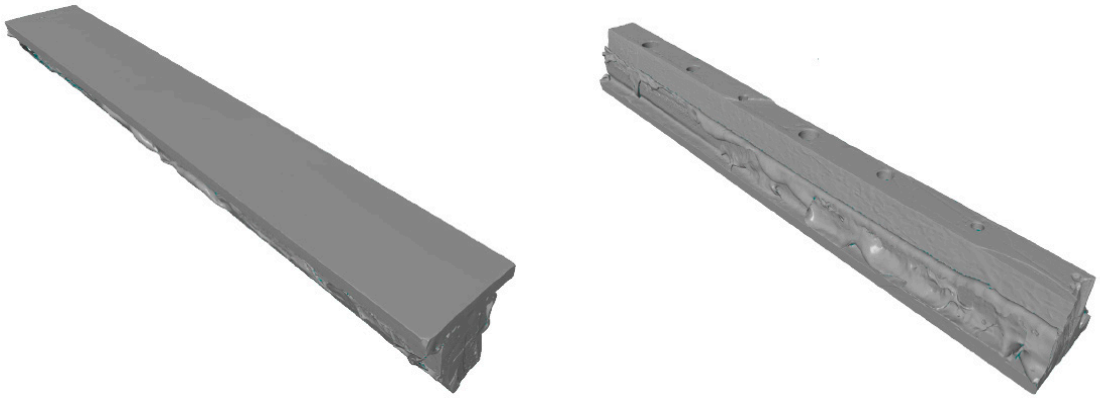

Frontside *Backside*

Figure 2-14: Overview of reference panel IRP27

A detailed view of this bonded connection can be seen in Figure 2-15. In total 3 diameter FBH's are inserted in IRP27, 0.5 inch (12.7mm), 0.75 inch (19.1 mm) and 1 inch (25.4 mm) respectively on two depth positions as indicated in Figure 2-15.

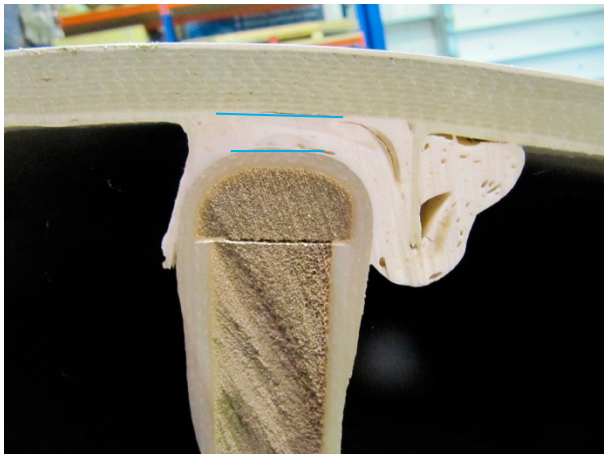

Figure 2-15: Detailed view of IRP27 showing the skin/spar bonding connection and the depth positions of the FBH's

2.3 Quality assessment reference specimens

The dashed rectangular area in Figure 2-16a shows a section of the blade through which the samples were cut for cross-section (CS) observations and CT-scan analysis. The direction of the arrows corresponds to the plane of observation in optical microscope. The schematic overview/representation and the cross-section of the composite wind turbine blade structure is presented in Figure 2-16b. The structure of the composite is composed of unidirectional (UD) fibre bundles, which are stacked on top of each other inside the epoxy resin. Each layer of bundled unidirectional fibres are stitched to supporting backing bundles with different orientation. An overview of the turbine blade structure including fibre glass, epoxy matrix and defects is shown in low-magnification optical microscopy image in Figure 2-16c.

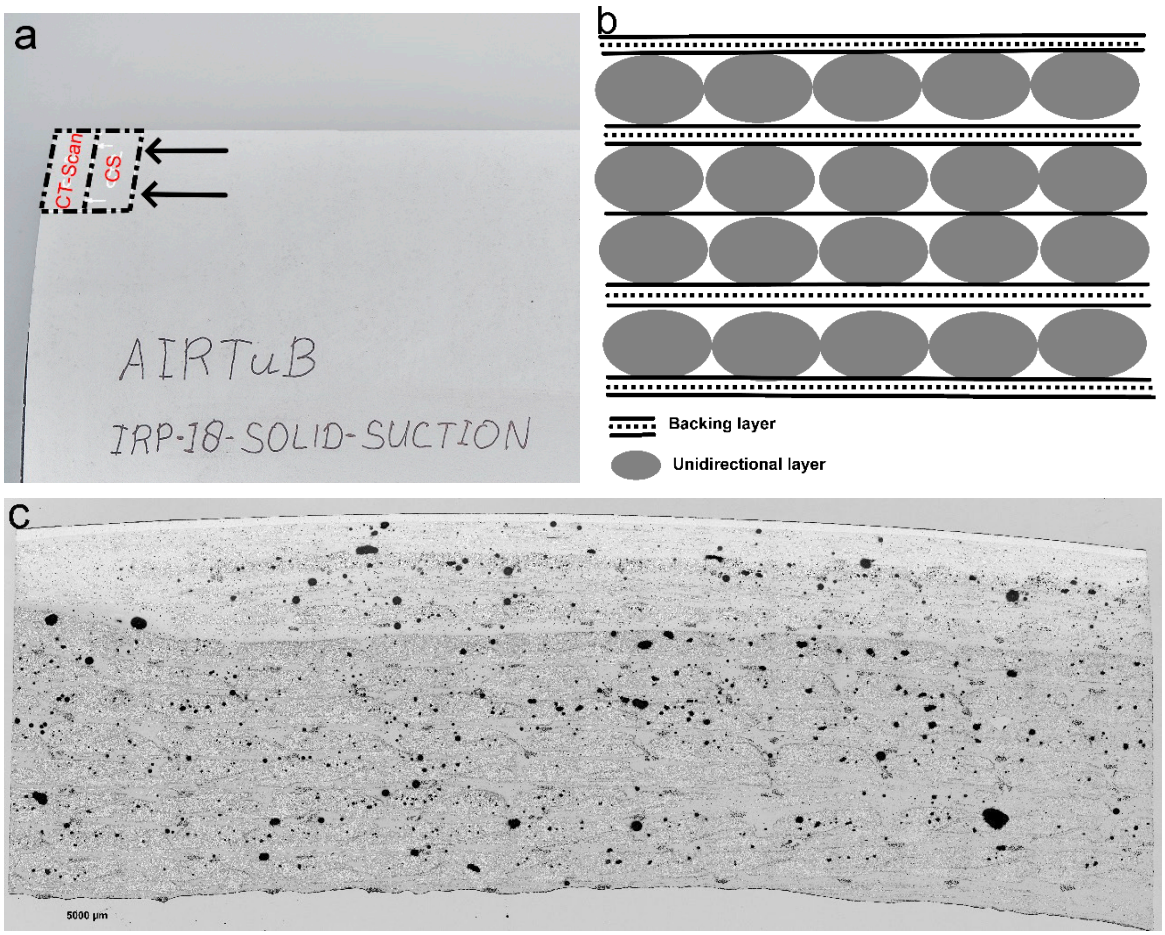

Figure 2-16: a) Sample location for cross-section and CT-scan analysis, b) schematic presenting the stacking sequence of the composite strcuture, c) optical microscopy image showing an overview of the cross-section

Figure 2-17 illustrates high magnification optical microscopy images of the structure with more detailed features. Fibre bundles in different directions through the cross-section are shown in Figure 2-17a. Besides, ultra-fine and large porosities in the matrix also fibre-rich area can be seen in Figure 2-17b. Cracks are also observed in the fibre-rich area. They most probably nucleated at the interface of the fibre and matrix and then propagated through several fibre-matrix interfaces leading to debonding of fibre and matrix.

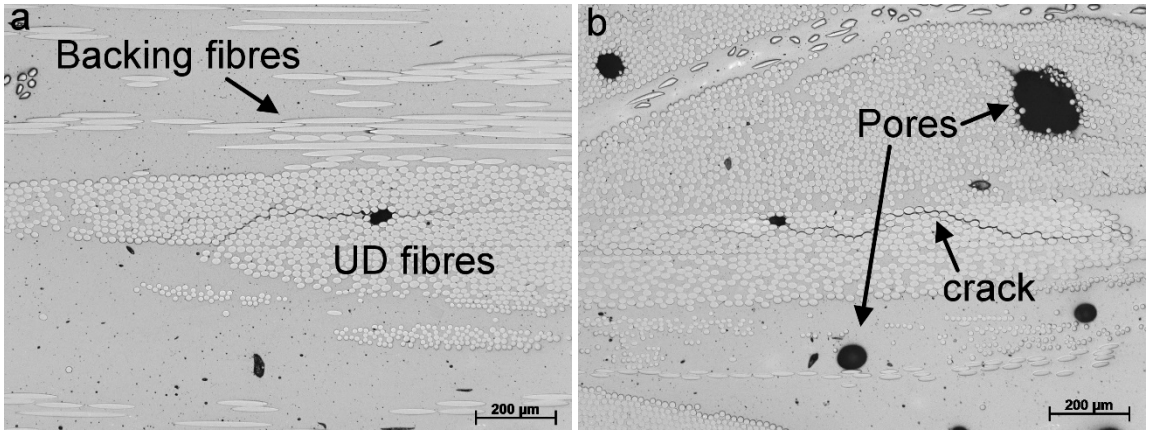

Figure 2-17: a) and b) High magnification optical microscopy images of the cross-section of the wind blade

The 3D rendering of reconstructed X-ray CT-scan data of a sample is shown in Figure 2-18. The stacked bundles of the unidirectional fibres can be clearly observed from 3D reconstructed image of the CT-scanned area. The unidirectional fibre bundles and also backing fibres are shown in top-view and side-view images of Figure 2-18b and Figure 2-18c, respectively.

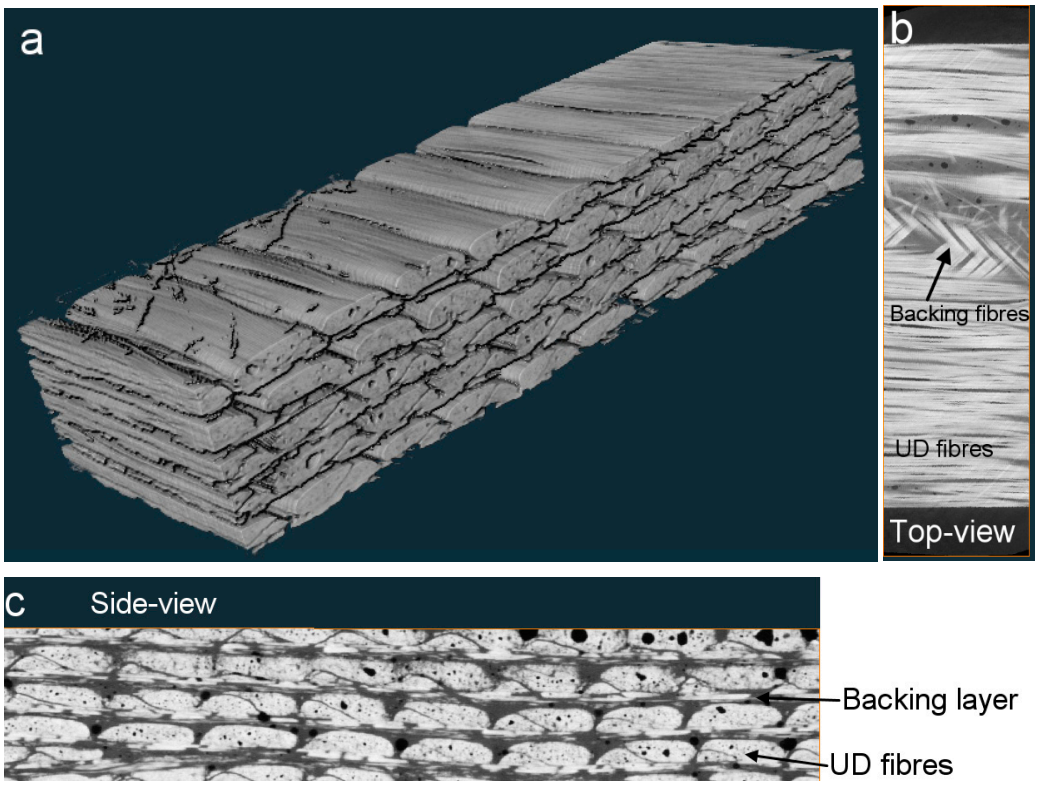

Figure 2-18: a) 3D tomography of the wind blade, b) top view and c) side view of the structure

The porosities are further analysed by Avizo image processing software. Unsharp masking is first applied to sharpen the edges without increasing the noise. It includes applying of Gaussian filter and then mixing it with the original image. The undesired effects are eliminated or reduced using a mask to sharpen the interest area. It is followed by median filter to reduce the pepper and salt noises in the image. The 3D distribution of the detected porosities is shown in Figure 2-19a. Figure 2-19b presents an overlay of 3D rendered image of the scanned area and detected porosities. As can be observed, the porosities are mostly elongated along the bundle of unidirectional fibres. The mean volume of the defects obtained using CT-scan analysis is 0.006 ± 0.07 mm^3 .

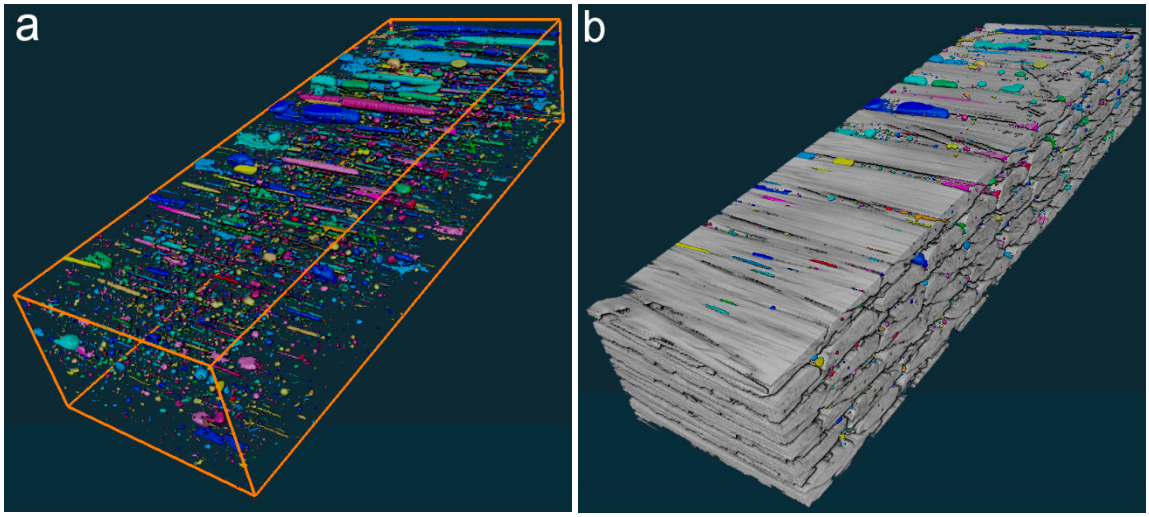

Figure 2-19: a) 3D distribution of porosities detected by CT-Scan b) an overlay of the detected defects and 3D rendered structure of the composite structure

Based on the test results of the cross-sections and the CT-scan analysis is can be concluded that high attenuative material is a quite challenging assignment to inspect with the ultrasonic method.

3 Inspection methods

Based on the literature “Survey on Remote Inspection of Offshore Wind Turbine Blades” (ref.1), the ultrasonic-based NDI methods is found to be the most practical approach in terms of miniaturization possibilities and damage detection possibilities in thick composite material. The phased array ultrasonic inspection method is selected, this method may provide practical solutions with respect to relative low payload and coverage of the inspection area. The conventional ultrasonic C-scan inspection is used as a baseline inspection, specimens are immersed and due to the application of focused transducers an optimum sensitive and resolution is achieved.

3.1 Baseline ultrasonic C-scan inspection

Ultrasonic C-scan inspection of the specimens was performed on Inspection Reference Panels (IRP): IRP1, IRP4, IRP10, IRP13 and IRP27, the test data provides a baseline. The test results of the in-situ and remote Phased Array Ultrasonic Testing (PAUT) will be compared to the ultrasonic C-scan baseline results. Ultrasonic Testing (UT) is a primary technique for the quality control of composite specimens, and provides a 2-dimensional plan view of internal defects in the material. The UT technique makes use of high-frequency ultrasonic waves, in fact propagating mechanical vibrations with a frequency in the range of about 1-50 MHz. Because air is not an adequate transmitting medium for ultrasonic waves, a coupling medium is generally used between the transducer and material. This can be realised in different ways; after manufacturing UT inspection is often carried out with the part totally immersed in water or with the water-jet method where the ultrasonic beam is collimated in a narrow water beam, see Figure 3-1.
When an ultrasonic beam is directed onto a material surface, both reflection and transmission of the waves will occur at the material interfaces. The ratio of the reflected and transmitted parts depends on the angle of beam-incidence and on the difference in acoustic impedance (product of material density and wave velocity). Material defects constitute extra interfaces and these will result in extra reflection signals and in a decrease of the transmitted signal.

a) Immersion method

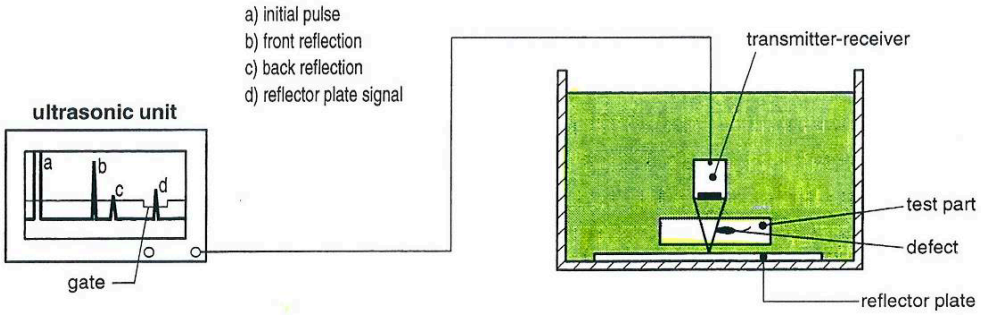

b) Water-jet method

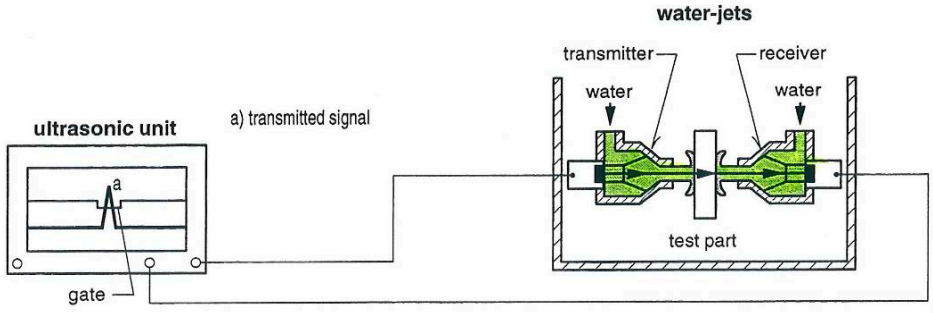

Figure 3-1: Acoustic coupling methods in ultrasonic testing

Immersion inspection was performed on the reference panels IRP1, IRP4, IRP10, IRP13 and IRP27 using the set-up for monitoring the backwall. Due to the high attenuative character of the wind turbine blades (see Section 2.3) relative low test frequencies (500kHz and 1 MHz) are applied. The transducer is focused on the front surface of the reference specimen. The gate of the ultrasonic unit is placed over the backwall reflection (signal 'c' in Figure 3-1a). This signal, for sound material, is set at 80% full screen height (FSH) of the ultrasonic unit.

Inspections were carried out using C-scan equipment of Ultrasonic Sciences Ltd., serial number S618/1, see Figure 3-2. The equipment is a 12-axis scanner (scan window of 4.0 x 2.5 x 2.5 m) that can be used both in the immersion and squirter inspection mode. Complex geometry components (double curved) can be scanned with both the pulse-echo and through-transmission technique.

Figure 3-2: NLR ultrasonic C-scan equipment

Figure 3-3 shows an overview of the references panels immersed in the water tank. All panels were corrected for contour (in particular IRP13 part of the leading edge) by means of manual Teach and Learn programming. The contour of the front of the panels is programmed by optimising the front reflection (sound beam normal to the surface) and adjusting the transducer-part-distance to the focus distance of the transducer, the last illustrations of Figure 3-3 shows the programmed surface mesh of IRP13.

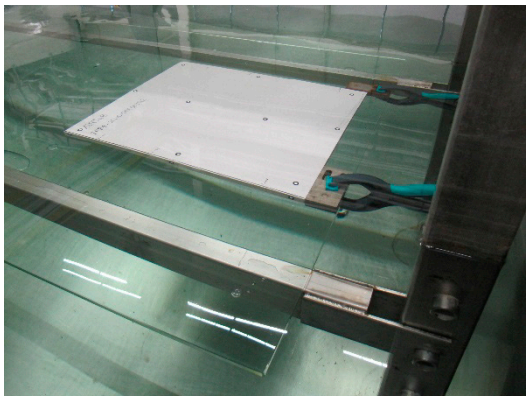

IRP1

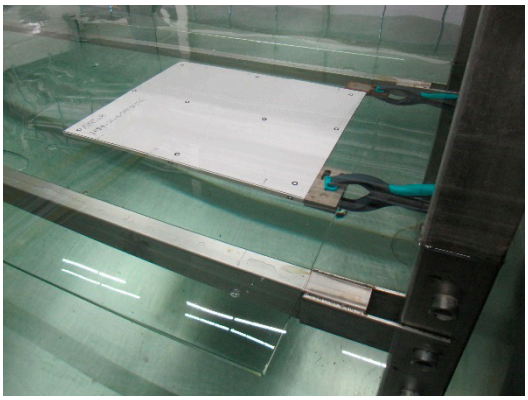

IRP4

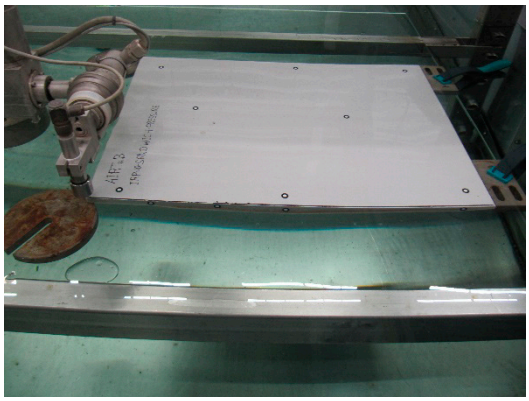

IRP10

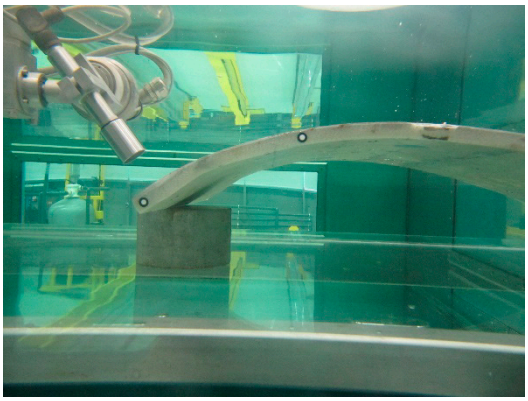

IRP13

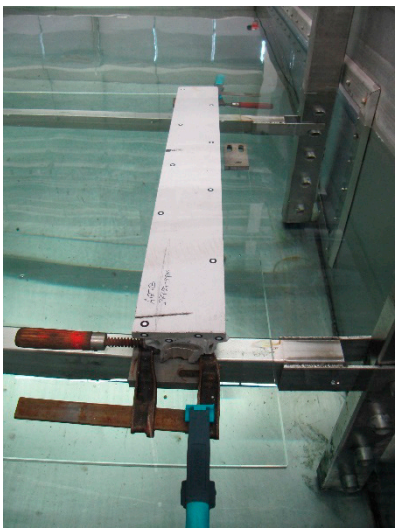

IRP27

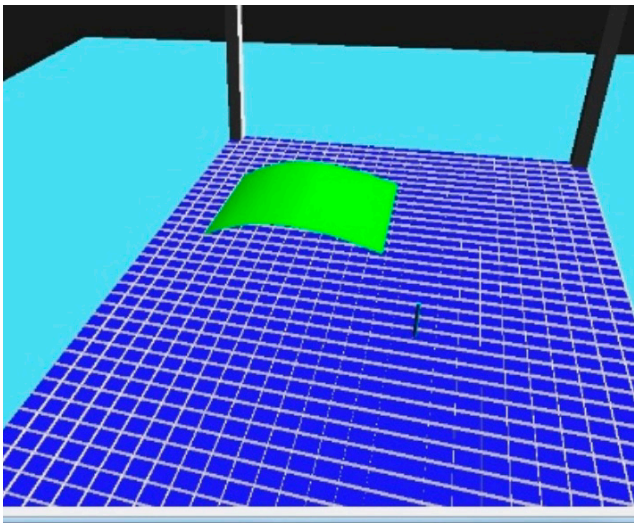

IRP13 programmed surface mesh

Figure 3-3: Set-up of the reference panels in the immersion tank

During this investigation the following two presentations are used:

- A-scan: During ultrasonic inspections reflection and transmission signals can be displayed and analysed on a scope (A-scan). Depending on the material condition attenuation/reflection of the sound beam due to the microstructure or local defects can occur. The time difference between reflected signals gives information about the “defect” depth in the material. The time-base provides the depth information in [µs] or [mm] and the other axis the amount of sound energy received by the probe in [dB] or [%FSH] (Full Screen Height).
- B-scan: B-scan display, front and side view of specimen cross-sections. The B-scan display or presentation is a profile (cross-sectional) view of the test specimen. In the B-scan, the time-of-flight (travel time) of the sound energy is displayed along the vertical axis and the linear position of the transducer is displayed along the horizontal axis. From the B-scan, the depth of the reflector and its approximate linear dimensions in the scan direction can be determined.
- C-scan display, a plan view of the scan area, using colours or shades of grey to show variations in attenuation or thickness.

3.2 Phased Array Ultrasonic Testing (PAUT)

Phased Array Ultrasonic Testing (PAUT) is a widely accepted ultrasonic method for inspection of aircraft parts. Instead of using a single transducer and beam, the PAUT technique uses multiple ultrasonic elements (currently up to 256 elements) that can each be driven independently. Similar to conventional ultrasonic inspection, a coupling medium is required between the transducer and material. The Phased Array (PA) transducers can have a different geometry, for example linear array (elements aligned along an axis), matrix array (elements in checkerboard design) and annular array (elements in concentric circles), see Figure 3-4.

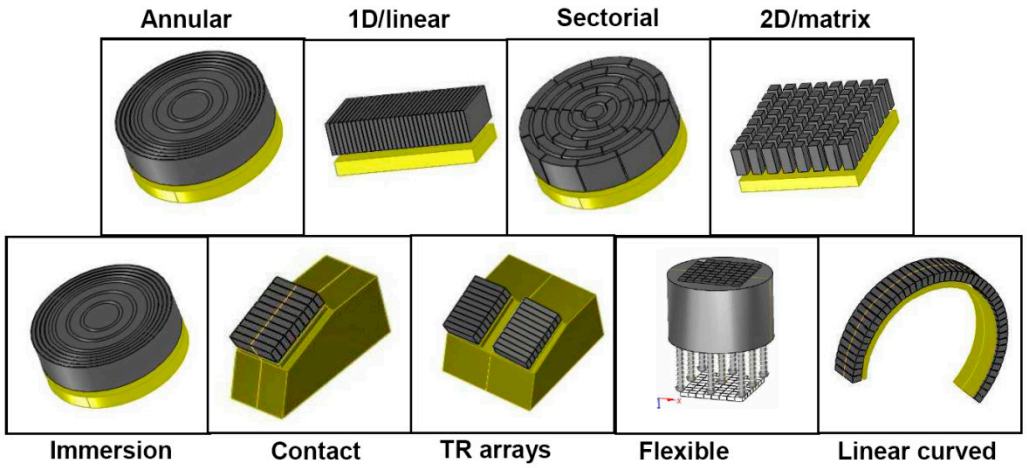

Figure 3-4: Examples of phased array transducer configurations (ref. Olympus)

Different electronic time delays applied to the elements create beams by constructive and destructive interference. The PA beams can be steered, scanned, swept and focused electronically, see Figure 3-5.

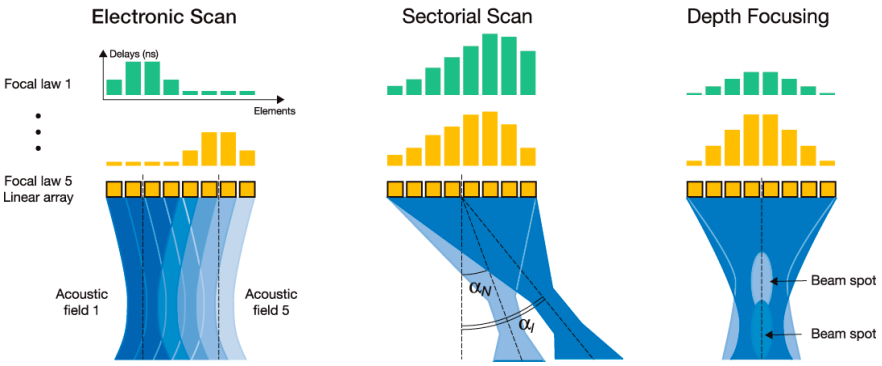

Figure 3-5: Time shifting wave fronts enables linear scanning, angulating/sweeping and focussing of the sound beam (ref. Olympus)

These actions can be combined almost arbitrarily, hence achieving a maximum of flexibility in terms of sound field control. Specific advantages of the PAUT technique are:

- Electronic scanning of a test part by the selective activation of different elements of the array transducer. This enables the scanning of a larger surface area and can replace the relatively slow scanning with a single transducer mechanical system.
- Electronic focusing at different depths to increase the detectability of defects at specific depth, by application of electronic delays to the different transducer elements.
- Electronic steering to enable the inspection of different parts of the specimen without moving the transducer itself, by varying the angle of beam incidence. The electronic steering also allows the inspection of part geometries which are not inspectable with conventional transducers (e.g. near edges in thick components, and geometry changes such as thick-thin transitions, radii, corners, etc.).

The same presentations (A-scan, B-scan and C-scan) are used as during the baseline C-scan inspections.

Inspections were carried out using Omniscan-M-PA16-128, see Figure 3-6 The following main specifications applies:
- Suitable for in-service inspection.
- Number of focal laws 256.
- Automatic probe recognition.
- Max. aperture 16 elements.
- Max. number of elements 128.
- Pulse voltage 40 or 80V per element.
- Receiver gain from 0 to 74 dB.
- Encoder input possible.

Figure 3-6: NLR ultrasonic phased array equipment the Omniscan-M-PA16-128

4 CIVA modelling

Phased Array Ultrasonic Testing (PAUT) is more complex than conventional UT inspection and the PA transducers are quite expensive. Modelling of UT-PA can be a tool to provide more insight in the technique, to optimise defect detection and to make the inspection more cost-effective. CIVA is a software platform developed by Extende to simulate NDT imaging and signal processing. The platform consists multiple modules:

- Ultrasonic Testing (UT)
- Ultrasonic Testing Analyses
- Guided Waves Testing (GWT)
- Structural Health Monitoring (SHM) (Guided waves)
- Electromagnetic Testing (ET)
- Radiographic Testing (RT) with X-Ray and Gamma Ray
- Computed Tomography (CT)

For the purpose of this project the focus of CIVA will be on the Ultrasonic Testing module.

4.1 Functions of UT

Each module have their dedicated function which in the case of UT includes: Beam Computation, Inspection Simulation, and Composites.

4.1.1 Beam computation

Beam computation function of the UT module is intended for simulating the ultrasonic field produced by a particular transducer in a defined material. Therefore, the user defines many of the test parameters such as the specimen and transducer settings, that will go on to be used in the next inspection simulation function.

Specimens

When defining the specimen the geometry and materials of the test part are required. For geometry, CIVA accommodates both simplistic preset (blocks, cylinder, cones, etc.) that can be adjusted, and importing 3D CAD models (in STEP or IGES format) of parts that are custom made. The materials of the test part can be selected from a library of isotropic or anisotropic materials which can be further adjusted to be representative of the actual part. These factors such as form, dimensions, roughness, homogeneity, density, etc. are crucial to the accuracy of the beam computation as they all directly affect the propagation of the sound waves through the specimen.

Transducers

Once the user has defined the specimen to be tested, they also need to select the appropriate probe. This selection can be made from the CIVA library that contains many of the commercial off-the-shelf probes. If a desired transducers is not included in the library then it can be custom defined in the platform to be the same as the actual probe to be used. For this project, Phased Arrays are going to be most relevant type of probes and examples of the different types of arrays that are feasible in CIVA are shown in Figure 3-4.

With specimen and the transducer defined, the final steps in the sequence for beam computation can be executed (see *Figure 4-1*). The position of the beam computation needs to be set. For the most relevant beam computation, the position of the transducer and the surrounding media must be the same as the setting for the Inspection simulation

function of the UT module. The user can further modify the focal laws, but if the phased array is chosen from a library then the default laws are automatically imported. With all the computation parameters set the user can click Run and obtain the beam computation results. Depending on the complexity of the settings the run times can take anywhere between couple of mins to couple of hours.

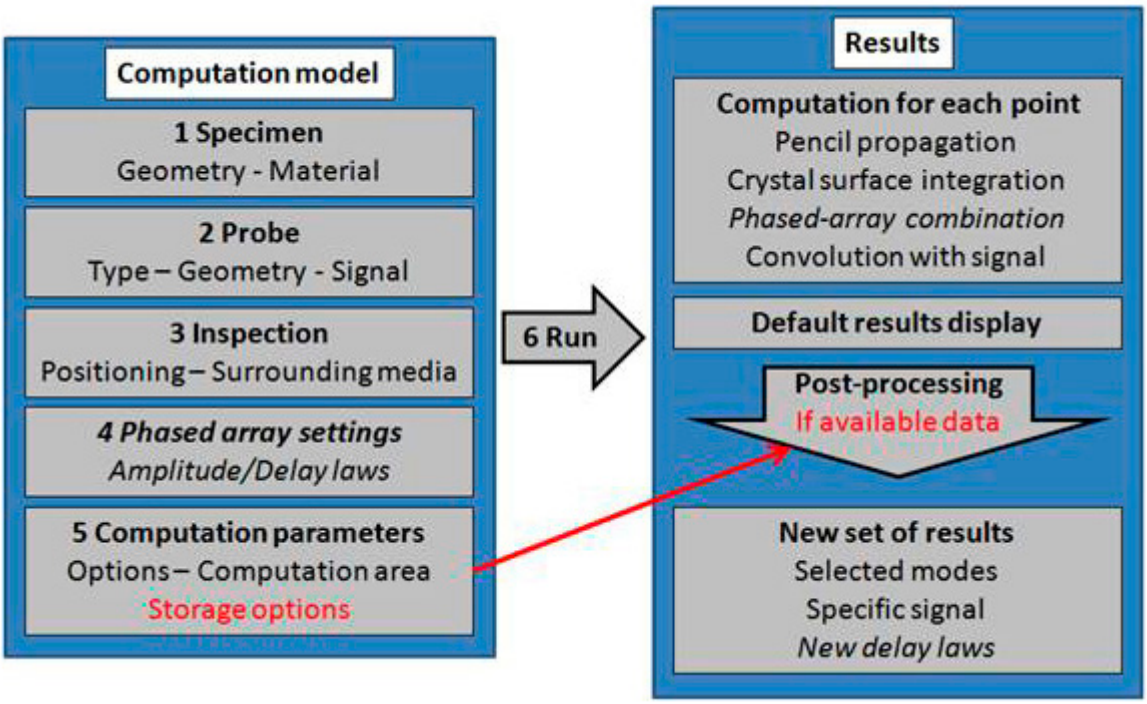

Figure 4-1: Initiation and sequence of UT beam computation

4.1.2 Inspection simulation

The Inspection simulation function is intended for simulating the ultrasonic examination of a test part with flaws. Much like the Beam computation function, the user has to define the parameters of the simulation such as specimen, probe, inspection, phased-array settings, but now includes a new step: flaws settings. These flaws can be numerous, of different types (side drilled hole, flat bottom holes, notches, etc.), and at different locations and orientations. Therefore, full flexibility to achieve realistic flawed components. Additionally, aside from conventional inspection the simulation settings can be set to use techniques such as (Full Matrix Capture) FMC and DDF. However, these techniques can significantly rise the run time due to the increased steps in the computation sequencing. For example, a linear phased array with 128 elements, 32 element aperture, scanning 6 Flat Bottom Holes on a composite block took about 3 hours using conventional focal laws. However, with 4-step DDF, the run time quadrupled to almost 12hours[1]. The default results include images of A-, B-, C-, and D-scan but given available data the user can choose other relevant ways of showing the analysis such as overlaying images in the specimen.

[1] These runs were conducted on a desktop with: Intel Xeon Gold 5218 CPU @2.30GHz, 256GB RAM

4.1.3 Composites

The Composites function is essentially the same as Inspection simulation but with the focus on composite material. While the active model used in this function follows the same UT principles, the differences comes with the types of specimens, materials and defects that are simulated. The four types of specimens dedicated for composites are: simple composite laminate (planar or cylindrical), curved composite laminate, stiffeners, and complex shaped composite laminate. For each of the specimens the different ply orientations, pattern, and epoxy can be specified for each layer, allowing the digital specimen to be fully representative of the real specimen.

4.2 Additional features

There are additional functions that are shared amongst all the inspection techniques: Batch manager, Parametric and Sensitivity study, and Probability of detection (POD). Batch manager function allows for multiple configurations to be computed in sequence. The user can therefore predefine the configurations and analyse the results all at once rather than having to wait for each run. Parametric and sensitivity study enables the user to define a variation scenario which includes the parameters to be varied and the extent of variation. The two types of parametric studies included are the classical “Parametric Study” and the “Metamodel Technique.” The classical study creates a new CIVA file for each combination of varied parameters, whereas the metamodel generates a database and provides real-time results for all the variations. These metamodels are especially powerful when a large number of evaluations need to be executed much like in POD analysis. POD feature calculates the probability of detection curves for different flaws in a test component following these 5 steps:

1. Defining the parameter for POD, most commonly flaw size
2. Defining the parameters likely to vary in the execution of the inspections
3. Defining the uncertainty distribution of each parameter
4. Run the computations
5. Analyse the results and compute the POD curve

These simulated curves are also known as MAPOD, Model-assisted Probability of Detection analysis. It is cheaper and faster to conduct a MAPOD analysis than an empirical evaluation of multiple physical tests. It is noted that CIVA also enables the user to import empirical data for further analysis.

5 PAUT sliding probe

5.1 Handheld design

Automated Inspection and Repair of Turbine Blades (AIRTuB) project pursues to reduce the downtime during maintenance of the offshore wind blades, by developing an unmanned automated system capable of performing necessary inspections. The unmanned systems comprises of a drone which is used as a carrier to land on a specific area of the wind blade and “drop” a crawler. The crawler makes a meander scan on a suspect area and an ultrasonic phased array probe performs an internal inspection. The PA-transducer needs to be lightweight to fulfil the payload requirements of the drone. Important is that the PA-transducer has a good acoustic coupling to the surface of the wind blade. When positioning a PA-transducer directly on the wind blade surface, a coupling gel is needed, which is not convenient in a unmanned system. To overcome this problem NLR developed its own PAUT sliding probe, see Figure 5-1.

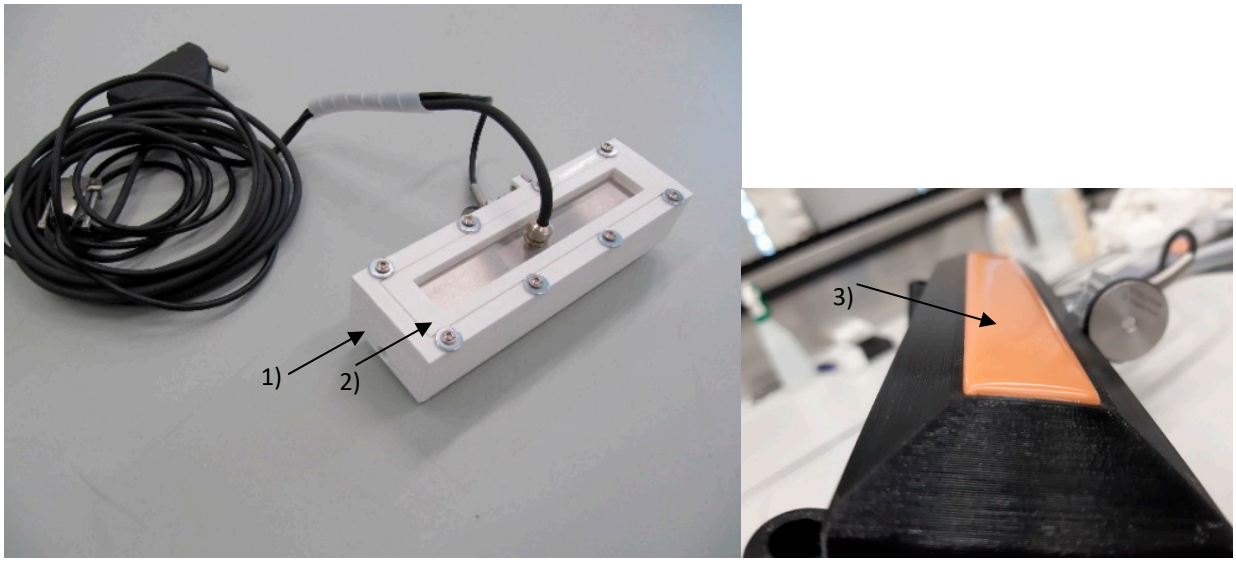

Figure 5-1: PAUT sliding probe developed by NLR

The PAUT sliding probe consists of 3 individual parts: 1) external case 2) casing for the PA-transducer 3) protecting foil. Further an off-the-shelf 500 kHz PA-transducer with 64 elements is inserted into the probe holder. The probe holder is made from lightweight Poly Ethylene Terephthalate (PET) and manufactured using 3D printing. The combination of probe holder and PAUT sensor is further called PAUT sliding probe.

The PA-transducer lay-out and characteristic parameters are illustrated in Figure 5-2 and exact values mentioned in Table 1.

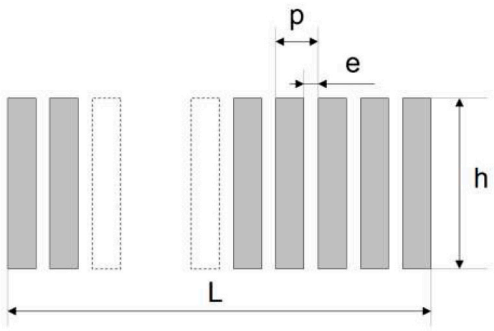

Figure 5-2: Layout of the PA transducer (ref. Imasonic)

Table 1: Parameters PA-transducer

S/N	Frequency [MHz]	Number of elements	Pitch (P) [mm]	Spacing (e) [mm]	Elevation (h) [mm]	Total active length (L) [mm]
147 16 1001	0.5	64	2	0.5	10	127.5

To prevent the usage of ultrasonic coupling gel, a Polyurethane foil of 0.8 mm thickness is placed in front of the transducer, see Figure 5-1. This foil has two functions: 1) protecting the facing of the PA-transducer, 2) establish coupling with only a thin spray of water. It is important that a constant coupling at both sides of the Polyurethane foil is established. To ensure that there is a constant coupling between the PA-transducer face and the foil the assembly is performed at an immersed condition, see Figure 5-3. The immersed condition prevents the possibility of entrapped air.

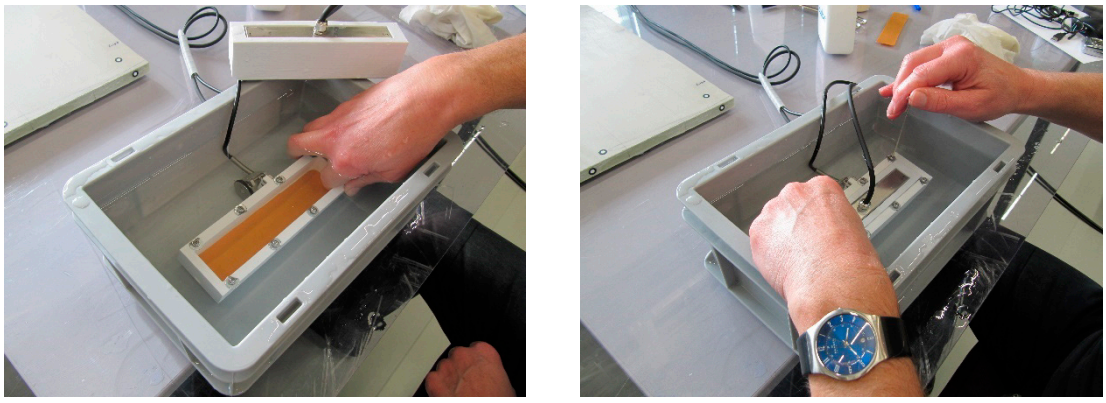

Figure 5-3: Assembly of the PAUT sliding probe under water to ensure no air is entrapped

To evaluate the coupling characteristics of the PAUT sliding probe concept, it is placed (with the protecting Polyurethane foil) on a translucent Perspex plate. Figure 5-4 shows an example that an air bubble is entrapped between the protection foil and the Perspex plate which is a not desirable situation.

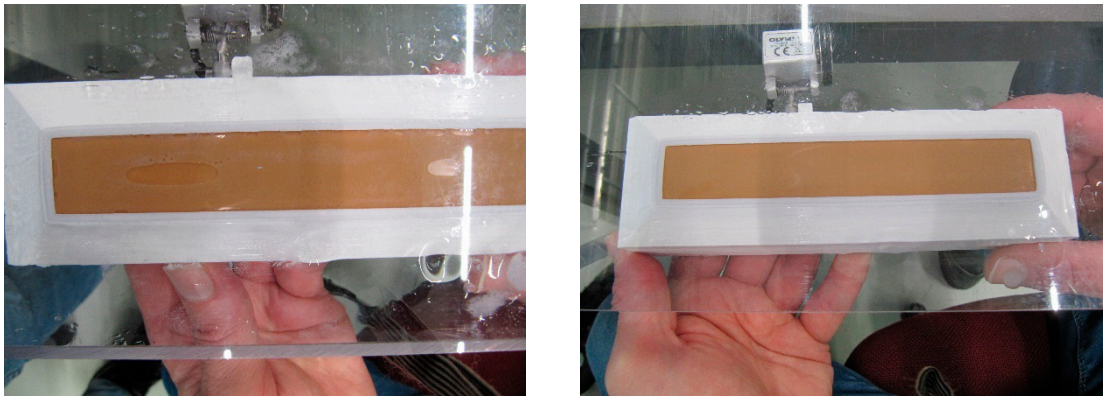

a) b)

Figure 5-4: a) Entrapped air bubble b) Correct coupling

In practice, it turned out that, on the Perspex plate, it is very difficult to remove the entrapped air by sliding the probe. But on the reference AIRTuB specimens, with a certain roughness, entrapped air could be removed quite easily, by sliding the probe. After several assembly sessions it turned out that, when the Polyurethane foil has a slightly convex shape, the coupling could be establish quite easily (no entrapped air) and the resistance to slide the probe was at a minimum, see also Figure 5-5.

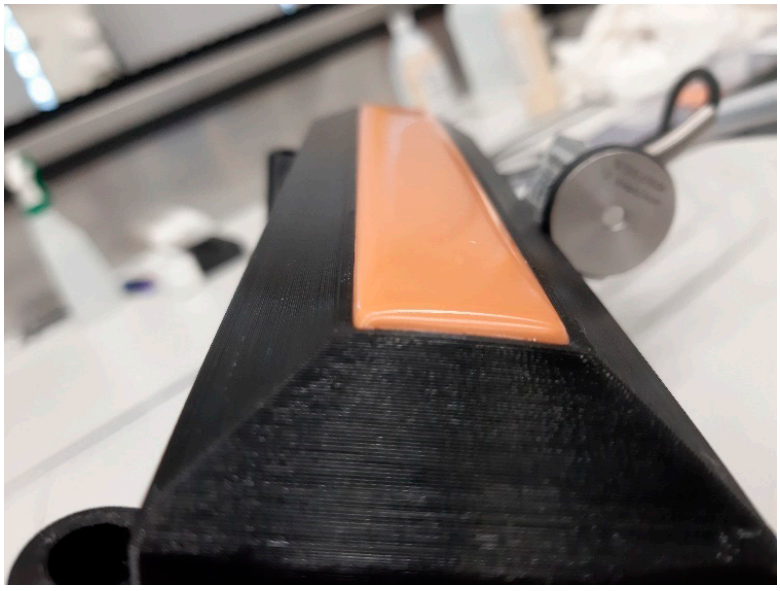

Figure 5-5: PAUT sliding probe with a slightly convex Polyurethane foil

5.2 Sensitivity calibration

Element sensitivity calibration must be carried out to have the same amplitude sensitivity over the complete array. To perform this calibrations, the PAUT sliding probe is set on “sound” material, in this case Perspex of 15 mm, see Figure 5-6.

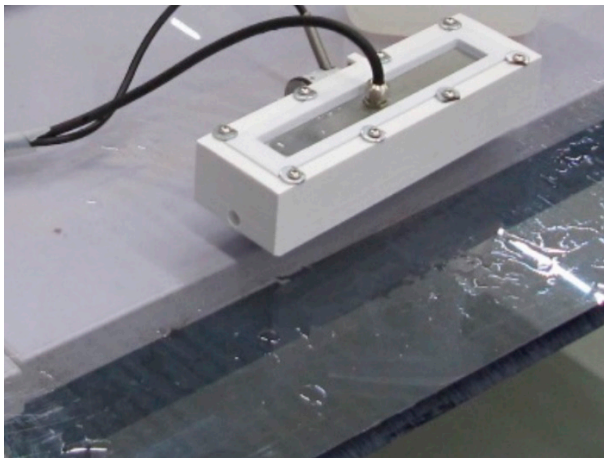

Figure 5-6: PAUT sliding probe placed on 15 mm Perspex plate to perform sensitivity calibration

Figure 5-7 shows the signal output of the complete width of the transducer (64 elements). In this case 8 elements form one aperture to generate a sound beam. Figure 5-7 a shows the PA-transducer output in a not calibrated situation, relative large amplitude differences can be observed. After calibration the output of the PA-transducer is set to 80% FSH with a tolerance of 5 %.

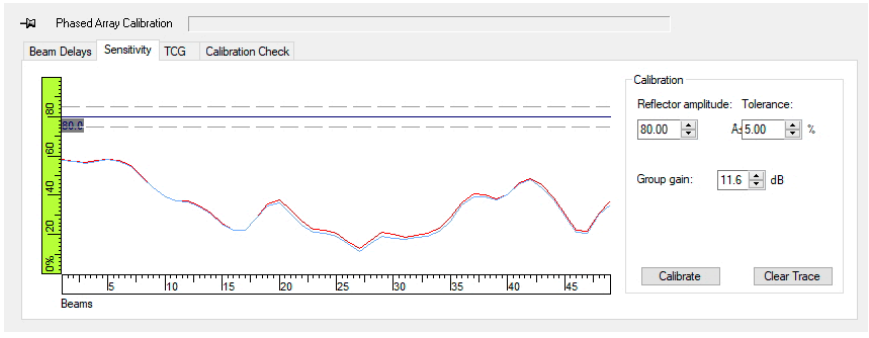

a) Example not calibrated PA-transducer

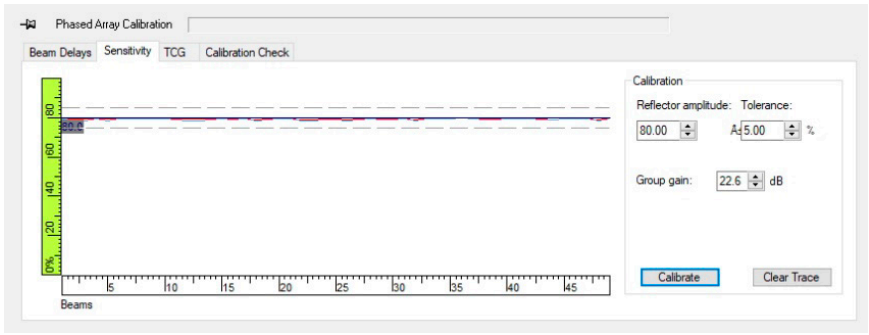

b) Example calibrated PA-transducer

Figure 5-7: Sensitivity calibration of the PA-transducer

5.3 PAUT sliding probe integration crawler

Consortium partner TU-Delft developed an inspection device based on an off-the-shelf phased array roller probe. For integration of this roller probe into the crawler, TU-Delft designed a mechanical structure to hold the phased array roller probe, water spray, analyzer and battery together. Furthermore, this structure has a tilt mechanism which can lift the roller probe up when the inspection is not needed (e.g. moving the crawler from landing position to the area of interest), see Figure 5-8 . This enables remotely positioning of the probe on and off the wind turbine rotor blade.

Figure 5-8: Overview of the crawler of Hoge School Zeeland including the TU-Delft sensor package (ref. HZ & TU-Delft)

A small redesign is performed to integrate the PAUT sliding probe. In principle, the TU-Delft phased array roller probe is replaced by the NLR's PAUT sliding probe from Section 5.1. Figure 5-9 shows the integration of the NLR PAUT sliding probe, see arrow.

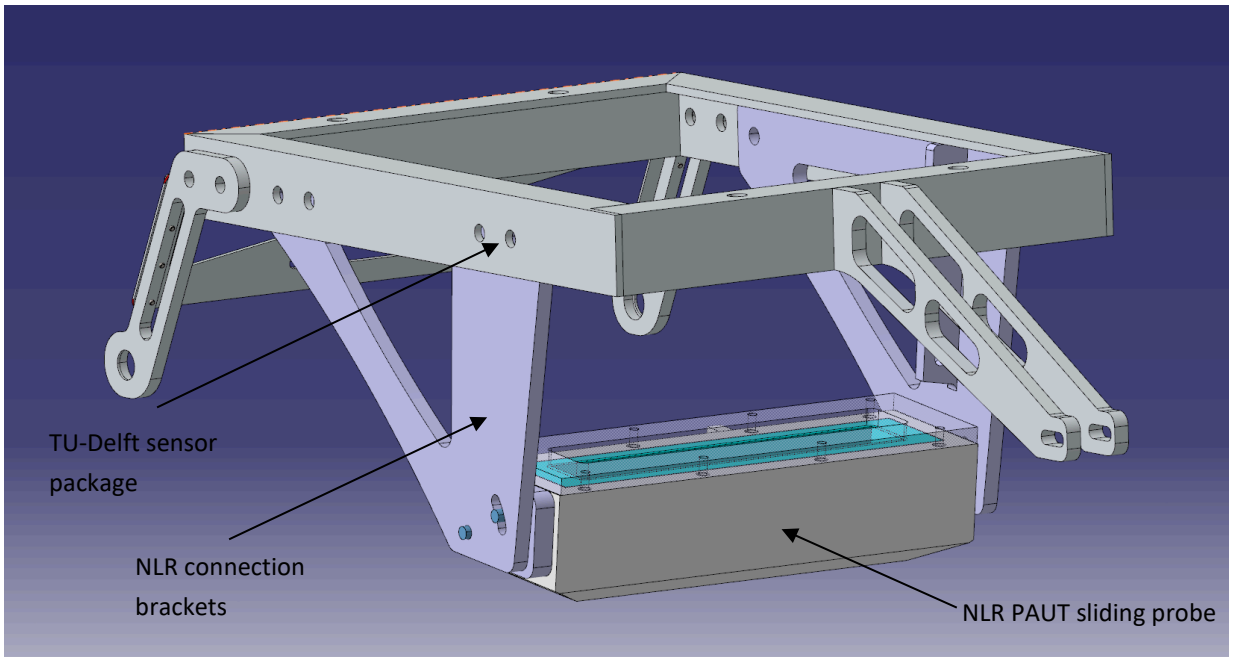

Figure 5-9 NLR PAUT sliding probe integrated in the TU-Deft tilt mechanism

Compared to the handheld design, only two extra brackets are printed to establish a reliable and stable assembly, see Figure 5-10.

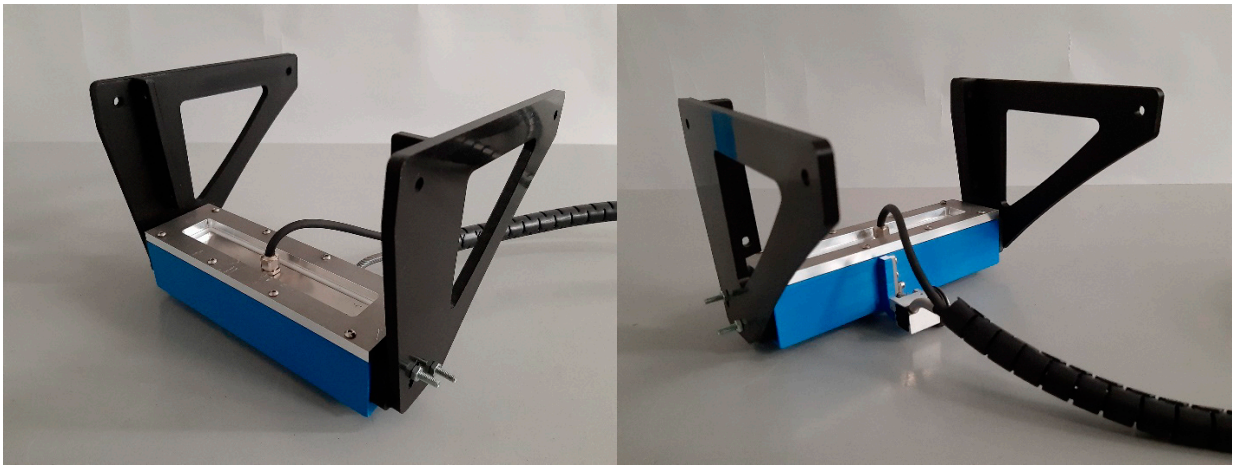

Figure 5-10: 3D printed PAUT sliding probe suitable for integration crawler

6 Baseline UT IRP inspection results

This chapter elaborates on the C-scan results that are acquired on the IRP's from Chapter 2 using the C-scan equipment introduced in Chapter 5. Sections 6.1 to 6.5 presents the baseline C-scan results on each IRP.

6.1 IRP1 Relative flat monolithic skin part

Immersion ultrasonic inspection is performed on IRP1 panel, using the set-up for the pulse-echo method. Due to the high attenuative character of the GFRP material, low frequency transducers are applied respectively 500kHz and 1MHz, both focused type. The linear amplifier of the ultrasonic unit is used. The transducer is focused on the front surface of the specimen. One electronic gate, of the ultrasonic unit, is placed over the Backwall Reflection (BR) signal to collect an attenuation C-scan. A second gate is placed between the Front Reflection (FR) and the backwall reflection to collect a reflection C-scan. The backwall signal for "sound material" is set at 80% full screen height (FSH) of the ultrasonic unit. Sound material can be defined as the best area of IRP1 panel, in other words, the area with the lowest attenuation.
Figure 6-1 shows the attenuation C-scans of IRP1 monitoring the backwall reflection for both 500kHz and 1 MHz transducer frequencies.

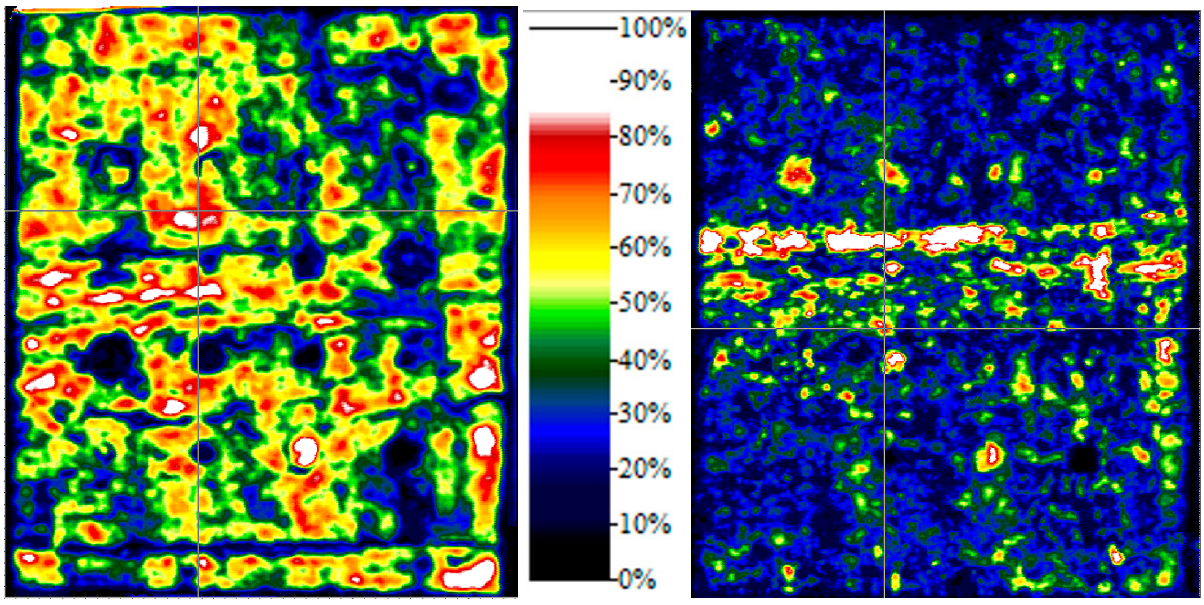

Figure 6-1: Attenuation C-scans of IRP1, 500kHz and 1 MHz, gate on BR

To begin with the 500kHz inspection, the crosshair is positioned at an area with relative "low" attenuation of the sound beam. The amplitude value at this crosshair position is 80% FSH which corresponds with a red/white representation in the C-scan, see also the colour histogram of Figure 6-1. The corresponding A-scan signals can be seen in Figure 6-2. The front reflection (FR) and backwall reflection (BR) can be clearly distinguished in the A-scan presentation. On the other hand, both signals are quite broad and bulky. These "bulky" signals are caused because significant amplification is needed to penetrate the high attenuative material with ultrasound.

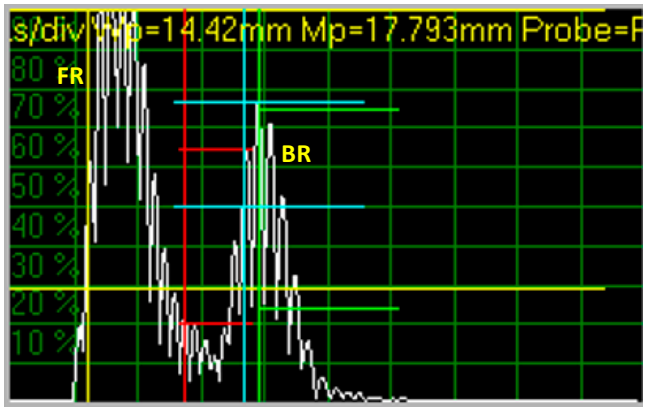

Figure 6-2: A-scan @ crosshair, IRP1, frequency 500kHz, FR= Front Reflection, BR=Backwall reflection, yellow gate =trigger gate, blue gate=TOF, red gate=reflection gate, green gate=backwall gate

Figure 6-1 shows also the 1 MHz attenuation C-scan, the same colour palette applies. The first thing to notice is that the areas red/white, which correspond with a backwall amplitude of 80% , is noticeably smaller. Figure 6-3 shows the A-scan presentation at the position of the crosshair (1MHz C-scan). The backwall reflection cannot be clearly discriminated. When checking the A-scan at other areas of the C-scan, it is noticed that large repeat reflection signals fall in the green backwall gate, meaning that the majority of the red/white areas are not representing the backwall reflection.

Remark: The 1MHz transducer generates an ultrasound beam with a smaller wavelength which is more influenced by the coarse material compared to the 500kHz transducer with a larger wavelength.

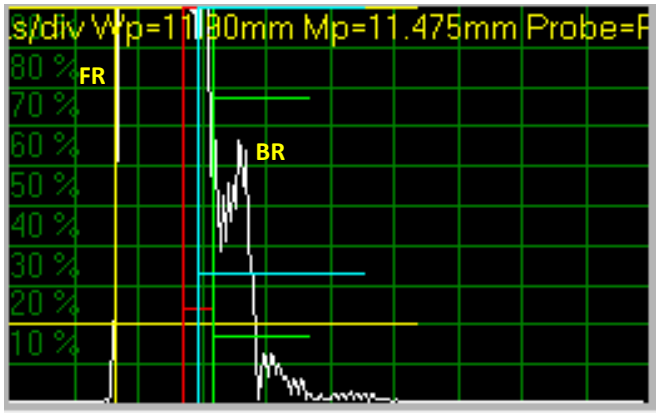

Figure 6-3: A-scan @ crosshair, IRP1, frequency 1MHz, FR= Front Reflection, BR=Backwall reflection, yellow gate =trigger gate, blue gate=TOF, red gate=reflection gate, green gate=backwall gate

Figure 6-2 shows the A-scan of the 500kHz inspection, the red gate, positioned between the FR and BR collects all the reflection signal of the complete thickness of IRP. Figure 6-4 shows the 500kHz reflection C-scan, in general all FBH's are detected with the exception of the FBH's located near the front and backwall. As mentioned before, the FR and BR are quite "bulky" signals, therefore it is not possible to collect reflection signals from the FBH's located close to the front and the backwall of the IRP. It is not possible to achieve enough separations between the signals on the timebase and to collect the FBH's close to the front and the backwall in the reflection gate without disturbing the large FR and BR signals. The FBH's are distinguished w.r.t. the basis material because position and appearance of the FBH's are known. Figure 6-4 also shows the 1 MHz reflection C-scan, as with the backwall C-scan, large high reflection signals mask the reflections signals from the FBH's.

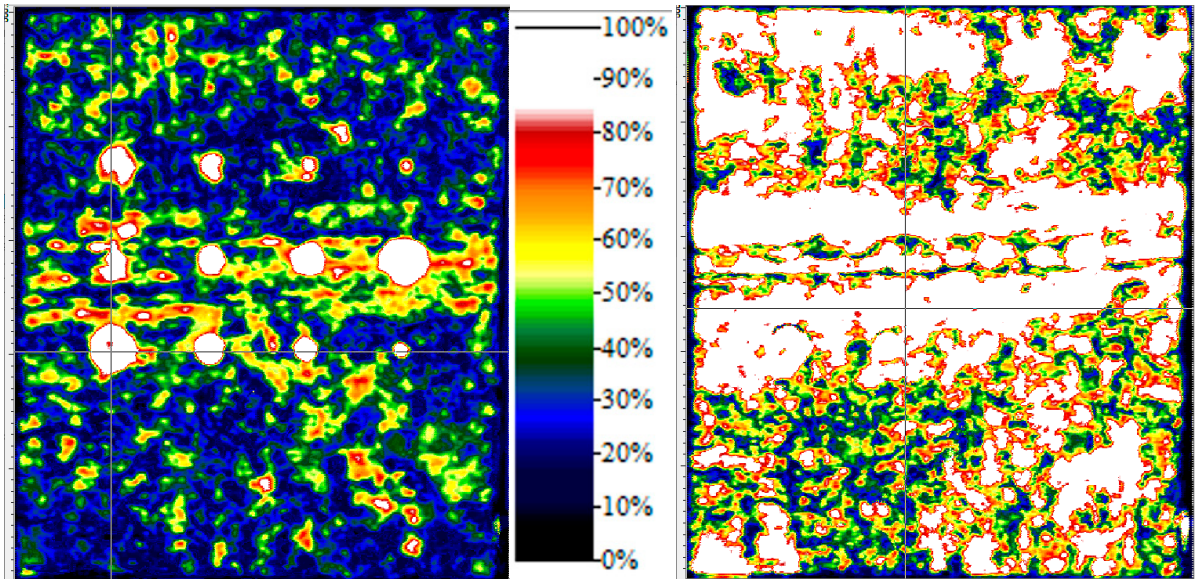

Figure 6-4: Reflection C-scans of IRP1, 500kHz and 1 MHz, gate between FR and BR

Figure 6-5 shows the 500kHz and 1 MHz Time Of Flight (TOF) C-scans. In contrast to attenuation C-scans the TOF represents the duration of the reflection signals measured in [µs] or [mm]. For both, but especially for the 1 MHz, a serious amount of reflection signals are received at approximately 10 mm (green areas) masking for a great part the locations of the FBH's.

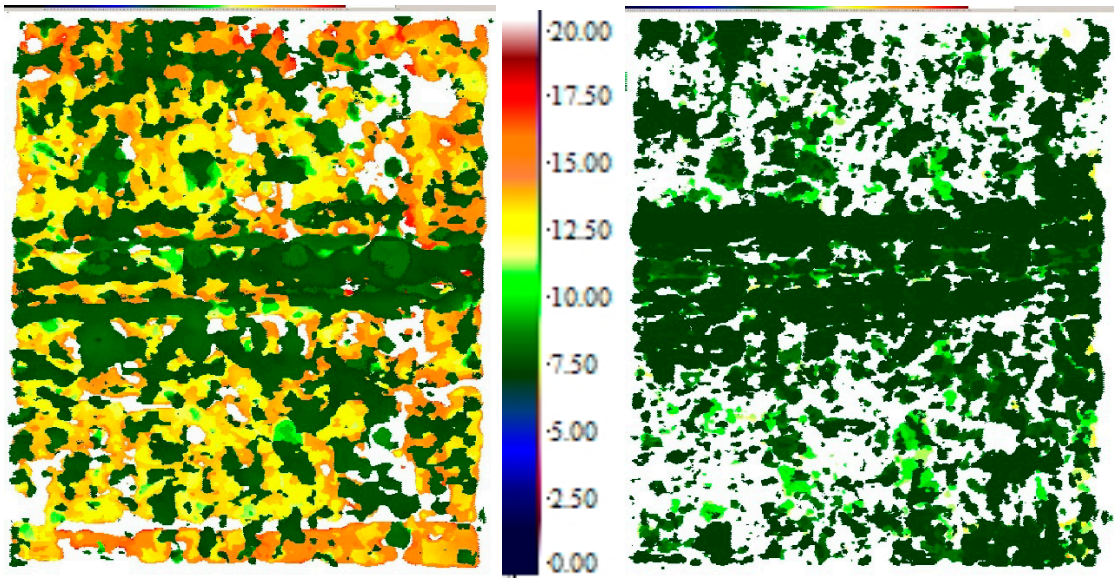

Figure 6-5: Time Of Flight C-scan of IRP1, 500kHz and 1 MHz, gate just after FR and including BR

In general it can be concluded that the high attenuative character of the material needs low frequency transducers. This first trial already indicates that a 1 MHz transducer is already a too high frequency. But also the 500kHz transducer frequency shows quite blurry C-scans. Put it in another perspective, can better results be expected due to the coarse grained high attenuative GFRP material?

6.1.1 Application of DAC/TCG

The ultrasonic settings, especially the preamplification and gain in chapter 6.1.1, are selected to accomplish a backwall signal of 80% FSH. This implicates that the total preamp and gain applies for the total thickness. But for the first part of the thickness, a reduced gain is already sufficient. It is possible to apply an adjustable gain with respect to the thickness, for this a so-called Distance Amplitude Curve (DAC) or Time Corrected Gain (TCG) can be used.
The acoustic signals reflecting from the same size FBH but at different depths will have different amplitudes (using one gain setting). Marking the amplitudes of the FBH's at these different depths gives a DAC Curve. The DAC/TCG was determined on the 1.5 inch FBH's of IRP1. The FBH's are located at the following depths: 2.8, 7.2 and 9.8 mm. In case of thick-walled composite materials the ultrasound beam undergoes a substantial attenuation. To achieve a backwall echo of 80% FSH, without using a DAC, the reflection signals of especially the first part of the specimen thickness goes off-screen. As a result, the interpretation or monitoring of these reflection signals are impossible, see for example the A-scan of Figure 6-6. The reflection signal of FBH Ø 1.5" @ t=7.2mm goes off-screen. As a consequence, the amplitude of the reflecting ultrasound wave cannot be measured. Further, the large amount of amplification results in quite "bulky" signals with hardly any discrimination between them.

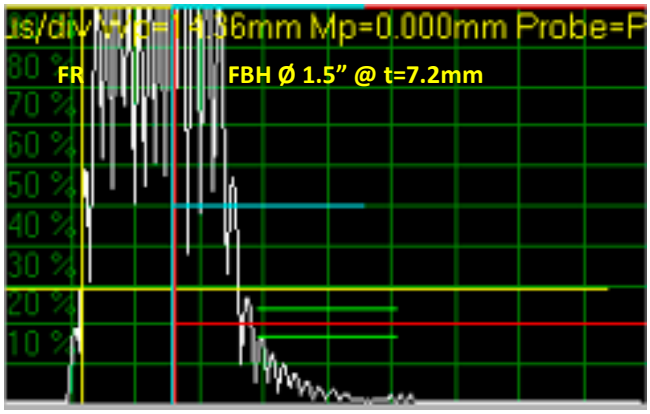

*Figure 6-6: Ultrasonic signal **without** DAC/TCG on IRP1*

Instead of using one gain setting for the total thickness it is possible to use a Time Corrected Gain (TCG). Hereby, it is possible to increase the gain as distance along the time base increases. This provides a constant sensitivity throughout the total thickness of the specimen with reduced disturbing reflection signals from the first part of the specimen thickness, see Figure 6-7. As a result of the TCG the noise signals are significantly decreased.

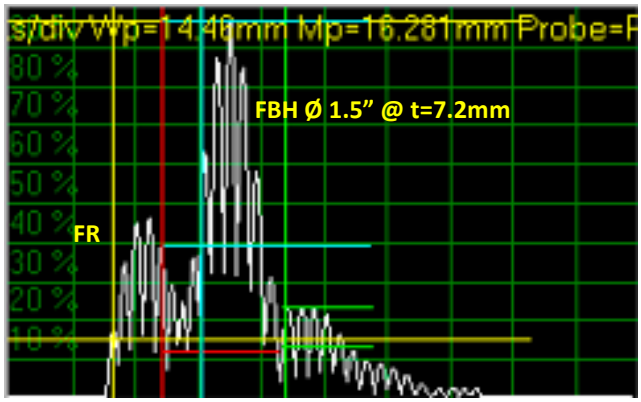

*Figure 6-7: Ultrasonic signal **with** DAC/TCG on IRP1*

The attenuation C-scan test results of IRP1 for both the 500 kHz and 1 MHz inspection can be seen in Figure 6-8. Compared to Figure 6-1 no significant difference can be observed which is explainable, although a DAC/TCG is applied the backwall is still adjusted to 80% FSH.

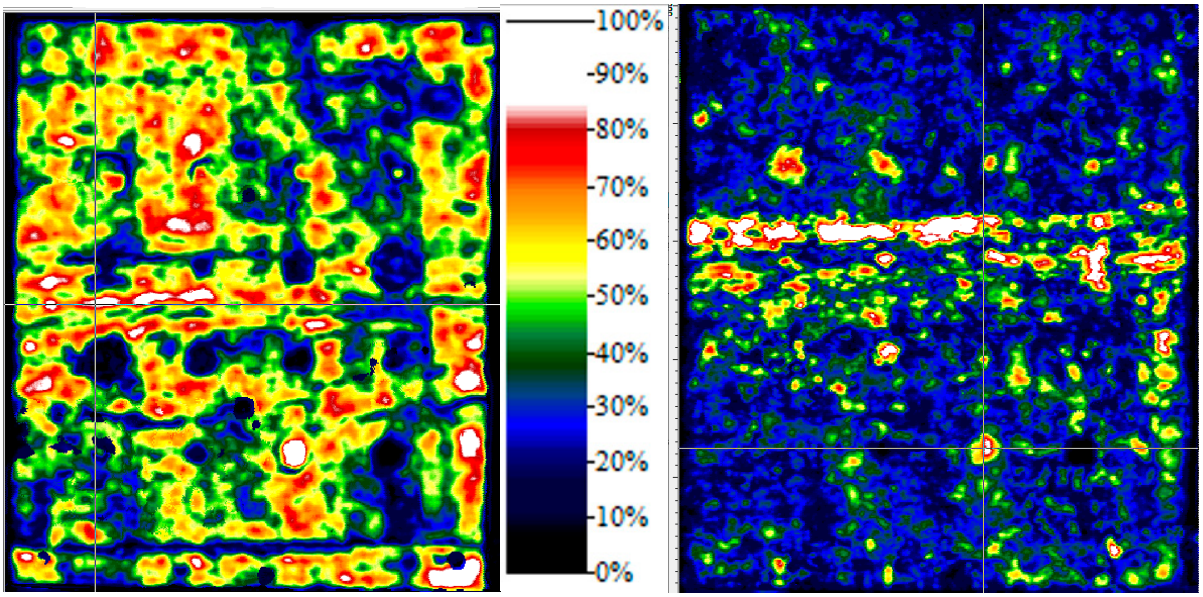

Figure 6-8: Attenuation C-scans of IRP1, with DAC/TCG, 500kHz and 1 MHz, gate on BR

The A-scan of the 500kHz inspection frequency showing the FR and BR at “sound material” can be seen in Figure 6-9. Compared to Figure 6-2 the signals are less “bulky” and the positioning of the red reflection gate is more precise. When analysing the A-scan of the 1MHz C-scan at several positions, it is noticed that large repeat reflection signals falls in the green backwall gate, meaning that the majority of the red/white areas are not representing the backwall reflection.

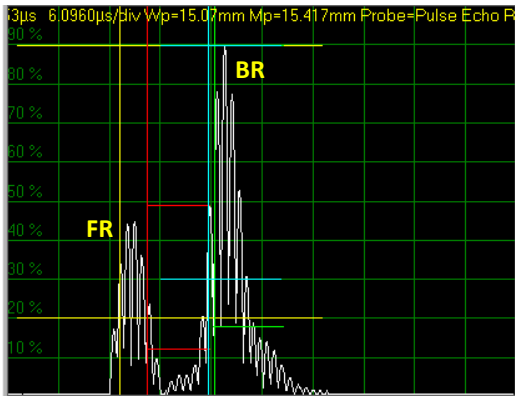

Figure 6-9: A-scan @ crosshair, IRP1, frequency 500kHz, FR= Front Reflection, BR=Backwall reflection, yellow gate =trigger gate, blue gate=TOF, red gate=reflection gate, green gate=backwall gate

Figure 6-10 shows both the 500 kHz and 1 MHz reflection C-scans with DAC/TCG. When comparing the 500 kHz reflection test results without DAC/TCG a considerable improvement can be witnessed. Also the FBH's positioned near the front and backwall are detected reliably with exception of FBH Ø 1.5" @ t=7.2mm. Further, the reflection signals caused by the basis material are significantly reduced. Again, the 1 MHz inspection results contain large reflection signals caused by the coarse grained high attenuative GFRP material in relation with the small wavelength of the sound beam and the FBH's cannot be detected reliably.

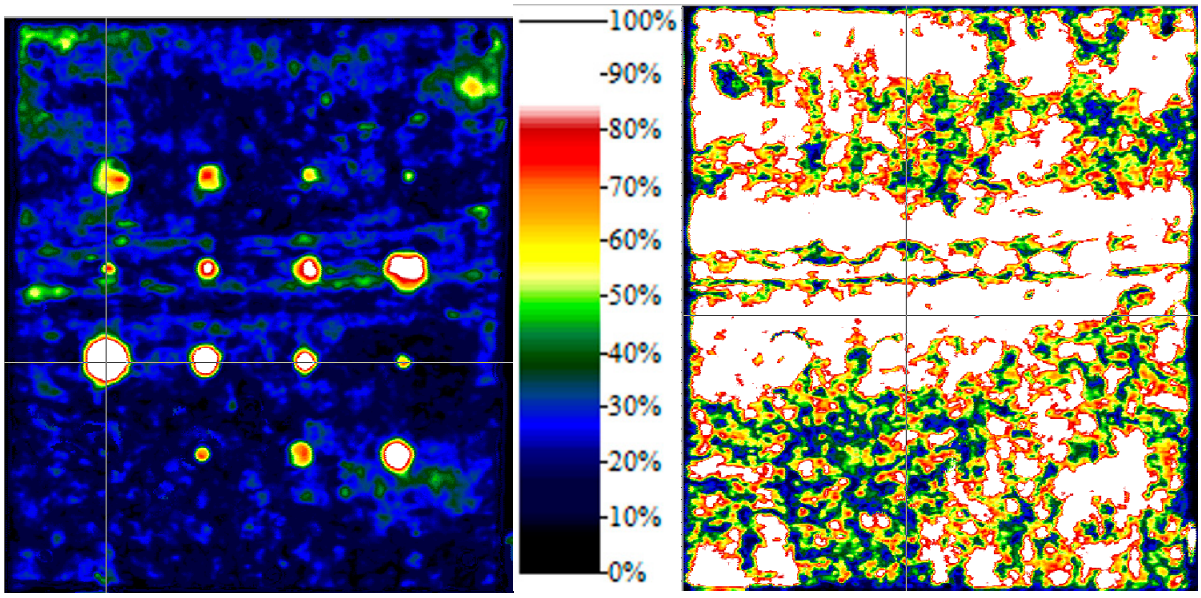

Figure 6-10: Reflection C-scans of IRP1 with DAC/TCG, 500 kHz and 1 MHz, gate between FR and BR

The TOF C-scans for both 500 kHz and 1 MHz with DAC/TCG can be seen in Figure 6-11. As in line with the reflection C-scan of Figure 6-10 the magnitude and the amount of reflection signals received from the basis material are significantly reduced for the 500 kHz transducer compared to the inspection without DAC/TCG (Figure 6-5). The 1 MHz inspection still suffers from large reflection signal from the base material.

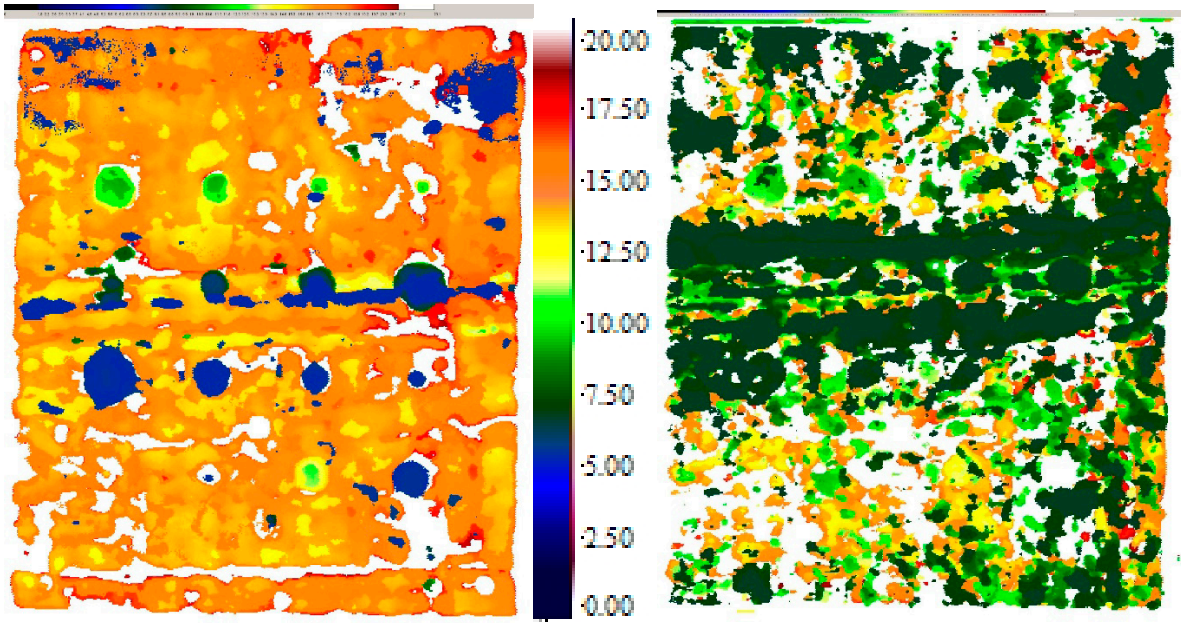

Figure 6-11: Time Of Flight C-scan of IRP1, 500kHz and 1 MHz with DAC/TCG, gate just after FR and including BR

Based on both experiments with 500 kHz and 1 MHz transducer frequency, without DAC/TCG and with DAC/TCG, it can be concluded that the 500kHz with DAC/TCG is the optimum transducer frequency and method to inspect the coarse grained high attenuative GFRP material.

When observing more in detail the responses of the FBH's, the following can be observed in TOF C-scan of Figure 6-12:

- At the first row all diameter FBH's (0.5, 0.75, 1 and 1.5 inch) at a depth of approx. 9.8 mm are detected;
- The same applies for the second row, all FBH's at a depth of approx. 7.2.mm are detected;
- The FBH's of the third row are positioned at a depth of approx. 2.9 mm. In the TOF C-scan, the FBH's are presented in blue which indicate a depth of approximately 5 to 6 mm. This implies that the multiple echo of the FBH's are detected (bulky signal).
- The near- and far surface FBH's with a diameter of 1 inch are detected, the 1 inch FBH at a depth of 0.7 mm is detected with a multiple echo (bulky signal), the time of flight the indicates a depth of approx. 5 mm. The 1 inch FBH at a depth of 11.5 mm is presented correctly in the TOF C-scan. The near- and far surface FBH's with a diameter of 0.5 inch are considered not detectable.

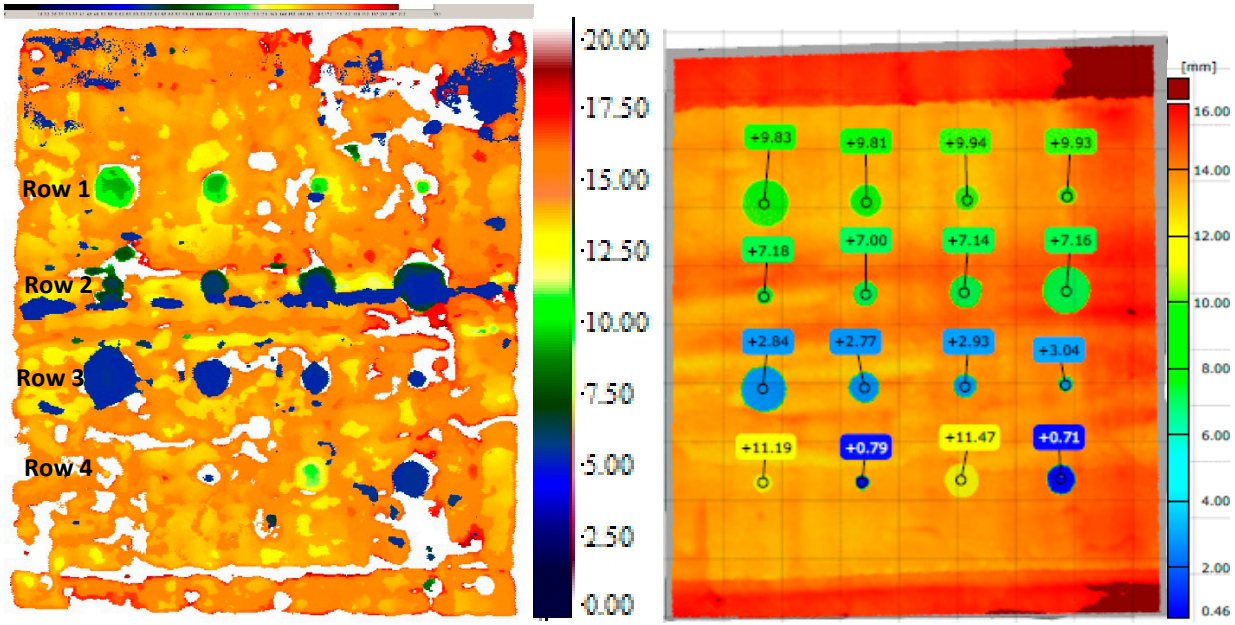

Figure 6-12: Time Of Flight C-scan of IRP1, 500kHz, gate just after FR and including BR (left hand side) and actual remaining material from the 3D optical measurement (right hand side)

For the remaining IRP4, IRP10, IRP13 and IRP27 only the 500kHz with DAC/TCG applications are included in this report.

6.2 IRP4 Relative flat monolithic skin stepwedge

The function of the stepwedge was intended to determine the general attenuation of the GFRP material in dB/mm. Due to the large quality differences, this is not possible, see also the C-scan test results of Figure 6-13. Due to the different thicknesses it is not possible to define one gate setting to collect all reflections signals in a reflection C-scan. At the thin section of approx. 3.5 mm it is not possible to distinguish the first backwall reflection, at the TOF C-scan it can be seen that most probably the repeat echo is collected.

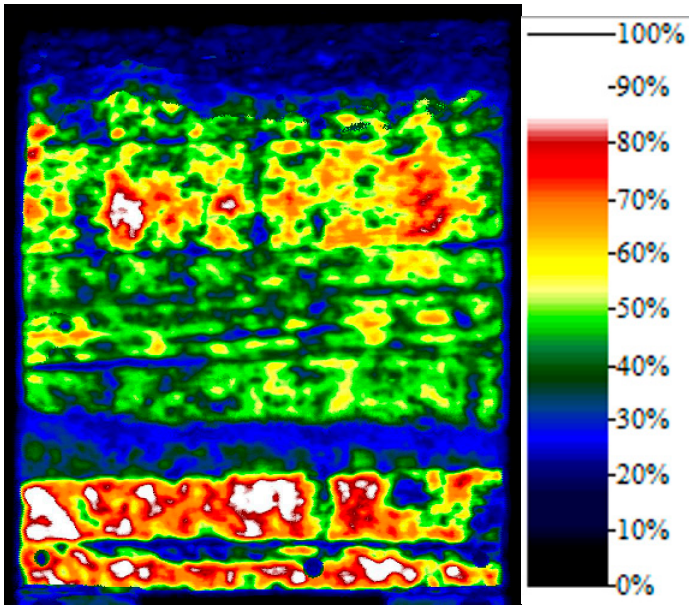

Attenuation C-scans, with DAC/TCG, 500kHz, gate on BR

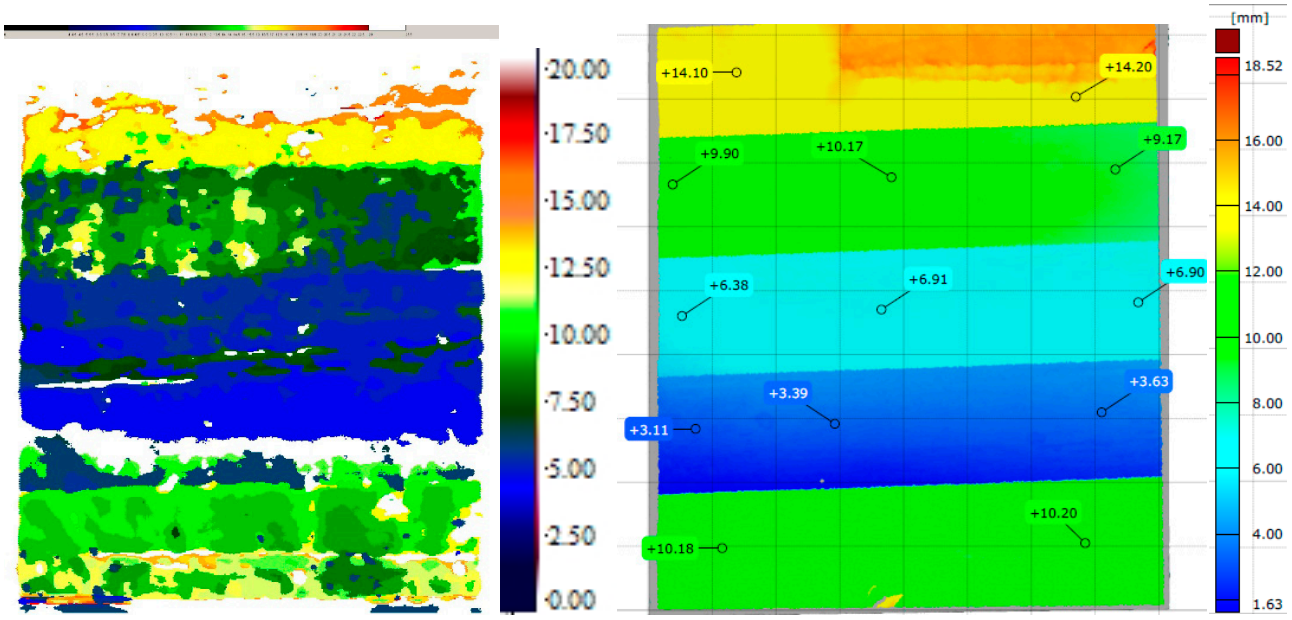

Time Of Flight C-scan, 500kHz, with DAC/TCG, gate just after FR and including BR

3D measurement, Actual remaining material

Figure 6-13: C-scan and 3D measurements test results of IRP4

6.3 IRP10 Relative flat sandwich skin

IRP10 represents the sandwich areas of the wind turbine rotor which is more located at the aft side of the blade towards the trailing edge. The sandwich material consist of balsa wood as indicated in Figure 6-14. The inserted FBH's are positioned at both interfaces between the sandwich material and the GFRP skin. The inspections are performed from the outer side of the skin. Due to high porosity content of the balsa wood it is not possible to penetrate this material with ultrasound. Beforehand is can be concluded that the FBH's positioned at row 2 (the inner side of the balsa wood) cannot be detected with the ultrasonic method.

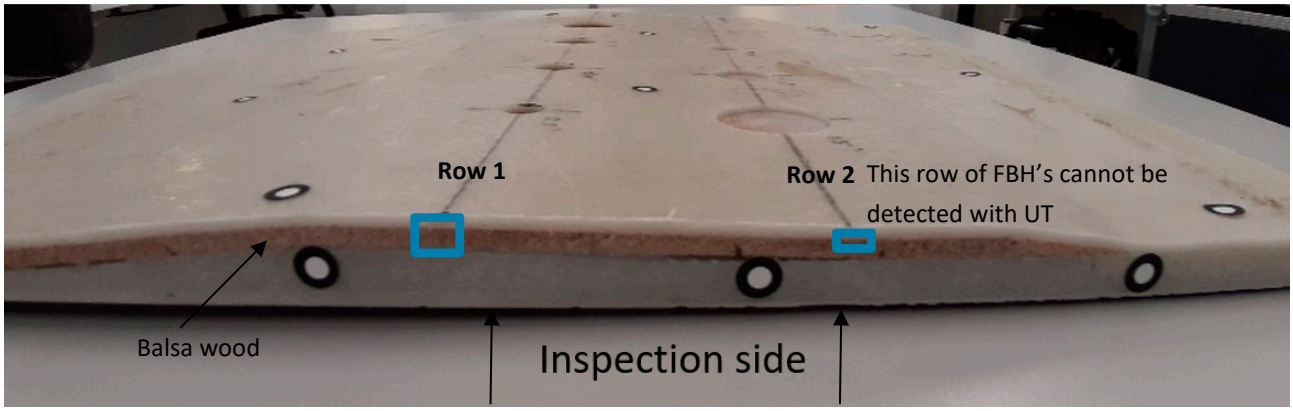

Figure 6-14: Side view of IRP10 showing the position of the balsa wood, inspection side and depth positions of the FBH's

Figure 6-15 shows the attenuation, reflection and TOF of IRP10. As expected the FBH's of IRP10 cannot be detected with the ultrasonic method. The FBH's of row 1 simulate, in fact, a debonding between the GFRP skin material and the core balsa wood. The high porosity content of the balsa wood already gives a 100 % reflection of the ultrasound beam. Therefore, no extra reflection can be expected from the FBH located at the glass/balsa wood interface.

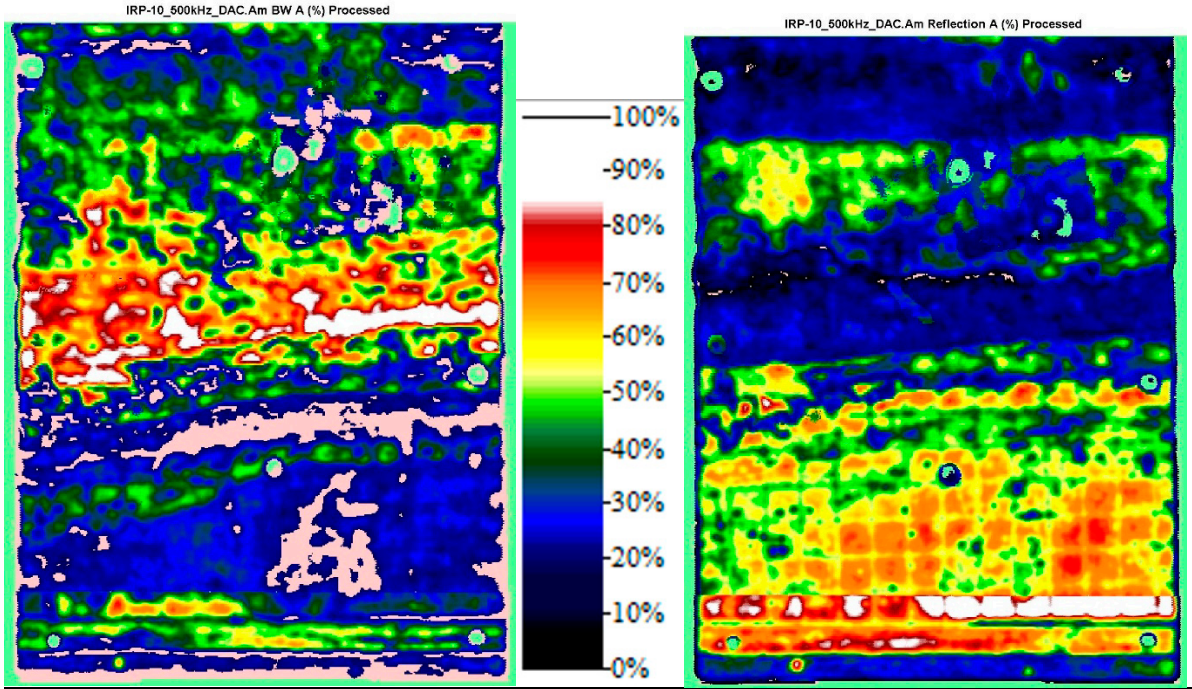

Attenuation C-scan, with DAC/TCG, 500kHz, gate on 1st interface balsa wood	*Reflection C-scan, with DAC/TCG, 500 kHz, gate between FR and 1st interface balsa wood*

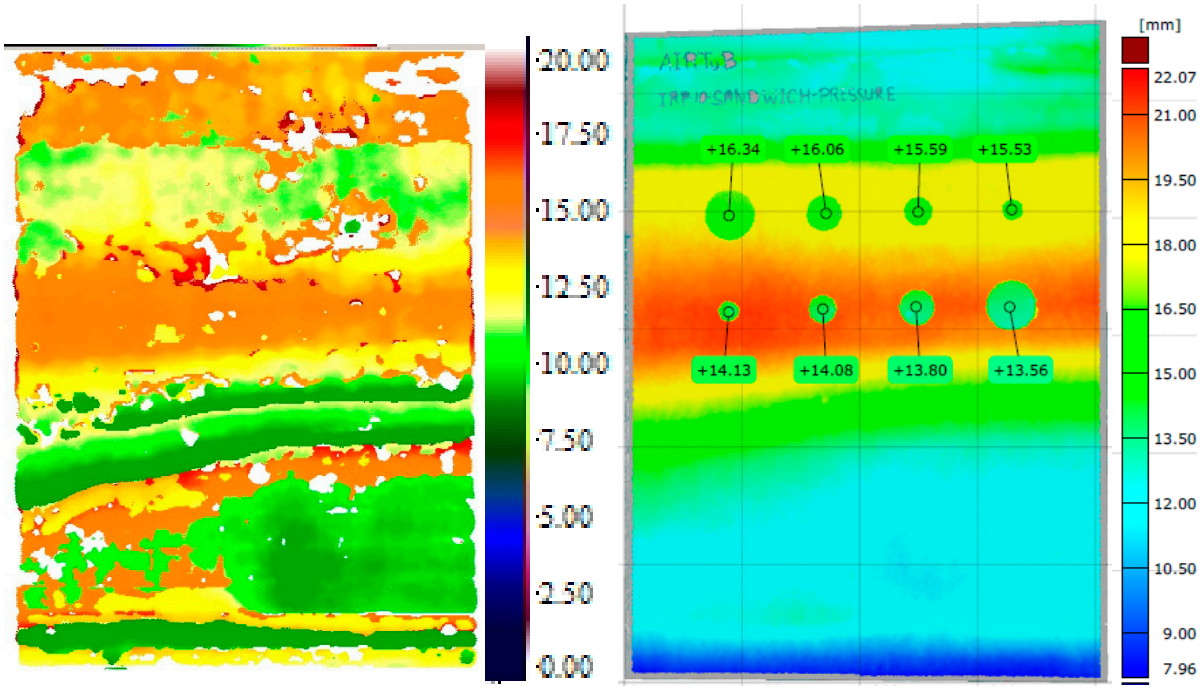

TOF *3D measurement, Actual remaining material*

Figure 6-15: C-scan and 3D measurements test results of IRP10

6.4 IRP13 Curved monolithic skin part

Figure 6-16 shows the attenuation, reflection and TOF C-scans of IRP13. The following observations are made:

- Attenuation C-scan:
  Monitoring the amplitude of the BR, a significant attenuation is expected resulting in an amplitude drop of the BR. Due to these high attenuative material, large amplitude variations of the BR can be seen. Therefore, it is quite hard to identify the FBH's. When evaluating the data more in detail, the following is observed:
  - Row 1 and 2, at respectively depths of approx. 11.6 mm and 7.6 mm, the FBH's show an increase of amplitude (white) instead of an amplitude reduction. The reflection signals of the FBH's (or repeat echo's) are collected in the backwall gate. In fact, the reflection of the FBH's and the reflection of the backwall cannot be separated from the A-scan trace.
  - Row 3 is can be detected as expected. The FBH's at a depth of approx. 3.7 mm shows a significant amplitude reduction (blue) of the backwall.
  - The same applies for row 4 (near-and far surface FBH's). The FBH's just beneath the front surface shows a amplitude reduction and the FBH's close to the backwall shows an amplitude increase (large reflection of the FBH's falls in backwall gate).
- Reflection C-scan:
  The reflection C-scan shows clear indications of all FBH's with exception of 0.5 inch diameter FBH close to the front reflection (row 4), at a depth of 2.2 mm, which is qualified as detectable with limitation.
- TOF C-scan:
  The TOF C-scan shows again that all FBH's are detectable, however, when evaluating the data more in detail the following is observed:
  - Row 1 with the FBH's at a depth of approx. 11.5 mm are-more-or less presented correctly in the TOF C-scan.

- This also applies for row 2.
- At row 3 the FBH's are presented in the TOF data at approx. 15 mm, in fact, the FBH's are positioned at approx. 3.7 mm. This can be explained, a multiple echo (bulky signal) of the FBH's are collected with the TOF gate.
- At row 4 also the near surface FBH's are not correctly presented in the TOF C-scan.

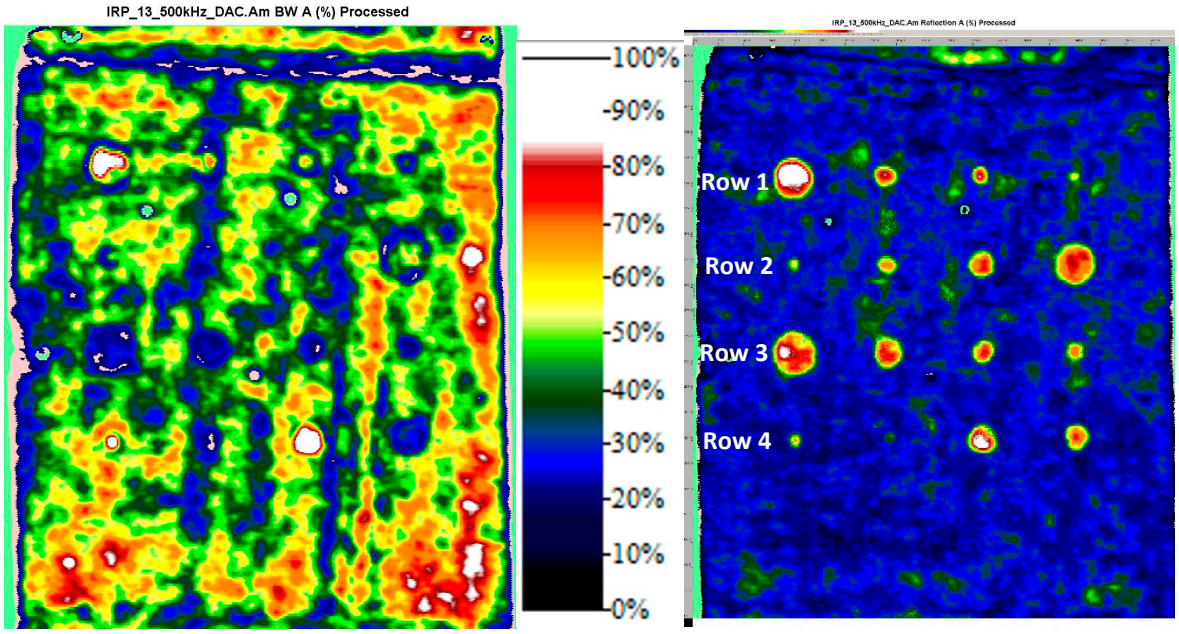

Attenuation (gate on BR) *Reflection (gate between FR and BR)*

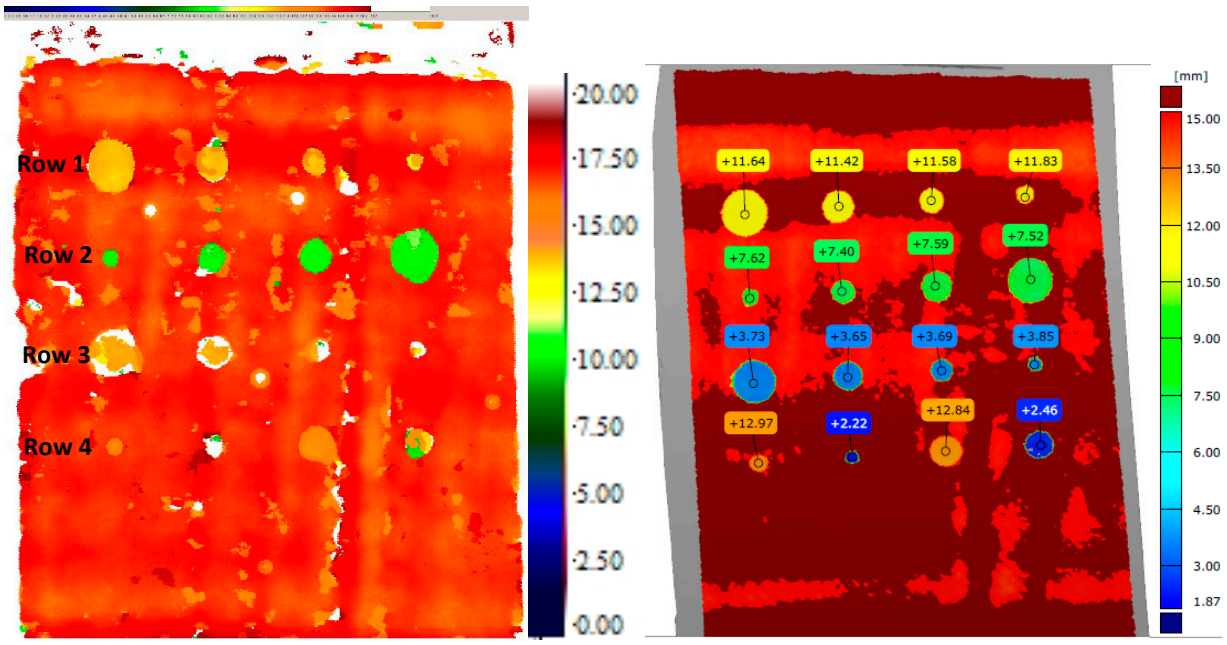

TOF *3D measurement, Actual remaining material*

Figure 6-16: TOF C-scan and 3D measurements test results of IRP13

6.5 IRP27 Skin/spar bonded connection

A skin/spar bonded connection is probably one of the more critical structural detail of a wind blade rotor. In total 3 diameter FBH's are inserted in IRP27, 0.5 inch (12.7mm), 0.75 inch (19.1 mm) and 1 inch (25.4 mm) respectively on two depth positions as indicated in Figure 6-17 Detailed view of IRP27 showing the skin/spar bonding connection and the depth positions of the FBH's. The two depth position simulate a disbonding between the GFRP skin and the adhesive layer and a disbond between the adhesive layer and the GFRP spar. Due to the relative thick adhesive layer both interfaces are chosen as possible critical interfaces.

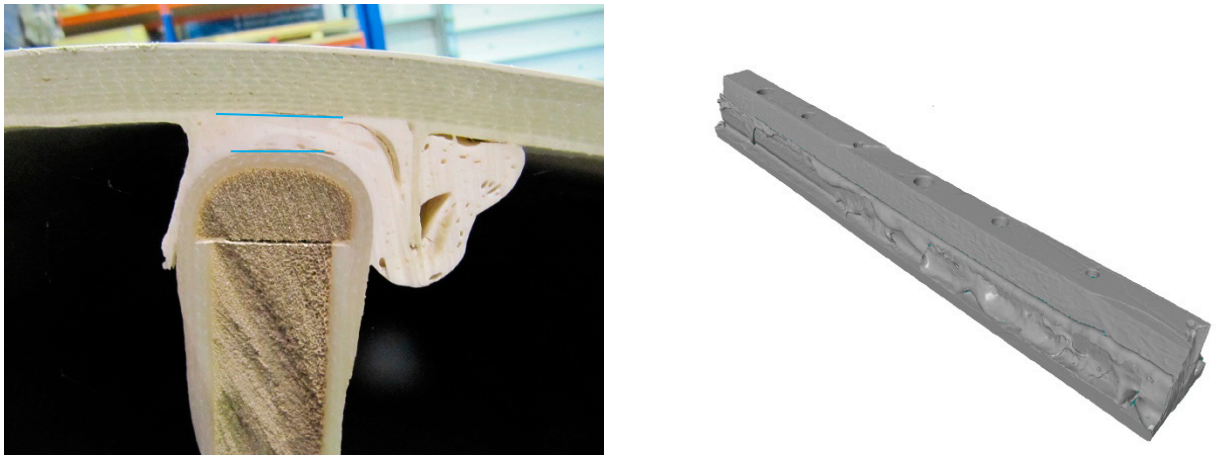

Figure 6-17: Detailed view of IRP27 showing the skin/spar bonding connection and the depth positions of the FBH's

Due to the fact that the defects are located at the interface of the skin and the adhesive layer, only the backwall echo is relevant to monitor. Figure 6-18 shows the attenuation C-scan, the white arrows are indicating the three FBH with a the circular appearance. The higher reflection of the backwall echo(white/red circle) is caused due to the fact that the ultrasound cannot be transmitted into the adhesive layer and back-up structure (locally removed by machining). In this case the FBH's are detected due to the fact that the circle shape is known. When observing the complete C-scan, including all amplitude differences it must be concluded that the debonding can be detected doubtfully. Larger defect sizes are most probably detectable but not included in this reference panel to underpin this statement with experimental results. The FBH's located at the interface adhesive/stiffener are not detected.

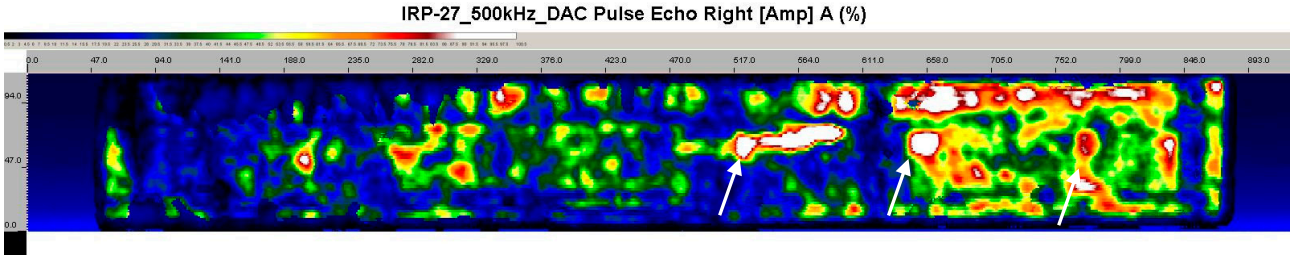

Figure 6-18: Attenuation C-scan test results of IRP27

Concluding remarks, with respect to the baseline UT test results, are mentioned in chapter 9 Conclusions.

7 CIVA simulation and PAUT set-up

This section provides simulation on IRP13 and the comparison with the experimental PAUT measurements are made.

7.1 CIVA modelling

Based on the test results of the baseline measurements with conventional ultrasonic C-scan, the PAUT CIVA modelling will be performed using a 500 kHz probe. For the simulation, the basic characteristics of the transducer are used: central frequency 500 kHz, bandwidth 53%, 64 elements with a pitch of 2 mm, spacing of 0.5 mm and elevation of 10 mm (transducer width).

The material can be defined as isotropic or anisotropic (cubic, transversely isotropic, orthotropic, monoclinic, and triclinic). Material types can be selected from a database where after the density and longitudinal/transverse wave velocities are given automatically. Figure 7-1 shows the parameters of the GFRP, selected from the CIVA library.

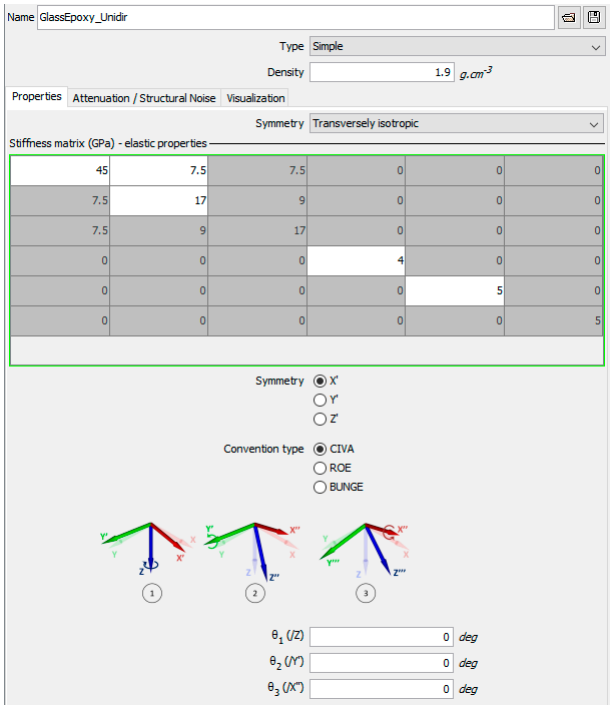

Figure 7-1: Selected GFRP material properties in CIVA

For the PAUT inspections, an important parameter is the size of the active aperture (number of active elements). This parameter has a significant influence on the shape of the ultrasonic beam in the GFRP material.
To have a first impression of the beam profiles using different aperture sizes (4, 8 and 16 elements), the following beam computations are performed using CIVA software. Basic parameters applied are; frequency of 500 kHz, infinite focus and a 15 mm thick GFRP. The direction of the ultrasound beam is normal to the entry surface (0°), so only generating longitudinal/compression sound waves. Figure 7-2 shows an overview of the beam profiles simulated with aperture sizes of 4, 8 and 16 elements.

- Although with 4 elements an well-defined beam is generated with almost a symmetric profile, the generated sound energy is somewhat less compared to larger aperture sizes. The light blue area presents the higher sound energy content of the sound beam, covering approximately the halve thickness of the GFRP plate.
- Also when using 8 elements a well-defined beam profile is generated. But comparing the active and passive direction of the PA-transducer in more detail, a slightly asymmetric sound beam can be witnessed. This is also observed in the top view, the cross-section has a more elliptical shape compared to the circle cross-section appearance when using 4 elements. The energy output is sufficient for the GFRP plate of 15 mm (without voids).
- With 16 elements more energy output is generated, as expected when using more elements, but with a more asymmetric beam profile. At the top it can be witnessed that almost two sound beams are generated with both their own maximum sound pressure. This amount of sound energy could be beneficial when inspecting thicker GFRP specimens but for this 15 mm GFRP plate less suitable.

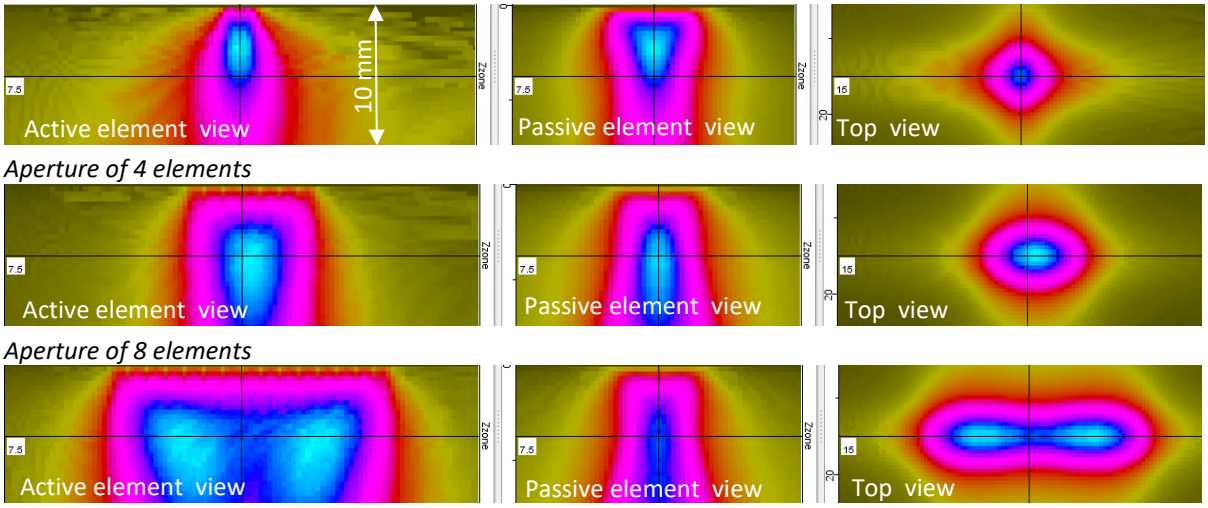

Aperture of 4 elements

Aperture of 8 elements

Aperture of 16 elements

Figure 7-2: Beam profiles of a 500 kHz PA-transducer in a 15 mm thick GFRP plate at different apertures

To determine the influence of the different beam profiles the layout of IRP13 is imported in CIVA. The GFRP material is assumed isotropic, unidirectional, homogenized and with no voids. To evaluate defect responses of FBH's using the different aperture sizes one row of IRP13 is selected, see Figure 7-3.

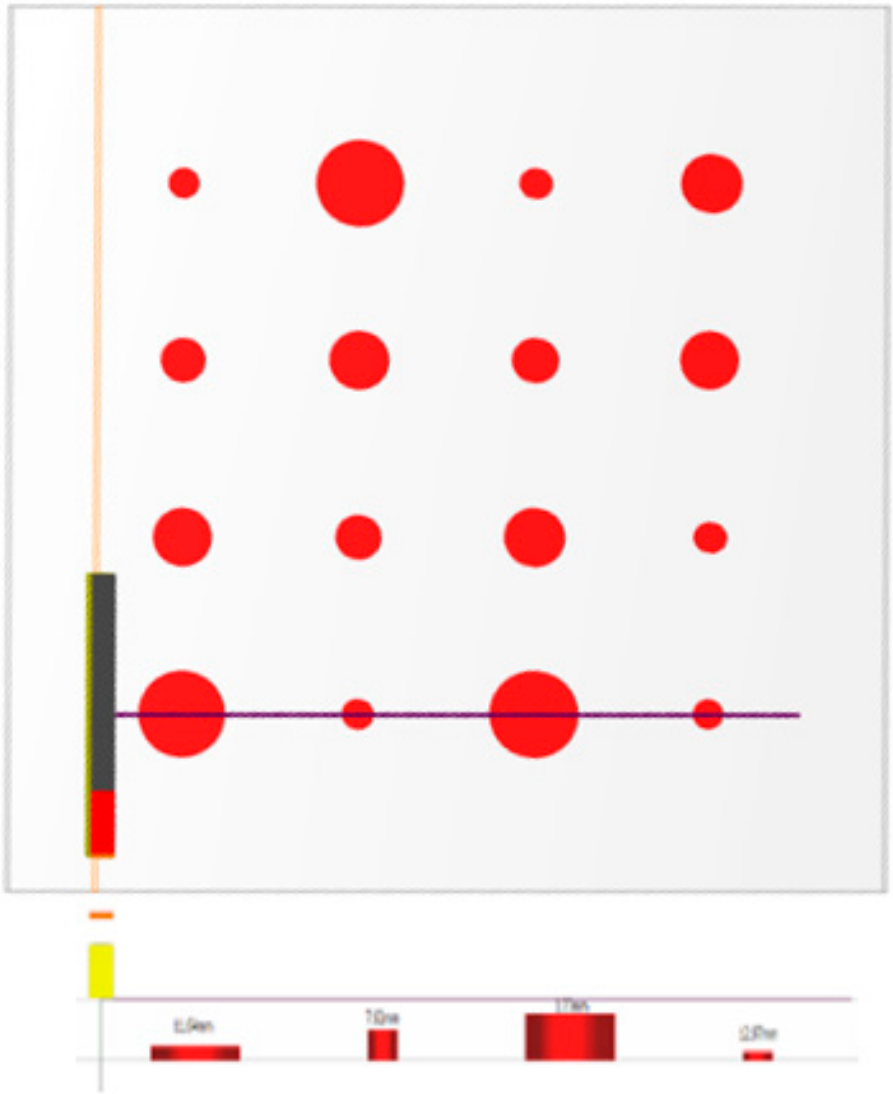

Figure 7-3: Showing layout of IRP13 modulated in CIVA, PA-transducer and selected FBH row

The simulations show that with larger aperture there is more signal strength but that the shape of the defect is distorted (more elliptical), see Figure 7-4. Both the signal strength and shape distortion can be explained when observing the calculated beam profiles of Figure 7-2. So one can conclude that a smaller aperture with added gain would provide an improved C-scan result. The baseline ultrasonic test results shows that the material is highly attenuative and not of constant quality. These material conditions are not included in this simulation. Therefore, it is doubtful whether this conclusion is completely valid in practice. Although the aperture of 4 elements shows a better defect response w.r.t. shape, in practice it must be determined if enough energy is generated with this aperture size.

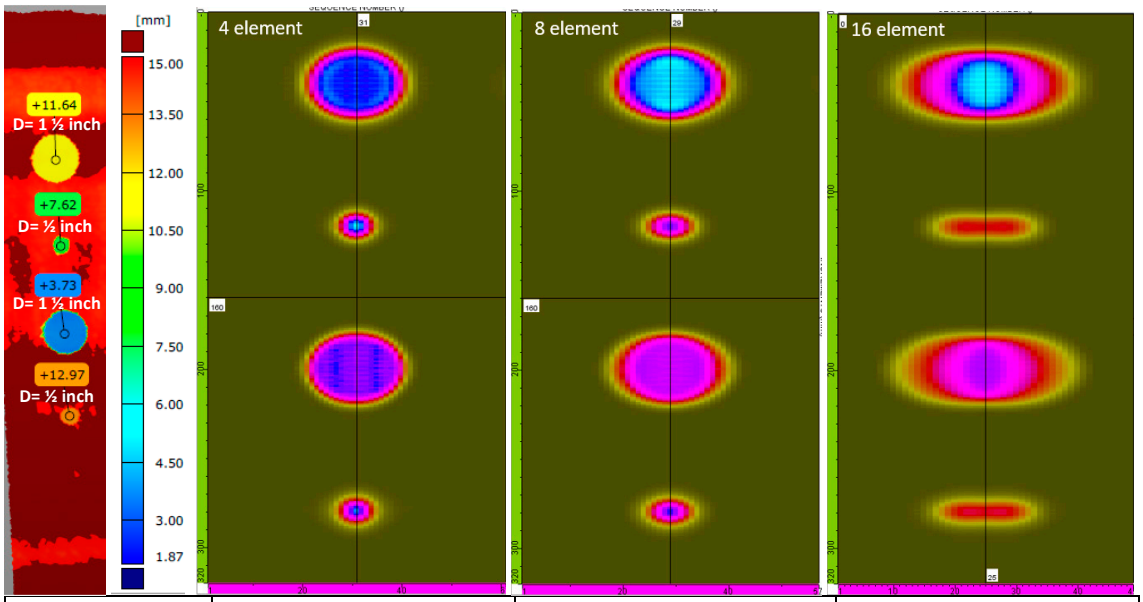

Remaining material	4 elements/aperture	8 elements/aperture	16 elements/aperture

Figure 7-4: Modulating test result: influence of aperture size on detectability FBH's of one row of IRP13

The best compromise is probably using 8 elements for inspecting a 15 mm GFRP plate. But when inspecting larger thickness, for example 30 or 60 mm GFRP plates, a larger aperture could be beneficial. Figure 7-5 shows an overview of the beam profiles in a 30 mm GFRP plate. More or less the same beam profiles are generated as with the 15 mm thick GFRP. Due to the 30 mm thick GFRP more, of the beam profile is presented. This lack of "penetration" depth must be compensated with the application of a DAC/TCG.

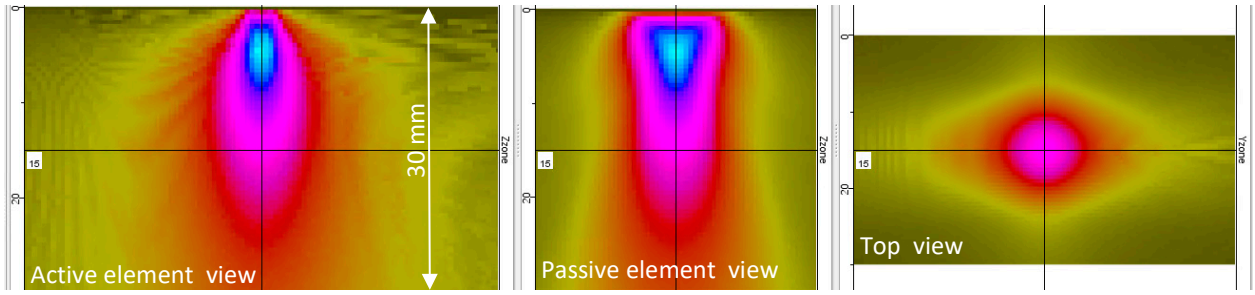

Aperture of 4 elements

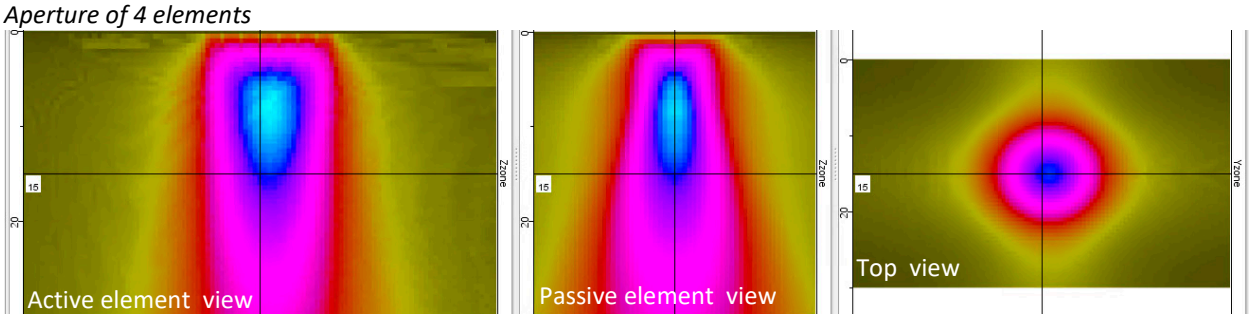

Aperture of 8 elements

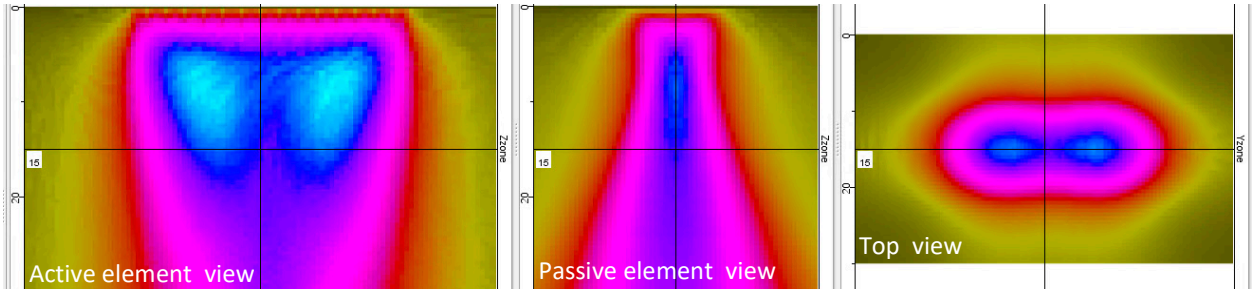

Aperture of 16 elements

Figure 7-5: Beam profiles of a 500 kHz PA-transducer in a 30 mm thick GFRP plate at different apertures

Figure 7-6 shows an overview of the beam profiles in a 60 mm GFRP plate. Comparable to the beam profiles at a 30 mm GFRP plate, all beam profiles shows a lack of sound energy. Also abeam profile using an aperture of 32 elements is simulated. In this case the 16 and 32 elements aperture seems to be the best choice. For the 60 mm GFRP plate it is doubtful whether the application of DAC/TCG will compensate sufficiently, especially when the GFRP material is highly attenuative due to fibre undulations, small cracks and high porosity content.

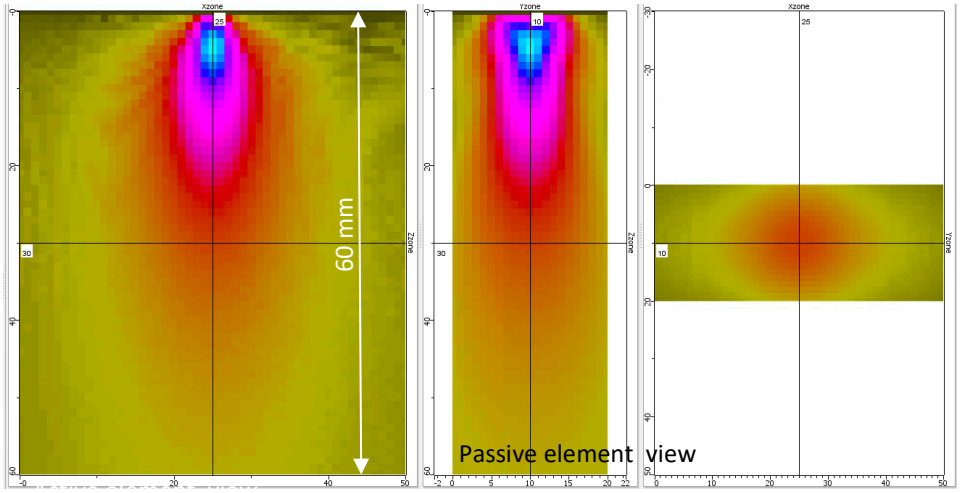

Aperture of 4 elements

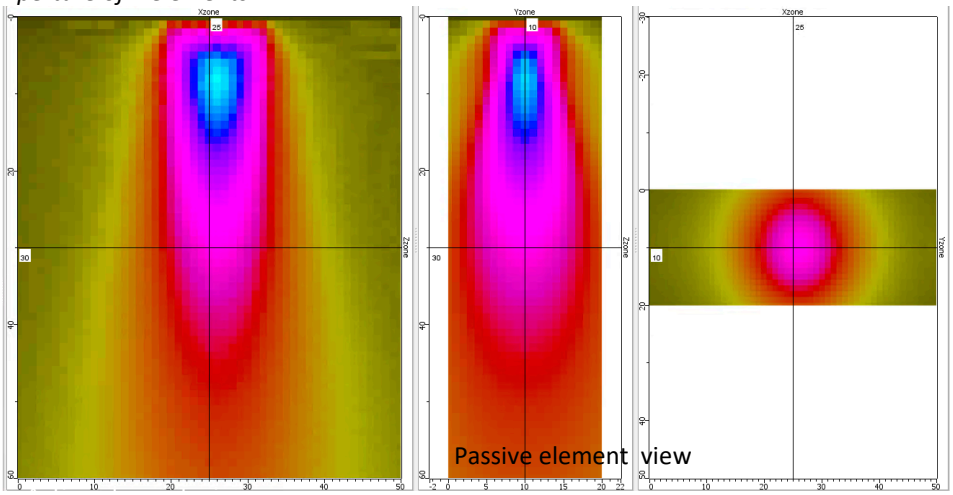

Aperture of 8 elements

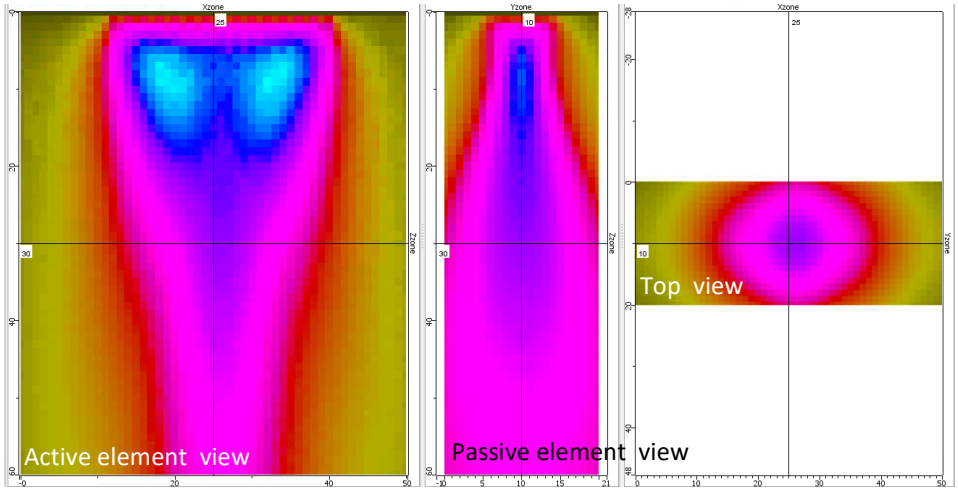

Aperture of 16 elements

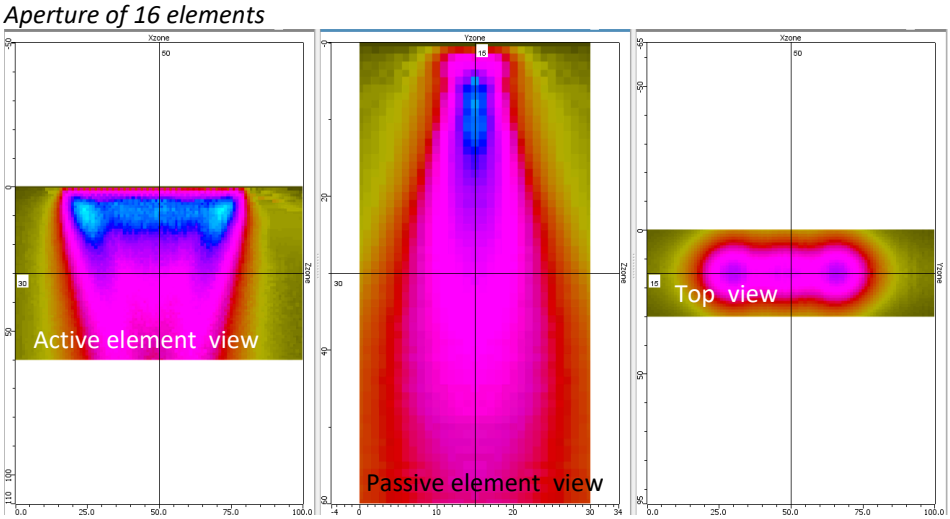

Aperture of 32 elements

Figure 7-6: Beam profiles of a 500 kHz PA-transducer in a 60 mm thick GFRP plate at different apertures

7.2 Setup DAC/TCG with PA-transducer

The CIVA simulations were performed without DAC/TCG, but for the experimental tests we have to take into account the highly attenuative GFRP w.r.t. fibre undulations, small cracks and high porosity content. Therefore, a TCG is mandatory to achieve a workable signal-to-noise ratio. During conventional ultrasonic C-scan, the DAC/TCG was determined on the 1.5 inch FBH's of IRP1. The FBH's are located at the following depths: 2.8, 7.2 and 9.8 mm. The same FBH's are used to setup the DAC/TCG for the PA-transducer. However, for the PA-transducer the total active width of the transducer (including all defined apertures) must be physically above the applicable FBH's. This means that the PA-transducer must make a sliding movement over the FBH's and should be ideally only measuring the reflection signal of the FBH, see Figure 7-7.

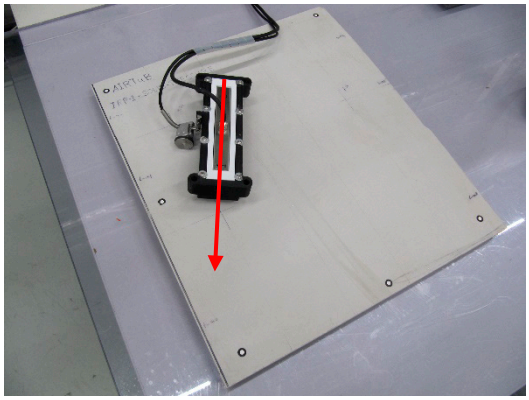

Figure 7-7: Sliding movement PA-transducer over 1.5 inch diameter FBH's of IRP1 to determine the DAC/TCG

After the sensitivity measurements are performed on a Perspex plate, as described in chapter 5.2, the DAC/TCG setup can be performed. The PA-transducer is positioned just before the 1.5 inch FBH at a depth of 2.8 mm and a sliding movement as indicated in Figure 7-7 is performed. The signal response of all apertures of the 1.5 inch diameter FBH at a depth of 2.8 mm is adjusted to 80% FSH. This calibrating procedure is repeated for the 1.5 ich FBH's at the depths of respectively 7.2 mm and 9.8 mm.

Figure 7-8 shows the A-scan presentation at sound material, clear reflection can be seen from the backwall. Furthermore, the 3 DAC/TCG points are indicated.

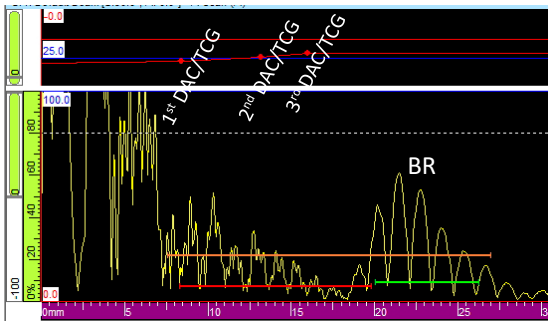

Figure 7-8: Example of an A-scan trace with the 3 DAC/TCG points

With the DAC/TCG settings derived from the 1.5 inch FBH's of IRP1, the PAUT inspections are performed on the reference specimens IRP1, IRP4, IRP10, IRP13 and IRP27. The basic PAUT settings including gain/TCG are given in Appendix B.

7.3 Determination of the aperture size

Figure 7-9 shows the experimental C-scan reflection test results on IRP13 of row 1 using different aperture sizes, respectively 4, 8 and 16 elements. In general, larger aperture sizes will generate more sound energy. However, the DAC/TCG compensates for a part these generated energy differences. When having a closer look to the differences between 4 and 8 elements, it can be seen that the an aperture with 8 elements gives a somewhat clearer reflection C-scan. At the reflection C-scan, generated with an aperture existing of 16 elements, it can be observed that especially the smaller 0.5 inch FBH at a depth of 7.6 mm is completely distorted in an ellipse shape. This test results corresponds with the CIVA sound beam modulation, see also Figure 7-4. Further, the 0.5 inch FBH at a depth of 13 mm is not detected at all and the larger 1.5 inch diameter FBH's are also somewhat distorted.

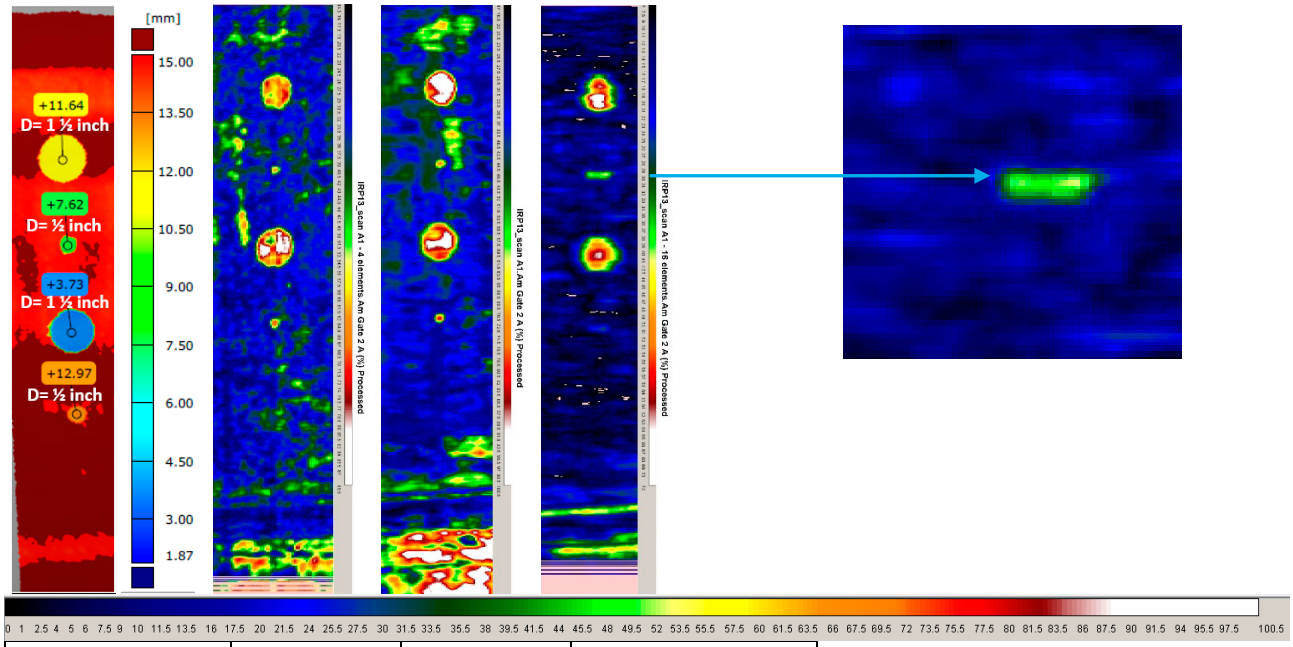

Remaining material	4 elements/ aperture	8 elements/ aperture	16 elements/ aperture

Figure 7-9: Experimental reflection C-scan showing the influence of aperture size on the detectability of the FBH's (row 1 of IRP13). The reflection signals between the FR and BR are collected

Figure 7-10 shows the attenuation C-scan of the of IRP13 of row 1 monitoring the backwall amplitude. The reflections signals from the FBH's, both 0.5 inch and 1.5 inch, at a depth of 12 mm falls in the backwall gate. This results in not a complete detection of the 0.5 inch FBH's, but only the edges of the 1.5 inch FBH's. The distortion of the smaller 0.5 inch FBH at a depth of 7.6 mm is less distorted compared to the reflection scan. Possible explanation could be that the sound beam is more uniform at a depth of 30 mm compared to the 7.6 mm depth registration of the reflection C-scan.

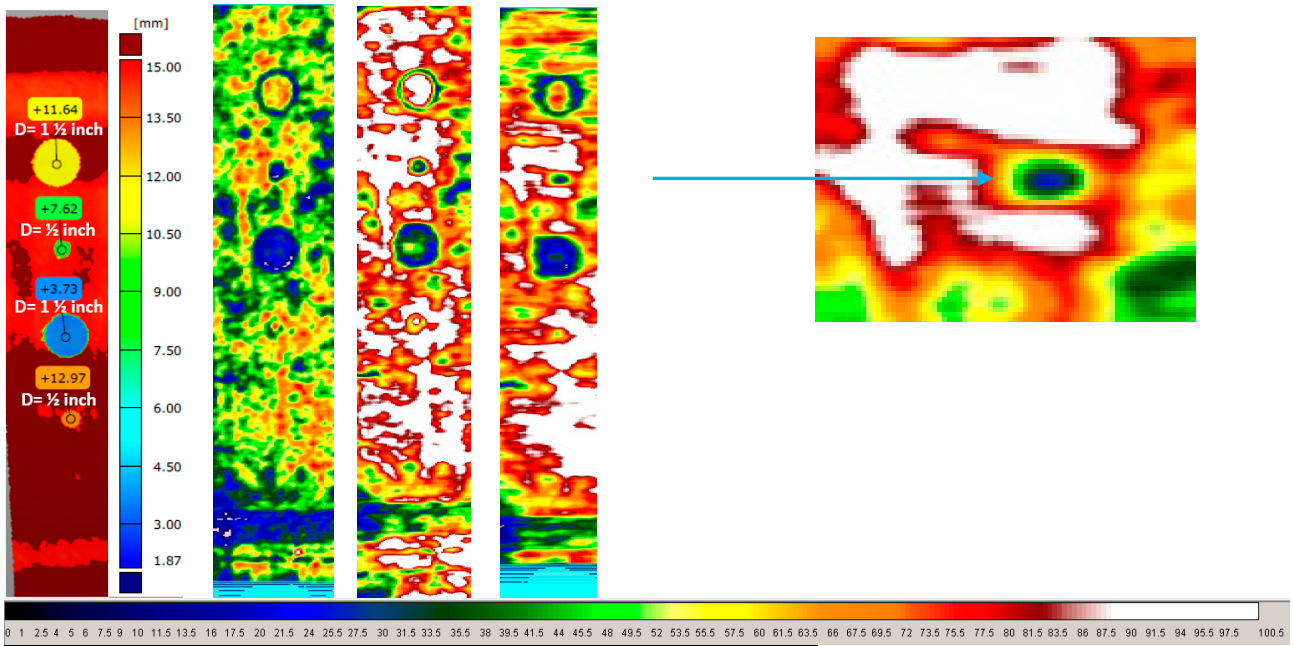

Remaining material	4 elements/ aperture Gain	8 elements/ aperture Gain	16 elements/ aperture Gain

Figure 7-10: Experimental attenuation C-scan showing the Influence of aperture size on the detectability of the FBH's (row 1 of IRP13). The backwall signal is collected

Figure 7-11 shows the TOF C-scan of the of IRP13 monitoring the time differences between the reflection signals and indicating the depth positions of the FBH's. Also here, the 0.5 inch FBH's close to the backwall are not detected. The 0.5 inch FBH at a depth of 7.6 mm shows, more-or-less, the same distortion as observed at the reflection C-scan. This distortion is explainable because it is the same UT-signal: for the reflection C-scan the amplitude of the signal is plotted and for the TOF the duration of the reflection signal measured in [µs] or [mm] is plotted.

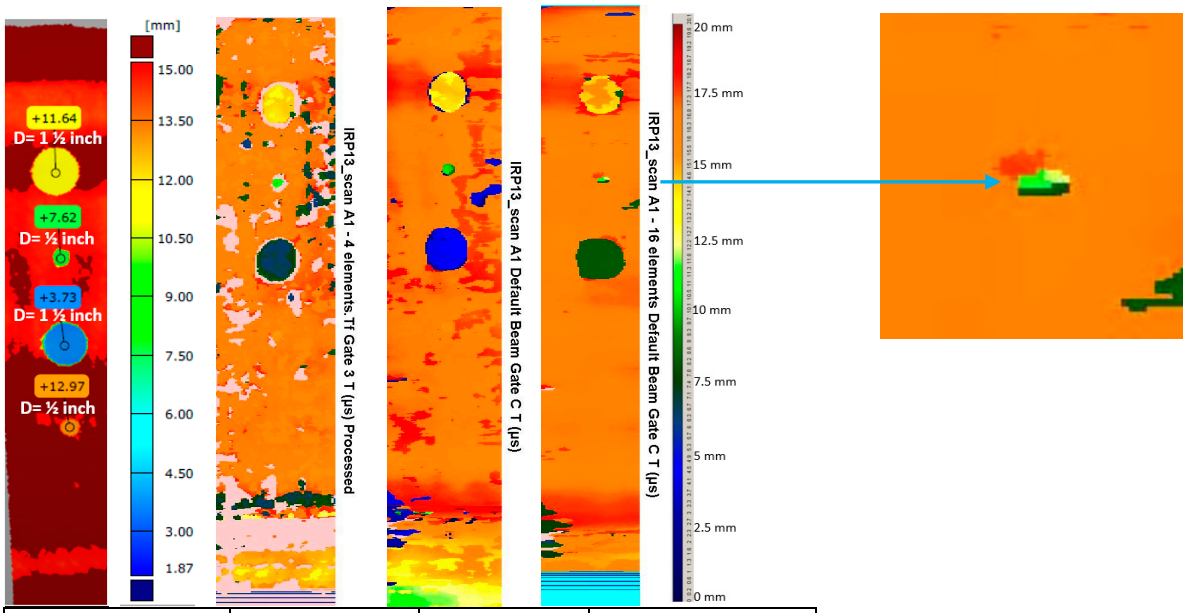

Remaining material	4 elements/ aperture	8 elements/ aperture	16 elements/ aperture

Figure 7-11: Experimental TOF C-scan showing the Influence of aperture size on the detectability of the FBH's (row 1 of IRP13). The reflection signals after the FR are collected measuring the time/position)

7.4 Final PAUT set-up

A pulse-echo method, using a contact coupling, is performed on all reference panels. Due to the new PAUT sliding probe, only a thin spray of water is sufficient to establish the ultrasonic coupling. The DAC/TCG settings as determined in chapter 7.2 are applied. The number of elements per aperture is set to 8, as determined in chapter 7.3 One gate of the PA-ultrasonic unit is placed over the backwall reflection signal to collect an attenuation C-scan and a second gate between the front reflection and the backwall reflection to collect a reflection C-scan. The backwall signal for "sound material" is set at 80% full screen height (FSH) of the ultrasonic unit. Sound material can be defined as the best area of the IRP panel, in other words, the area with the lowest attenuation. The basic PAUT settings are given in Appendix B.

8 PAUT IRP test results

This chapter elaborates on the PAUT results that are acquired on the IRP from Chapter 2 using the new PAUT sliding probe design introduced in Chapter 5. The handheld probe is used without the AIRTuB crawler. Sections 8.1 to 8.5 presents the baseline C-scan results on each IRP.

8.1 IRP1 Relative flat monolithic skin part

Figure 8-1 shows both the attenuation and reflection C-scans of IRP1. When observing the C-scans more in detail the following can be observed:

Note: Figure 8-3 shows the measured depth positions (remaining material) of the FBH's in IRP1.

- At the first row only the contour of the FBH's (diameters of 0.5, 0.75, 1 and 1.5 inch) at a depth of approx. 9.8 mm can be seen in the PAUT attenuation C-scan. In the reflection C-scan all FBH's of row 1 are clearly detected;
- The same applies for the second row, all FBH's at a depth of approx. 7.2.mm are detected for both the PAUT attenuation and reflection C-scan. Exception is the 0.5 inch FBH at the attenuation C-scan, due to a local quality reduction the attenuation of the basis material mask the FBH and therefore not detectable;
- The FBH's of the third row are positioned at a depth of approx. 2.9 mm. All FBH's in both the PAUT attenuation and PAUT reflection C-scan are detectable;
- The near- and far surface FBH's at row 4 with a diameter of 1 inch are detected in the PAUT attenuation C-scan with a limited detectability for the 1 inch diameter FBH at a depth of 11.5mm. At the PAUT reflection C-scan only the one inch diameter FBH's at depths of 0.7 mm and 11.5 mm are detectable. The near- and far surface FBH's with a diameter of 0.5 inch are considered not detectable.

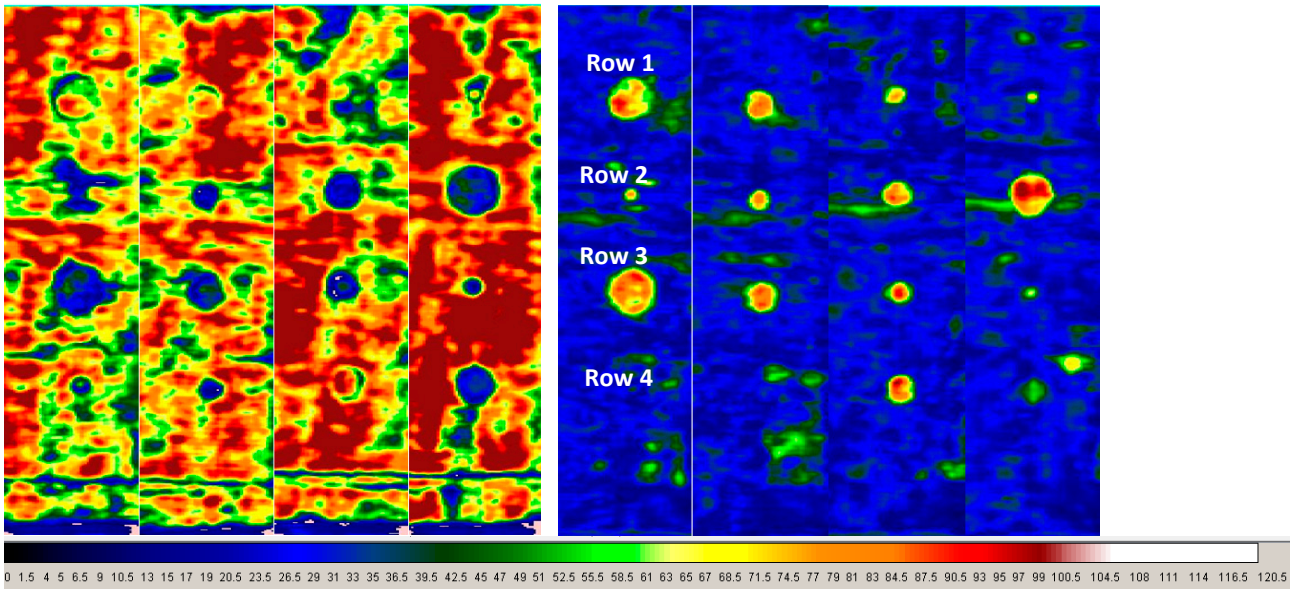

PAUT Attenuation C-scans, gate on BR *PAUT reflection C-scan, gate between FR and BR*

Figure 8-1: PAUT attenuation and reflection C-scans of IRP1, 500kHz

When comparing the PAUT test results of Figure 8-1 with the conventional amplitude C-scans of Figure 8-2 more-or-less the same test results can be observed. To generate the PAUT data, four individual scan strokes are performed at the center of the FBH rows, observe also the vertical stripes. These individual scans are not merged with an overlap but presented just next to each other. Therefore, the C-scans cannot be compared directly 1:1 to the conventional UT C-scans but only w.r.t. the detectability of the FBH's. Further, the PAUT attenuation C-scan at the "sound areas" is somewhat in saturation (dark red areas). Because of that, the range of the color bar is set from 1 to 120%.

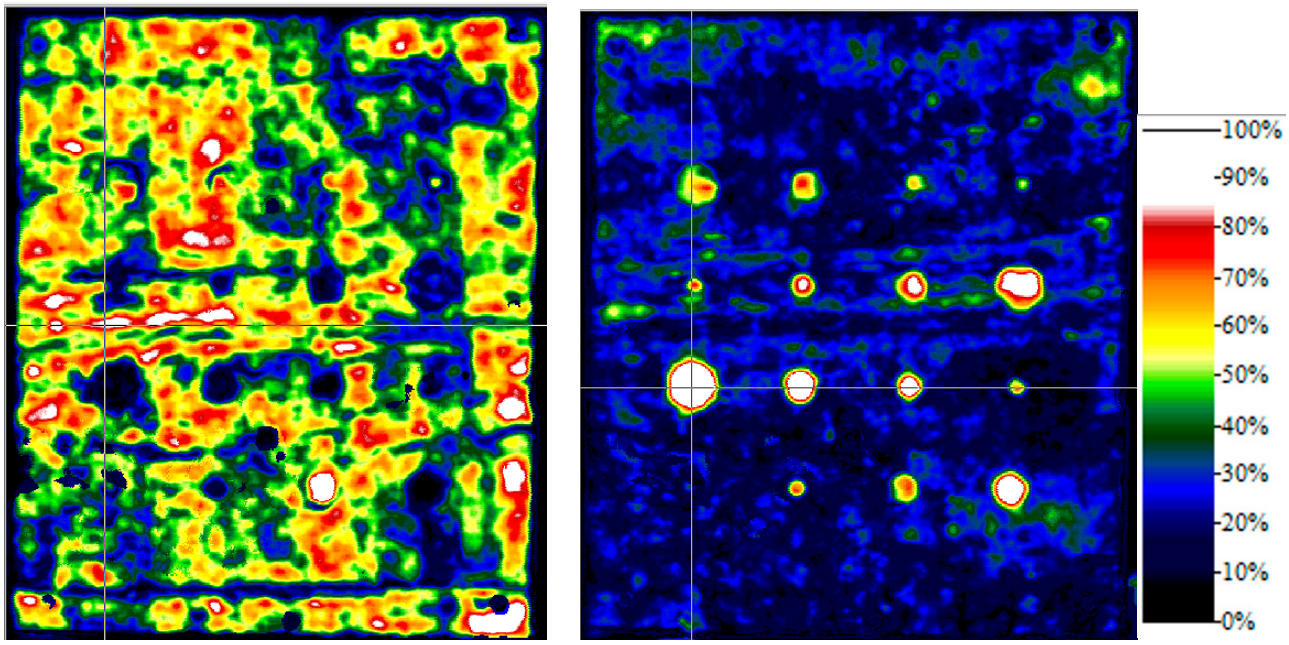

Conventional UT Attenuation C-scans, gate on BR *Conventional UT reflection C-scan, gate between FR and BR*

Figure 8-2: Conventional attenuation and reflection C-scans of IRP1, 500kHz

Beside the amplitude C-scans also the TOF data is collected. Figure 8-3 shows the PAUT TOF C-scan data, generated as four individual scan strokes. All FBH's are detected, the FBH's at a larger depth with a somewhat decreased color contrast compared to the BR (orange/red). The TOF data is collected with a longitudinal sound velocity set on 2700 m/s comparable to the sound velocity used during the conventional UT experiments.

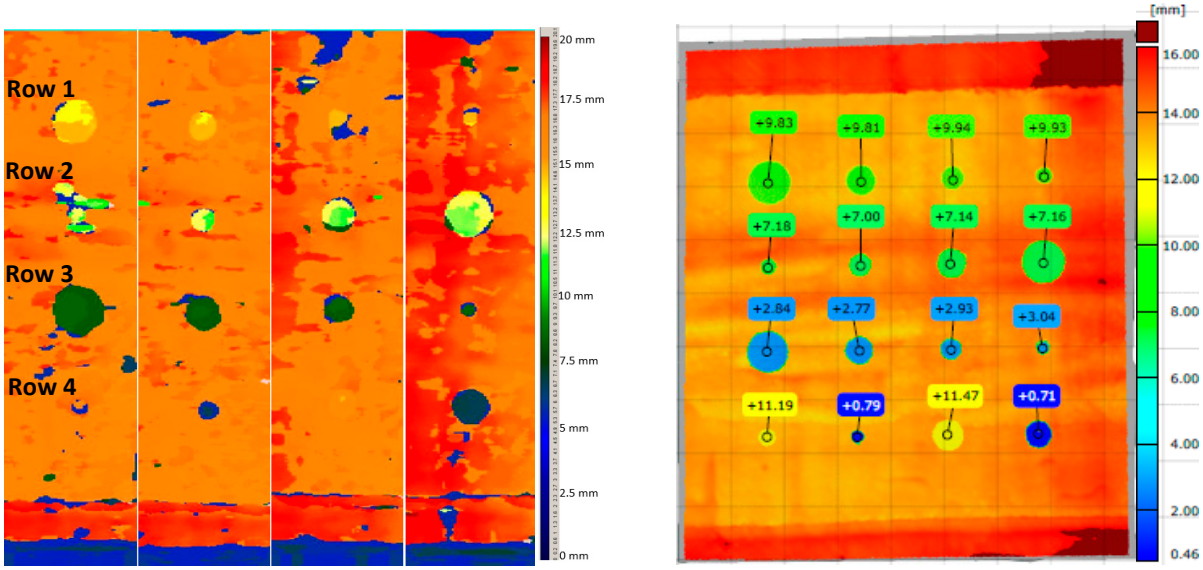

Figure 8-3: PAUT Time Of Flight C-scan of IRP1, 500kHz, gate just after FR and including BR, actual remaining material

During the evaluation of the conventional UT TOF data it was noted that not all FBH's were represented at the correct depth position due to collection of multiple echo's (bulky signal). This also applies for the PAUT TOF data, when taken a closer look at the A-scan signals the following can be observed:
Due to the coarse grained material, the PAUT signals are also quite broad and bulky. Figure 8-4 shows an example of the PAUT A-scan signal derived from IRP1. The parameters of the TOF gate (blue gate) involves the Start, End and the Height. Further, the triggering and Peak determines the way the UT signals are measured. The red circles in Figure 8-4 indicate the difference in sampling the PAUT signal between measuring the first peak or the maximum. The point of measuring is indicated by a blue cross and also depends on the Height setting. E.g. when the height setting was selected to 20 % the first Peak crossing will be somewhere at the yellow arrow(s) which has a large influence on the TOF measurement.

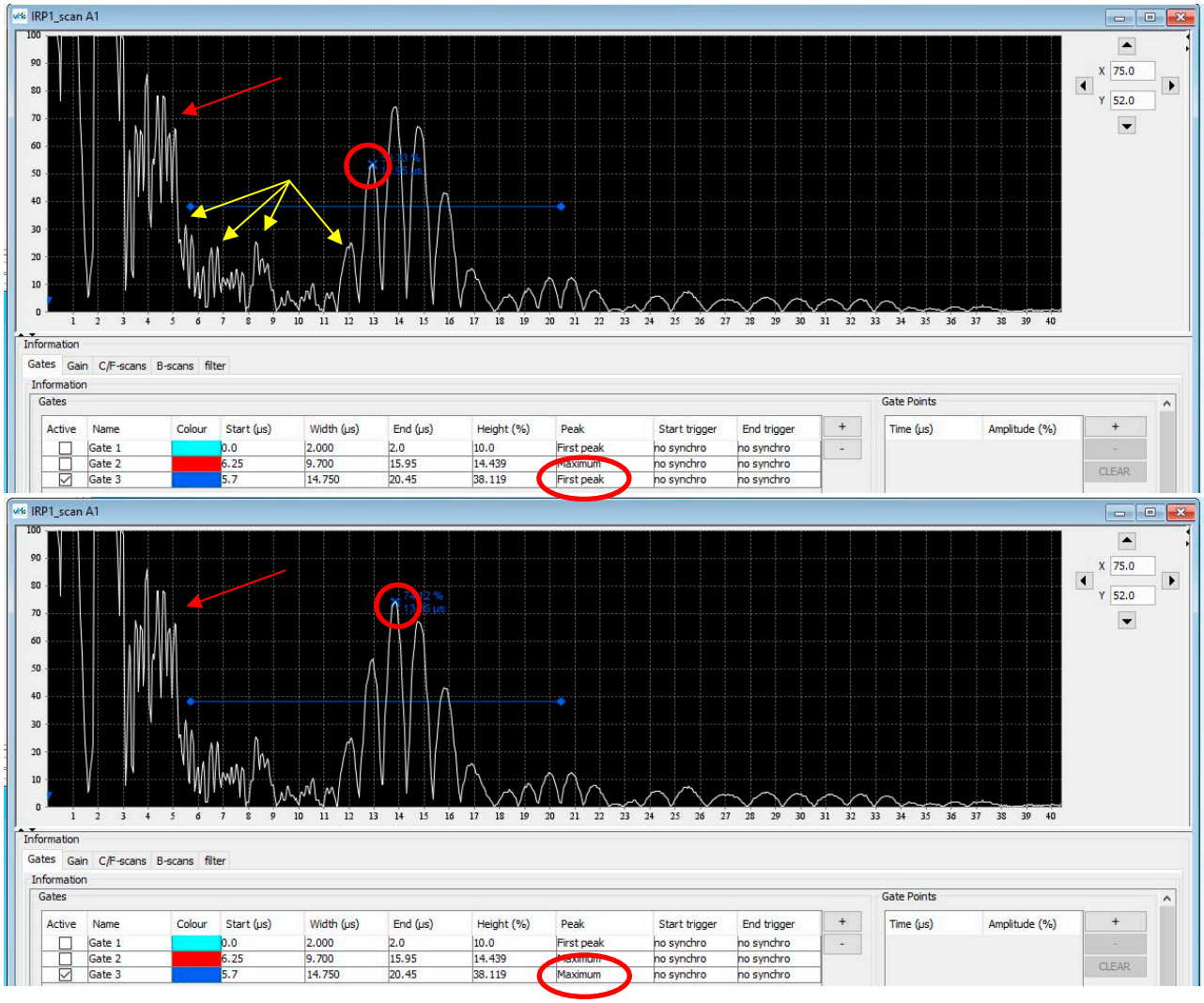

Figure 8-4: Example of PAUT A-scan signals of IRP1

Further, as mentioned in chapter 5, the optimum coupling and sliding conditions exists when the protecting Polyurethane foil has a somewhat convex shape, see also Figure 5-5. Disadvantage of this approach is that the entry signal is not so well defined, see red arrows in Figure 8-4. The broad entry signal reduces an accurate gate start just after the entry signal which has a negative influence to collect reflection signals (amplitude or TOF) of near surface defects.

8.2 IRP4 Relative flat monolithic skin stepwedge

Figure 8-5 shows both the PAUT (three individual scan strokes) and conventional UT attenuation C-scan monitoring the amplitude of the BR. Although some similarity at certain areas can be distinguished, see corresponding color circles, also a quite deviating test results can be observed. More precisely, this deviating test result is likely caused by slightly different gate settings. As already mentioned during the evaluation of the conventional UT it is not possible to define one gate setting to collect all reflections signals in one reflection C-scan.

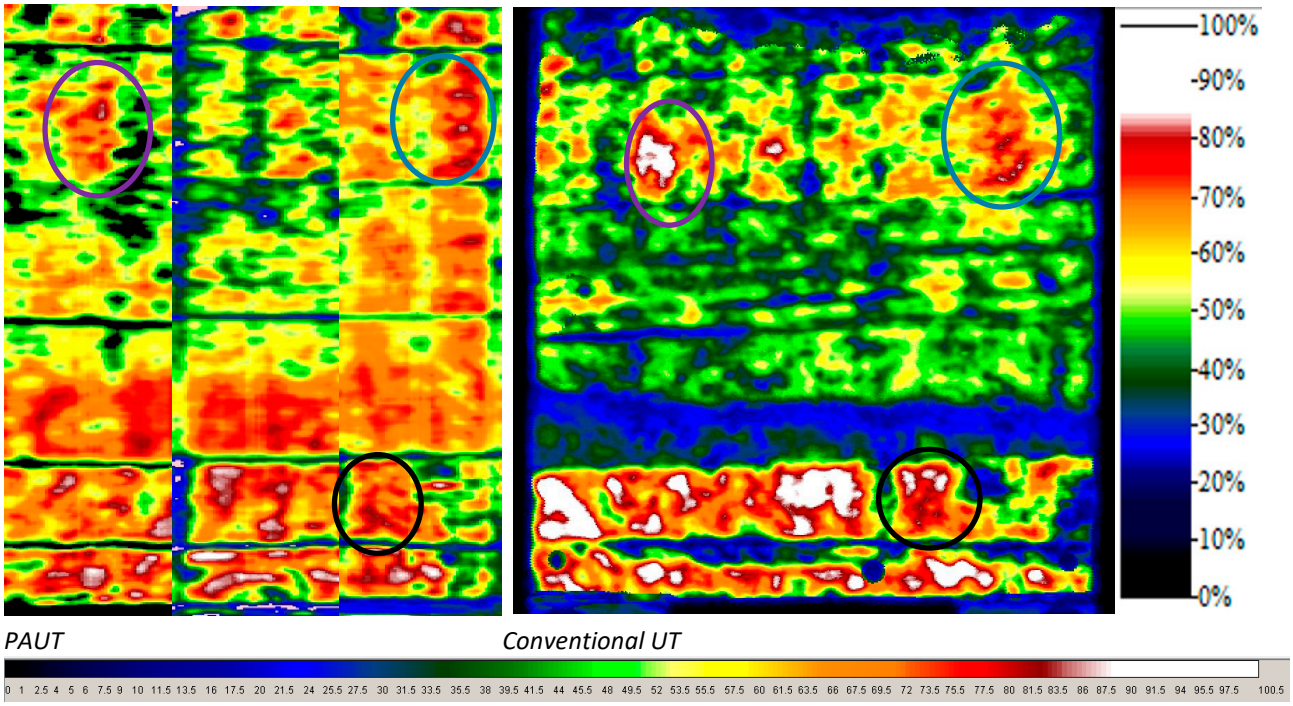

Figure 8-5: IRP4 Attenuation C-scans, with DAC/TCG, 500kHz, gate on BR, the three circles indicate some similarity

Figure 8-6 shows the TOF data of IRP4 (three individual scan strokes) and the 3D data. The different thickness steps are clearly identified. However, when interpret the color scale of the TOF it can be concluded that the quantification of the thickness is not correct. This incorrect test results are caused by multiple echo's and the different choices with gate settings as mentioned by IRP1, see also Figure 8-4.

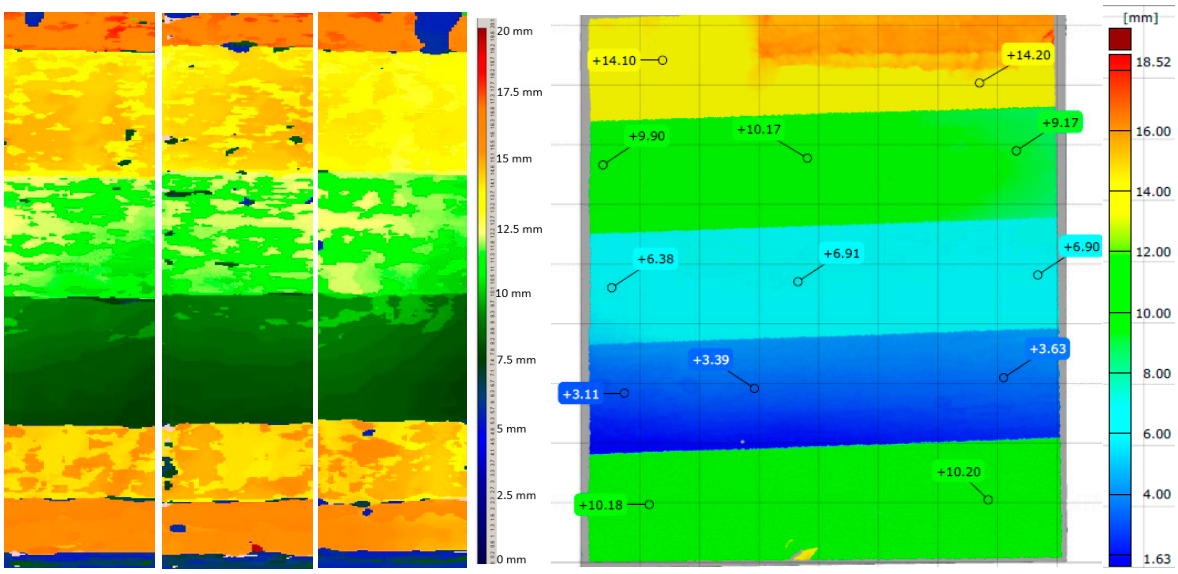

Figure 8-6: PAUT Time Of Flight C-scan of IRP4, 500kHz, gate just after FR and including BR, actual remaining material

8.3 IRP10 Relative flat sandwich skin

Figure 8-7 shows the attenuation of IRP10 for PAUT and conventional UT. As expected the FBH's of IRP10 cannot be detected with the ultrasonic method. The FBH's of row 1 simulate, in fact, a debonding between the GFRP skin material and the core balsa wood. The high porosity content of the balsa wood already gives a 100 % reflection of the ultrasound beam. Therefore, no extra reflection can be expected from the FBH located at the glass/balsa wood interface. As expected, the FBH's at the opposite side of the balsa wood (inner side) cannot be detected because the ultrasound beam cannot penetrate through the balsa wood. Noticeable is the similarity between the PAUT data and the conventional UT data.

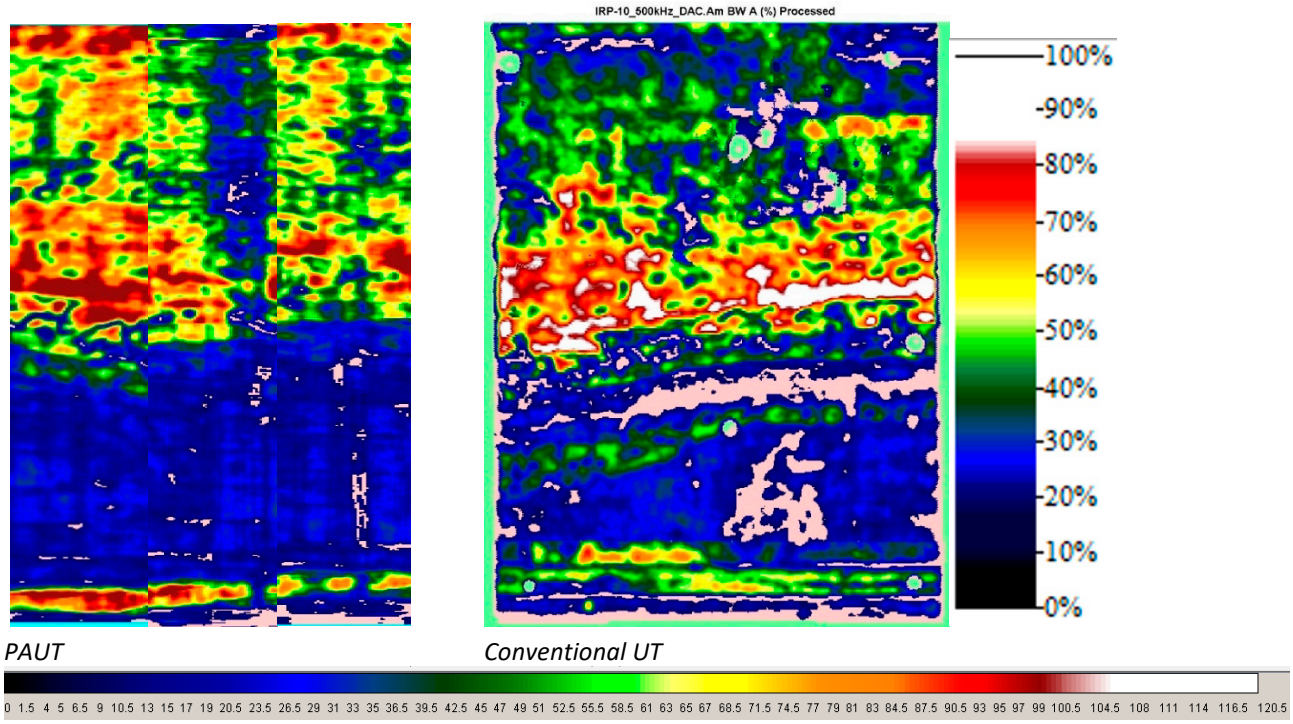

PAUT *Conventional UT*

Figure 8-7: IRP10 Attenuation C-scans, with DAC/TCG, 500kHz, gate on interface glass/balsa wood

The same conditions applies for the reflection C-scan, thus the FBH's are not detectable. Further, also the PAUT and conventional UT reflection data give similar test results.

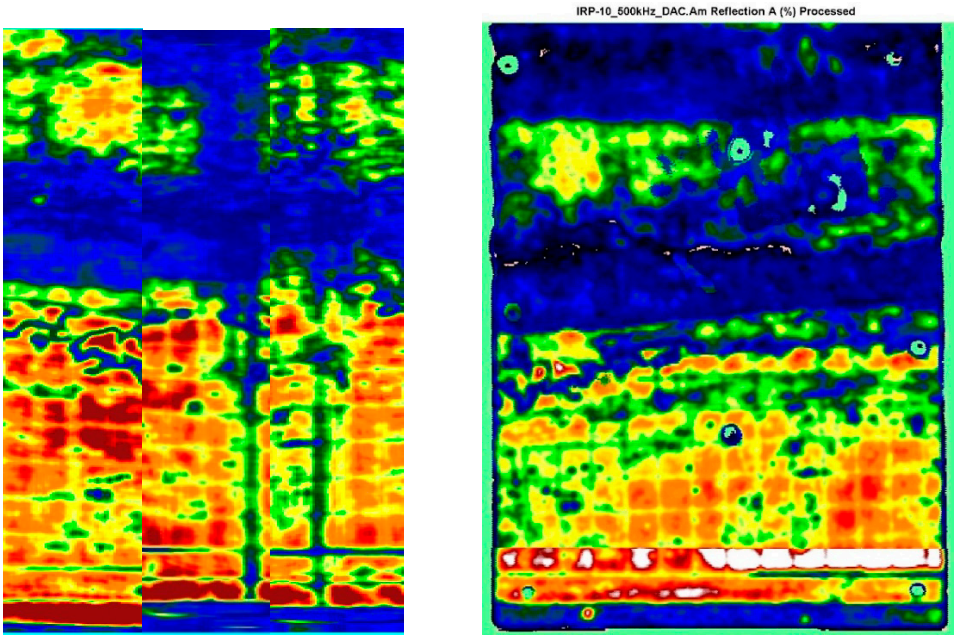

PAUT *Conventional UT*

Figure 8-8: IRP10 reflection C-scans, with DAC/TCG, 500kHz, gate on interface glass/balsa wood

Figure 8-9 shows the TOF data, in fact the thickness of the GFRP outer skin is shown until the acoustic obstacle balsa wood gives a 100% reflection.

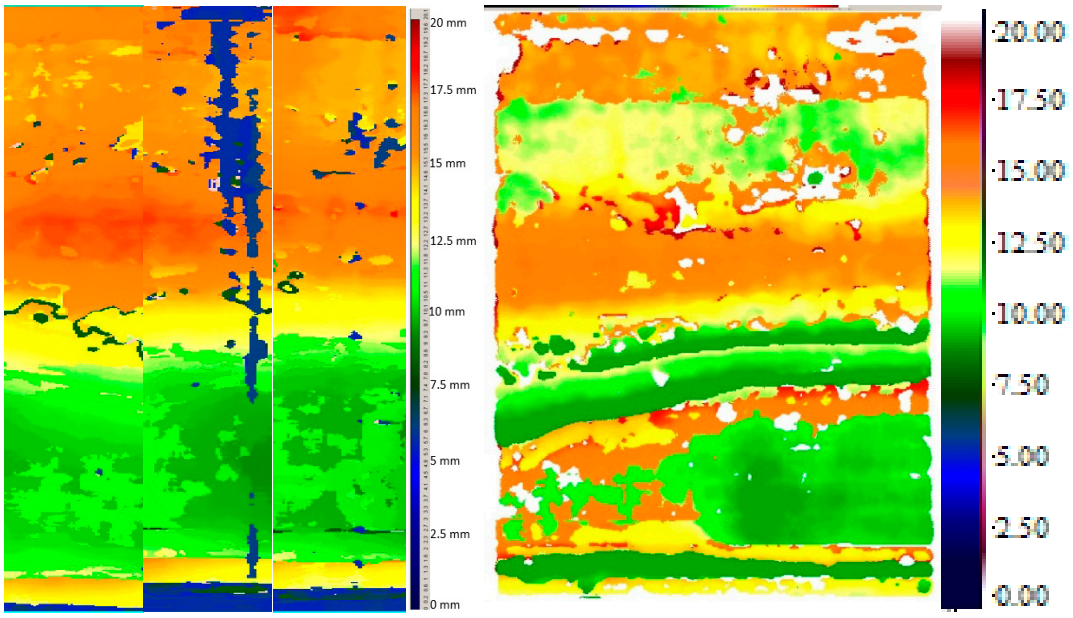

Figure 8-9: PAUT TOF C-scan of IRP10, 500kHz, gate just after FR and including BR, TOF conventional UT

8.4 IRP13 Curved monolithic skin part

Figure 8-10 shows both the attenuation and reflection C-scans of IRP1. When observing the C-scans more in detail the following can be observed:

Note: Figure 8-11 shows the measured depth positions (remaining material) of the FBH's in IRP13.

- At the first row only the contour of the FBH's (diameters of 0.5, 0.75, 1 and 1.5 inch) at a depth of approx. 11.6 mm can be seen in the PAUT attenuation C-scan. In fact, the reflection of the FBH's and the reflection of the backwall cannot be separated on the A-scan trace. In the reflection C-scan all FBH's of row 1 are clearly detected with exception of the 0.5 inch dimeter FBH;
- For the second row, all FBH's at a depth of approx. 7.6.mm are detected for both the PAUT attenuation and reflection C-scan. Because the depth of the FBH's and the backwall are more separated the signals can be clearly separated on the A-scan trace. Exception is the 0.5 inch FBH at the reflection C-scan, due to a local quality reduction reflection signals of the basis material more or less mask the FBH and therefore limited detectable;
- The FBH's of the third row are positioned at a depth of approx. 3.7 mm. All FBH's in both the PAUT attenuation and PAUT reflection C-scan are detectable;
- At row 4 both near surface FBH's (0.5 and 1 inch) are detectable in the PAUT attenuation C-scan. In contrast to the far surface FBH's, again the reflection of these FBH's and the reflection of the backwall cannot be separated on the A-scan trace. At the PAUT reflection C-scan, the 1 inch diameter near surface FBH's at depths of 2.5 is detected and at the position of the 0.5 inch near surface only a quit small reflection can be observed, but regarded as not detectable. The 0.5 inch diameter far surface FBH at a depth of 13 mm is detected, the 1 inch far surface FBH can be detected but with a relative small amplitude and considered not detectable.

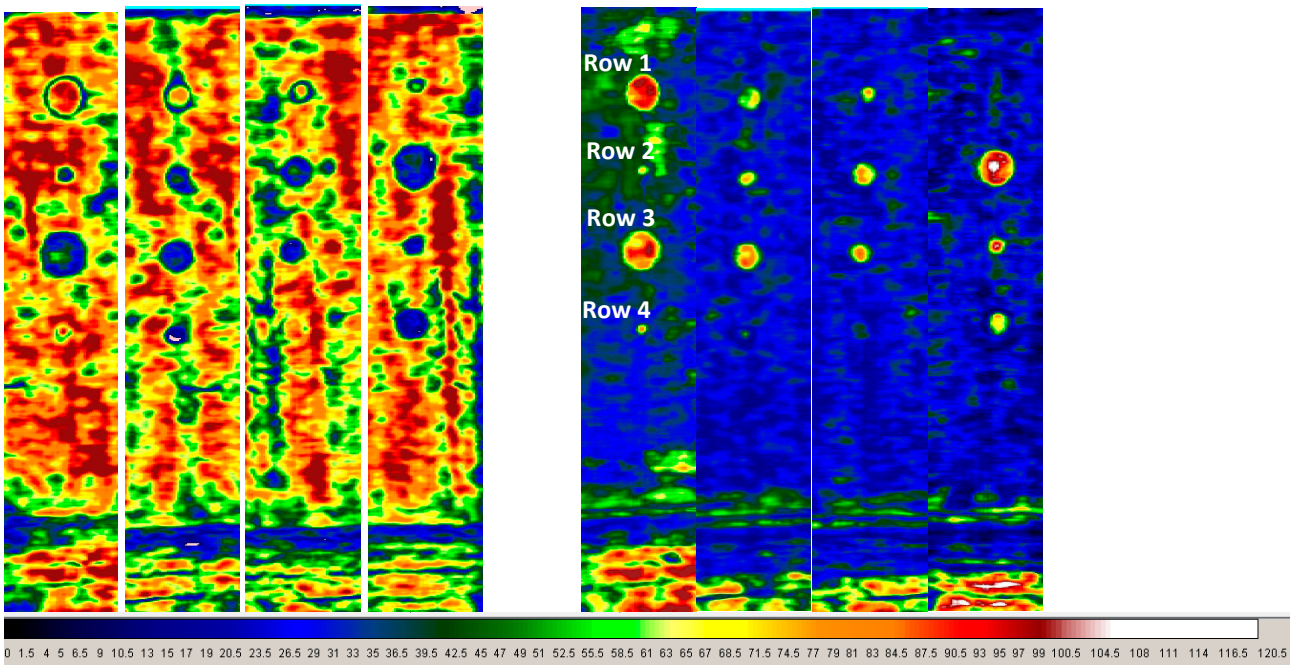

PAUT Attenuation C-scans, gate on BR *PAUT reflection C-scan, gate between FR and BR*

Figure 8-10: PAUT attenuation and reflection C-scans of IRP13, 500kHz

Beside the amplitude C-scans also the TOF data is collected. Figure 8-11 shows the PAUT TOF C-scan data, again as four individual scan strokes. All FBH's are detected, the FBH's at a larger depth with a somewhat decreased color

contrast compared to the BR (orange/red). The TOF data is collected with a longitudinal sound velocity set on 2700 m/s comparable to the sound velocity used during the conventional UT experiments. During the evaluation of IRP1 it was noted that not all FBH's were represented at the correct depth position due to collection of multiple echo's (bulky signal) or gate triggering parameters. This also applies for the TOF data of IRP13.

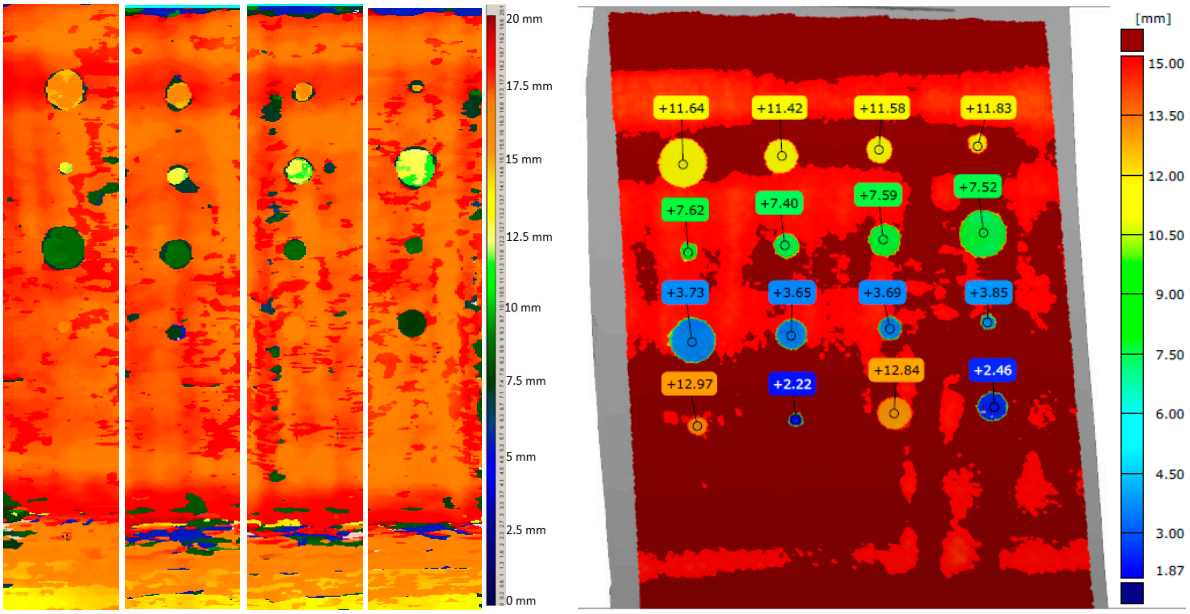

Figure 8-11: TOF C-scan and 3D measurements test results of IRP13

8.5 IRP27 Skin/spar bonded connection

In total 3 diameter FBH's are inserted in IRP27, 0.5 inch (12.7mm), 0.75 inch (19.1 mm) and 1 inch (25.4 mm) respectively on two depth positions as indicated in Figure 8-12. The two depth position simulate a disbonding between the GFRP skin and the adhesive layer and a disbond between the adhesive layer and the GFRP spar. Due to the relative thick adhesive layer both interfaces are chosen as possible critical interfaces.

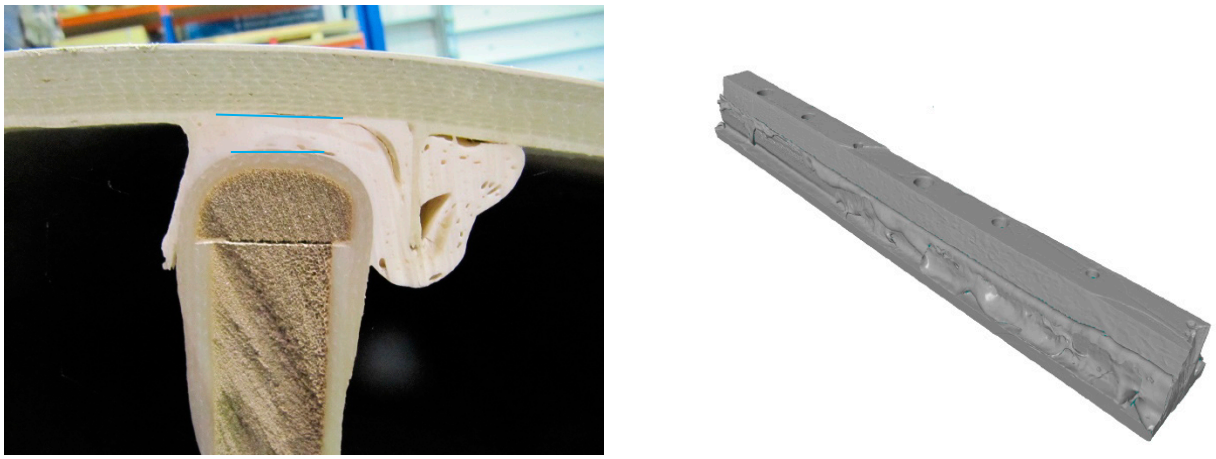

Figure 8-12: Detailed view of IRP27 showing the skin/spar bonding connection and the depth positions of the FBH's

As in the case with conventional UT, only the backwall echo is relevant to monitor, due to the fact that the defects are located at the interface of the skin and the adhesive layer. More-or-less the same test results are achieved as during conventional UT. The higher reflection of the backwall echo (white/red circle) is caused due to the fact that the ultrasound cannot be transmitted into the adhesive layer and back-up structure (locally removed by machining), see Figure 8-13. In this case the FBH's are detected due to the fact that the circle shape is known. When observing the complete C-scan, including all amplitude differences it must be concluded that the debonding can be detected doubtfully. Larger defect sizes are most probably detectable but not included in this reference panel to underpin this statement with experimental results. The FBH's located at the interface adhesive/stiffener are not detected.

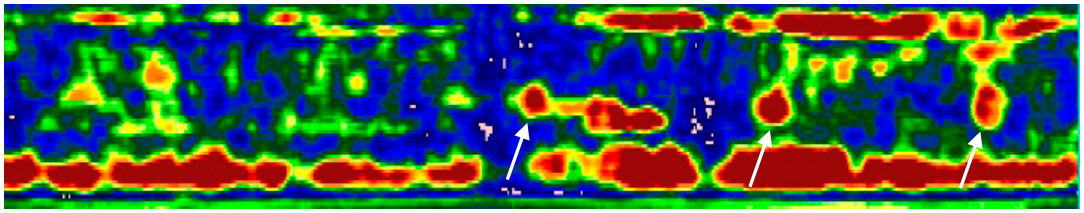

Figure 8-13: PAUT reflection and TOF C-scan of IRP27, 500kHz

9 Conclusions

1. Based on the literature “Survey on Remote Inspection of Offshore Wind Turbine Blades” (ref.1), the ultrasonic-based NDI methods is found to be the most practical approach in terms of miniaturization possibilities and damage detection.

PAUT sliding probe development

2. Commercial low frequency Phased Array wheel probes, in principal suitable for the rotor blade inspection task, have a weight of >5 kg (excluding cable and connector). Payload is key, because the crawler and sensor package are transported by drone. NLR developed a PAUT sliding probe with a payload < 1 kg.
3. The 3D printed PAUT sliding probe casing and protection foil, which is in direct contact with the rotor blade, showed good acoustic coupling. Only a small spray of water must be applied to the inspection surface, comparable to commercial PAUT wheel probes.
4. A sensitivity test was performed, during several tests an equal ultrasound output over the entire width of the array probe was observed.
5. Adjustment of the amount of water between the PA-transducer and the protection foil is critical. In this proof-of-concept, this amount of water was not a very controlled parameter.

PAUT sliding probe integration:

6. Assembly brackets are designed and 3D printed to enable the integration of the NLR PAUT sliding probe into the sensor package of the TU-Delft. Final integration and testing is not performed.

Rotor blade reference specimens:

7. It is expected that the material quality of the investigated rotor blades is rather low compared to nowadays manufacturing quality. Besides, ultra-fine and large porosities in the matrix fibre-rich areas can be seen at cross-sections and CT-scan analyses. Cracks are also observed in the fibre-rich areas. This relatively low material quality is an extra complicated factor for the ultrasonic inspections. In other words, the achieved NDI results can be interpreted as conservative, better material quality of the rotor blades will probably lead to improved inspection results.
8. The overall size of the investigated rotor blades is rather small compared to nowadays off-shore windmills. Besides larger surface areas also the thickness of these off-shore rotor blades is increased up to approximately 60 mm. Compared to the investigated thickness of 15 mm, this is a significant deviation.

Baseline ultrasonic C-scan inspection:

9. Automated ultrasonic C-scan at immersed conditions using focused transducers is characterised as the optimum ultrasonic inspection and used as a baseline.
10. Optimum transducer frequency is determined experimentally at 500 kHz.
11. Time Corrected Gain (TCG) approach is necessary due to the coarse grained high attenuative GFRP material.

Monolithic configurations flat and curved:

12. Due to the coarse grained high attenuative GFRP material the attenuation C-scans monitoring the backwall are less suitable.
13. All diameter FBH’s (0.5, 0.75, 1 and 1.5 inch) are detected monitoring amplitude of the FBH reflection signals.
14. When measuring the duration of the signals the FBH’s at larger depth (~7 and ~ 10 mm) are presented correctly in the data. But the FBH’s located closer to the transducer (< 3 mm) are presented in the data at a larger depth. These FBH’s are detected by monitoring multiple echo’s (bulky signal) from the FBH.

15. Due to the 3D scanning option of the NLR C-scan system no detectability changes are observed between relative flat and curved panels.

Sandwich configuration:

16. Only the GFRP layer positioned at the outer side of the rotor blade can be inspected. In fact, this part of the cross-section can considered as a monolithic skin.
17. Disbonds between GFRP skin and Balsa wood cannot be detected.
18. Due to high porosity content of the balsa wood, it is not possible to inspect the GFRP skin positioned at the inner side of the rotor blade.
19. Overall, it is not possible to inspect the complete cross-section of a sandwich configuration.

Skin/spar bonded connection:

20. The amplitude differences caused by sound material masked the inserted FBH's. Larger defect sizes are most probably detectable but not included in this reference panel. Hence, no experimental data is available to underpin this statement.

CIVA modelling PAUT:

21. The CIVA modulation definitely supports the experimental investigation. The appearance of the ultrasound beam profiles per aperture size gives an underpinned insight to make the correct choice.
22. The FBH responses in CIVA and the experimental test results are quite comparable.
23. For now, GFRP material was selected from the CIVA library. This implicates that the quality of the material w.r.t voids, undulations, small cracks is not taken into account. This makes the simulation less representative.

Experimental PAUT in combination with manual PAUT sliding probe:

24. For the PAUT inspection also the relative low frequency of 500 kHz was used in combination with TCG application, which is in line with the baseline ultrasonic C-scan inspection:
25. During the manual inspections of the five reference specimens a constant acoustic coupling was observed.
26. To obtain the optimum coupling and sliding conditions, the Polyurethane foil has to have a somewhat convex shape, actually creating a very small water column. Disadvantage of this approach is that the entry signal is not so well defined. This reduces the detection of defects just below the transducer (near surface resolution).

Monolithic configurations flat and curved:

27. All diameter FBH's (0.5, 0.75, 1 and 1.5 inch) are detected monitoring amplitude of the FBH reflection signals. In general, it can be concluded that the ultrasonic test results are quite similar compared to the baseline automated ultrasonic C-scan inspections.
28. Comparable with the baseline ultrasonic C-scan inspection, the FBH's relative close located to the transducer are detected based on multiple echo's (bulky signal). In the time-of-flight C-scans these FBH's are presented incorrectly.
29. The PA-probe has a rigid facing. When a single curved panel is inspected and the long side of the probe is 90 degrees w.r.t. the curvature the inspections can be performed and no reduction of detectability is observed. In other directions no inspection can be performed. Keeping the probe perpendicular to the inspection surface is detrimental but doable. The same accounts for a roller probe, also here small misalignment will lead to a reduction of defect detectability.

Sandwich configuration:

30. Overall, it is not possible to inspect the complete cross-section of a sandwich configuration. Only the GFRP layer positioned at the outer side of the rotor blade can be inspected. In fact, the same conclusion can be drawn as by the baseline inspections

Skin/spar bonded connection:

31. The same conclusion can be drawn as with baseline inspections, amplitude differences caused by sound material masked the inserted FBH's. Larger defect sizes are most probably detectable but not included in this reference panel. Hence, no experimental data is available to underpin this statement.

10 Recommendations

1. The reference specimens were cut from relative old (~30 years) rotor blades with relative low material quality. In consequence, this relatively low material quality has an negative influence on the inspection performance. Due to improved manufacturing technology nowadays, rotor blades probably contain less manufacturing defects (e.g. delaminations, voids etc.) which will have a positive effect on the inspection performance. It is recommended to perform the inspections on more representative material quality.
2. On the other hand, large off-shore rotor blades have skin thickness of approx. 60 mm. Compared to the reference specimens used in this investigation (15 mm), it is questionable whether the reference specimen used in this study represents the current state. It is essential that the experiments are performed on representative thicknesses.
3. CIVA simulations were performed using the material library from the CIVA software. To increase the reliability of the simulations, it is recommended to improve the material input parameters and take into account the anisotropic material and relevant elasticity coefficients.
4. This investigation is performed with an aperture of 16 elements to generate the ultrasonic sound beam. Using a phased array ultrasonic device which is capable in selecting 32 or even 64 elements an increase of “penetration power” will be achieved. This is beneficial to inspect coarse grained high attenuative GFRP material.
5. The developed PAUT sliding probe functioned quite well under handheld conditions. More tests in combination with the crawler are needed.
6. The amount of fluid between the PA-transducer and the protecting foil is quite critical to get the optimum coupling and sliding performance. A redesign of the PAUT sliding probe is needed having an feature that enables the control of the amount of fluid.
7. Payload is key. Besides the development of the light weight sensor package, a survey is needed to determine the optimum light weight ultrasonic device.
8. Development of a wireless remote communication device is needed, two aspects: i) operation of the ultrasonic device ii) data collection and validation.

11 References

1. Hwang J.S., Platenkamp D.J., Beukema R.P. “A literature Survey on Remote Inspection of Offshore Wind Turbine Blades”, NLR-CR-2020-223.

Appendix A Basic UT conventional parameters

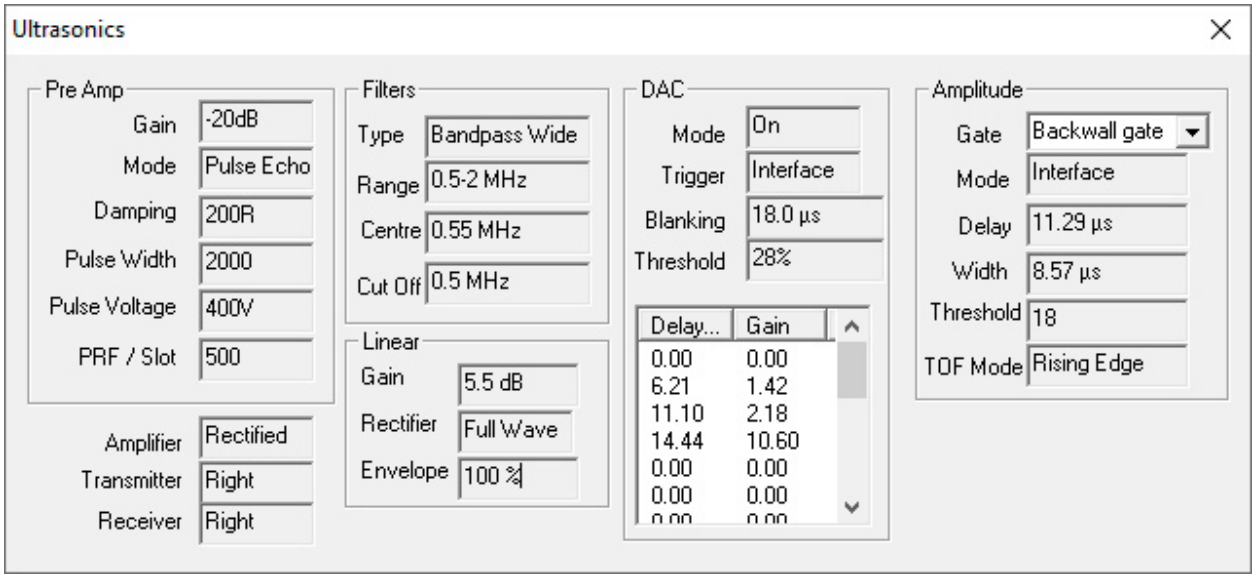

Appendix B Basic PAUT parameters

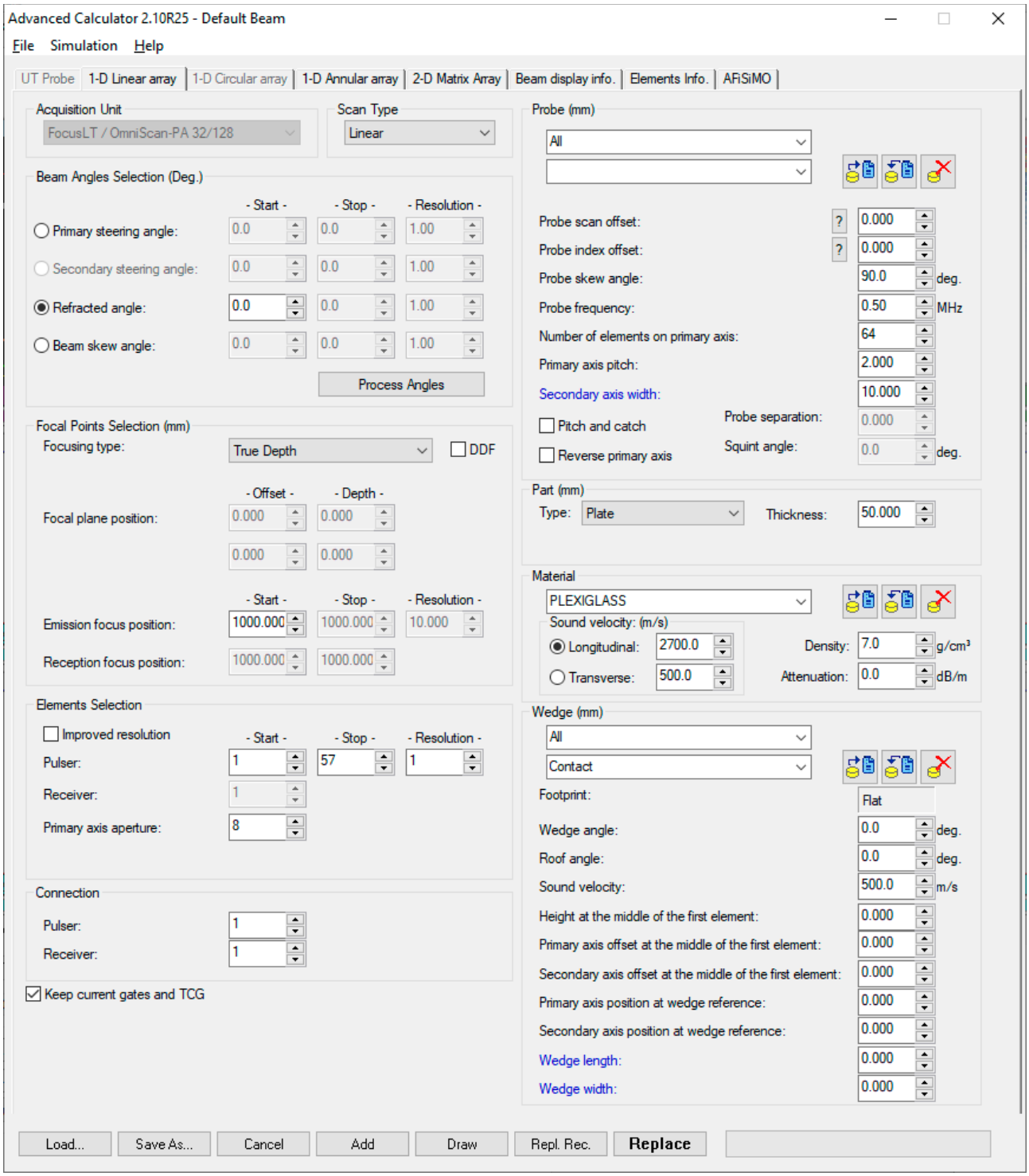

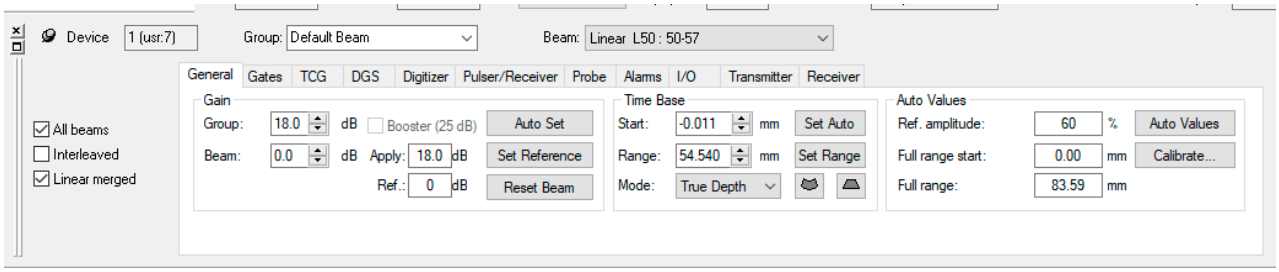
Device
1 (usr:7)
Group: Default Beam
Beam: Linear L50 : 50-57
General
Gates
TCG
DGS
Digitizer
Pulser/Receiver
Probe
Alarms
I/O
Transmitter
Receiver
All beams
Interleaved
Linear merged
Gain
Group:
18.0
dB
Booster (25 dB)
Auto Set
Beam:
0.0
dB
Apply:
18.0
dB
Set Reference
Ref.:
0
dB
Reset Beam
Time Base
Start:
-0.011
mm
Set Auto
Range:
54.540
mm
Set Range
Mode:
True Depth
Auto Values
Ref. amplitude:
60
%
Auto Values
Full range start:
0.00
mm
Calibrate...
Full range:
83.59
mm

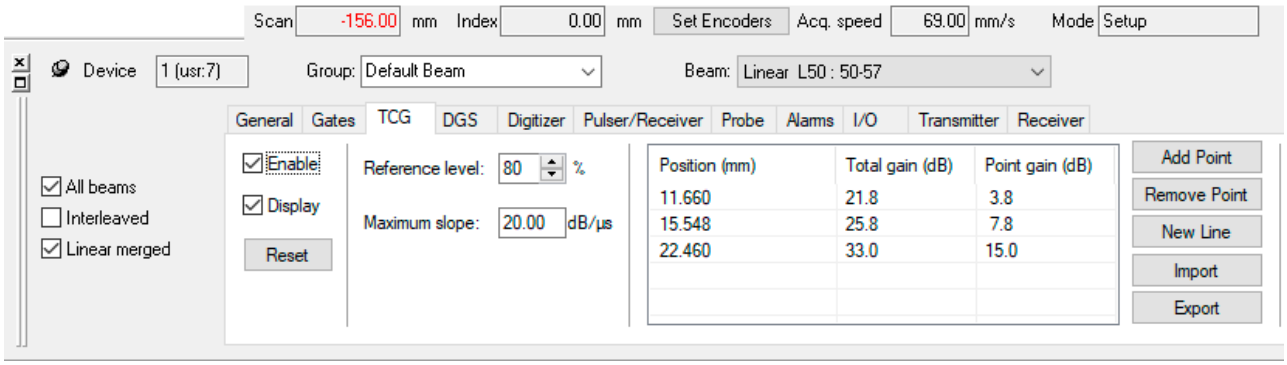
Scan
-156.00
mm
Index
0.00
mm
Set Encoders
Acq. speed
69.00
mm/s
Mode
Setup
Device
1 (usr:7)
Group: Default Beam
Beam: Linear L50 : 50-57
General
Gates
TCG
DGS
Digitizer
Pulser/Receiver
Probe
Alarms
I/O
Transmitter
Receiver
All beams
Interleaved
Linear merged
Enable
Display
Reset
Reference level:
80
%
Maximum slope:
20.00
dB/µs
Position (mm)
Total gain (dB)
Point gain (dB)
11.660
21.8
3.8
15.548
25.8
7.8
22.460
33.0
15.0
Add Point
Remove Point
New Line
Import
Export

Dedicated to innovation in aerospace

Royal NLR - Netherlands Aerospace Centre

NLR operates as an objective and independent research centre, working with its partners towards a better world tomorrow. As part of that, NLR offers innovative solutions and technical expertise, creating a strong competitive position for the commercial sector.

NLR has been a centre of expertise for over a century now, with a deep-seated desire to keep innovating. It is an organisation that works to achieve sustainable, safe, efficient and effective aerospace operations.
The combination of in-depth insights into customers' needs, multidisciplinary expertise and state-of-the-art research facilities makes rapid innovation possible. Both domestically and abroad, NLR plays a pivotal role between science, the commercial sector and governmental authorities, bridging the gap between fundamental research and practical applications. Additionally, NLR is one of the large technological institutes (GTIs) that have been collaborating over a decade in the Netherlands on applied research united in the TO2 federation.

From its main offices in Amsterdam and Marknesse plus two satellite offices, NLR helps to create a safe and sustainable society. It works with partners on numerous programmes in both civil aviation and defence, including work on complex composite structures for commercial aircraft and on goal-oriented use of the F-35 fighter. Additionally, NLR helps to achieve both Dutch and European goals and climate objectives in line with the Luchtvaartnota (Aviation Policy Document), the European Green Deal and Flightpath 2050, and by participating in programs such as Clean Sky and SESAR.

For more information visit: **www.nlr.org**

Postal address
PO Box 90502
1006 BM Amsterdam, The Netherlands
e) info@nlr.nl **i)** www.nlr.org

Royal NLR
Anthony Fokkerweg 2
1059 CM Amsterdam, The Netherlands
p) +31 88 511 3113

Voorsterweg 31
8316 PR Marknesse, The Netherlands
p) +31 88 511 4444